Deformation measurement and monitoring with Ground-Based SAR

Oriol Monserrat Hernández

Advisor:
Dr. Michele Crosetto
Unitat de Teledetecció Activa
Institut de Geomàtica
Castelldefels, Spain

Tutor:
Prof. Josep Gili Ripoll
Dep. d'Enginyeria del Terreny
Universitat Politècnica de Catalunya
Barcelona, Spain

Acknowledgements

This dissertation encompasses some of the most important results of the research activities that I have carried out at the Active Remote Sensing Unit (TA) of the Institute of Geomatics, during approximately the last six years. I started my activities at TA in October 2003, developing algorithms and data analysis tools for deformation measurement using satellite-based Synthetic Aperture Radar (SAR) interferometry. Most of the experience gained with satellite-based SAR turned to be essential for my Ground-Based SAR (GB-SAR) research, which is the subject of this thesis. This research started approximately six years ago, when we began the GALAHAD project (www.galahad.eu), which introduced us to two relatively new techniques: GB-SAR and Terrestrial Laser Scanning. I was fully involved in this project, which was useful to assess the potentialities of the GB-SAR technique for measuring deformations. In 2008 the Institute of Geomatics bought the IBIS instrument, the first GB-SAR system commercially available worldwide, which was developed by Ingegneria dei Sistemi SpA (IDS), one of the industrial partners of the GALAHAD project. In the last three years, a great part of my work has been devoted to GB-SAR deformation monitoring, by developing new algorithms and data analysis tools, making campaigns and exploring new applications.

This work would have not been possible without the support and effort of my advisor, Dr. Michele Crosetto. I would like to express my gratitude to him for his useful advices, his patience, the comments and long enjoying discussions and, why not, for his kind temporal pressure and the confidence he put on me. I would also thank my girlfriend and colleague Marta for her unconditional support, especially during these last months, for her advices, for being there always and for participating to all my cooking experiments. Special thanks to my mother, my father and my sister for their invaluable support.

I would like to thank my colleagues of the Institute of Geomatics, and specially those of TA, which have been playing an important role in my work. I would specially thank my roommate and colleague, Dr. Guido Luzi, for the enriching discussions, in the office and in the GB-SAR van, not only about GB-SAR but also about politics, philosophy or football. Thanks also to Maria for her comments on this work and her GB-SAR campaign omelettes, and to Núria for her last check of the work and her high-level jokes.

I can not forget to thank Prof. Bruno Crippa for his help, for our Skype talks, for his criticism with my particular way of programming, and for teaching me key sentences of Lombard dialect. Finally, a special mention is deserved to Prof. Josep Gili, my thesis tutor, for his kind help during all these years, his participation to the Vallcebre campaigns, and for his special barbecues.

To conclude, I would like to acknowledge the Galahad project for providing the Formigal landslide dataset, the UPC and the Safeland project for supporting part of the Vallcebre campaigns, the CTP project Saxum for funding the Canillo campaigns, and the project of the Fundación Ciudad de la Energía (www.ciuden.es) for financing part of the experiments realized in this work. Finally I acknowledge IDS for the open-pit dataset.

Abstract

The Ground-Based Synthetic Aperture Radar (GB-SAR) is a relatively new technique, which in the last ten years has gained interest as deformation measurement and monitoring tool. The GB-SAR technique is based on an imaging radar-based sensor, which offers high sensitivity to small displacements, in the region of sub-millimetres to millimetres, long-range measurements, which can work up to some kilometres, and massive deformation measurement capability. These features confer to the GB-SAR technique interesting advantages with respect to other point-wise deformation measurement techniques.

The process of estimating deformation from the GB-SAR data is not straightforward: it requires complex data processing and analysis tools. This dissertation is focused on these tools, covering the whole deformation estimation process. This thesis collects the main research results achieved on this topic during my work at the Active Remote Sensing Unit of the Institute of Geomatics. Two different approaches for measuring deformation with GB-SAR data are described and discussed. The first one is the interferometric approach, based on the exploitation of the phase component of the GB-SAR data, which is the commonly used GB-SAR method. The second one is a non-interferometric approach, which exploits the amplitude component of the GB-SAR data, offering an interesting alternative way to exploit the GB-SAR data.

This dissertation has two main objectives. The first one is presenting, step by step, a complete interferometric GB-SAR procedure for deformation measuring and monitoring. The second one is presenting two new algorithms, which represent the most innovative part of this thesis. The first algorithm faces the phase unwrapping problem, providing an automatic solution for detecting and correcting unwrapping errors, which is called 2+1D phase unwrapping. The second algorithm is the base of the above mentioned non-interferometric approach, which overcomes some of the most critical limitation of GB-SAR interferometry, at the expense of getting less precise deformation estimates.

The dissertation is divided in 6 chapters. The first one is the introduction, while the second one provides an overview of GB-SAR interferometry, introducing the main aspects that are the basics of the subsequent chapters. Chapter 3 describes a complete GB-SAR processing chain. Chapters 4 and 5 contain the most original part of the dissertation, i.e. the 2D+1 phase unwrapping algorithm, and the non-interferometric approach. Finally, in Chapter 6 the conclusions are discussed and further research is proposed.

Key words: GB-SAR, deformation measurement, interferometry, phase unwrapping, non-interferometric approach.

Resum

El radar terrestre d'obertura sintètica (GB-SAR) és una tècnica relativament nova que, en els últims deu anys, ha guanyat interès com a eina per a mesurar i monitorar deformacions. La tècnica GB-SAR es basa en un sistema radar amb capacitat per proporcionar imatges, que ofereix una alta sensibilitat a petits desplaçaments, d'ordre mil · limètric o submil · limètric, que és capaç de mesurar a llargues distàncies (alguns km) i que té una alta capacitat per fer mesures massives. Aquestes característiques donen a la tècnica interessants avantatges respecte a altres tècniques clàssiques de mesura de deformacions, típicament basades en mesures puntuals.

Derivar mesures de deformació a partir de dades GB-SAR no és un procés senzill, ja que requereix uns procediments complexos de processat i anàlisi de dades. Aquesta tesi es centra en aquests processos. Aquesta tesi recull alguns dels resultats més destacats de la investigació que he desenvolupat sobre aquest tema a la unitat de Teledetecció Activa de l'Institut de Geomàtica. Al llarg del document es descriuen dues aproximacions diferents per mesurar deformacions amb GB-SAR. Una es basa en la explotació de la tècnica de la interferometria, és a dir explotant la component de la fase de les imatges GB-SAR: és la tècnica GB-SAR usada habitualment. La segona, anomenada tècnica no-interferomètrica, es basa en la component de l'amplitud de les dades GB-SAR i ofereix una interessant alternativa a la primera.

La tesi acompleix dos objectius principals. En primer lloc presenta un procediment complet per la mesura i monitoratge de deformacions mitjançant interferometria GB-SAR. En segon lloc, descriu dos nous algorismes que resolen problemes específics de la interferometria clàssica aplicada al GB-SAR i que representen la part més innovadora d'aquesta tesi. El primer algorisme aborda un dels problemes oberts de la interferometria, el *phase unwrapping*, proposant un mètode automàtic per detectar-ne i corregir-ne els errors. El segon algorisme proposa un nou mètode per a l'explotació de les dades GB-SAR per mesurar deformacions sense utilitzar la interferometria.

La estructura de la tesi consisteix en sis capítols. Després de la introducció, el Capítol 2 proporciona una visió general de la interferometria GB-SAR, introduint els conceptes principals utilitzats en la tesi. En el tercer capítol es descriu una cadena de processament basada en GB-SAR interferomètric. Els capítols quart i cinquè contenen la part més original de la tesi: l'algorisme de *phase unwrapping* i el mètode no-interferomètric per la mesura de deformacions. Finalment, es discuteixen les conclusions principals i es proposen futures línies d'investigació.

Paraules claus: GB-SAR, mesura de deformacions, interferometria, *phase unwrapping*, mètode no-interferomètric.

Content

List of figures

List of tables

Chapter 1

Introduction

The Ground-Based Synthetic Aperture Radar (GB-SAR) is a relatively new technique developed for deformation measuring and monitoring. This technique offers a combination of interesting features. It has high sensitivity to small deformations, in the region of sub-millimetres to millimetres, which is achieved by exploiting the interferometric capability of centimetre-wavelength microwaves. It is a long-range measurement device, which can work up to some kilometres. It can provide, in an automatic way, massive deformation measurements. This is directly related to its imaging capability and represents an interesting advantage compared to many point-wise deformation measurement techniques. Finally, the GB-SAR is mounted on a terrestrial platform: this offers the maximum flexibility in terms of data acquisition over a specific area of interest, at the required time, during the necessary observation period and with the needed temporal sampling. In particular, the GB-SAR technique can be used to monitor a wide range of deformation phenomena, ranging from a few millimetres per year up to metres per day. This flexibility represents a fundamental advantage with respect to any satellite-based deformation monitoring technique, and, in general, makes the GB-SAR system complementary to a number of existing deformation measurement techniques.

This dissertation contains the results of my research on GB-SAR performed at the Active Remote Sensing Unit (TA) of the Institute of Geomatics. The main research activities of TA are focused on the processing, analysis and exploitation of the data acquired by active remote sensing sensors, like satellite-based SAR sensors, GB-SAR and laser scanners, for different applications such as digital surface model generation and deformation measurement, e.g. see Crosetto et al. (2010) and Monserrat and Crosetto (2008). This involves the development of algorithms and procedures for data processing and analysis (Biescas et al., 2007; Crosetto et al., 2011; Monserrat et al., 2011), the development of new applications and validation and quality assessment activities, e.g. see Crosetto et al. (2008) and Adam et al. (2009).

Part of my activity on GB-SAR has been performed in the frame of different projects where TA was involved. Three of them deserve a specific mention, because within them, most of the data used in this thesis were collected: Galahad, Ciuden and Safeland. The Galahad project (www.galahad.eu) was useful to study in depth the limitations and advantages of GB-SAR and terrestrial laser scanners for deformation monitoring, and to develop new tools for data analysis and integration. The landslide of Formigal (Spanish Pyrenees) was one of the test sites of this project and is used in this thesis for evaluating different GB-SAR processing algorithms. In the Ciuden project, which concerns CO_2 storage activities, the GB-SAR is meant to monitor very subtle surface deformation associated with complex deformation phenomena. Two of the main test sites of the thesis,

Algeciras and Castelldefels, were used in Ciuden for assessing the quality of the GB-SAR measurements. Finally, in the Safeland project the GB-SAR is mainly used for the long-term monitoring of landslides. The landslide of Vallcebre (Catalan Pyrenees) was used to test new measurement methodologies and processing algorithms described in this work.

This dissertation has been written with two main objectives. The first one is to provide a complete view of a GB-SAR data processing chain, going from the data acquisition to the generation of the deformation maps. This involves a step by step description of a complete processing and analysis procedure, which includes the know-how acquired by the author in the last eight years working with satellite and ground-based SAR data. The second objective is presenting two innovative algorithms for deformation measurements with GB-SAR data, which represent the most original part of this dissertation. The first one addresses one of the critical aspects of the interferometric SAR data, which is due to the ambiguous nature of the phase measurements: the phase unwrapping. As discussed later in this document, the process of phase unwrapping is one of the main source of errors in GB-SAR interferometry. The proposed algorithm detects and, if possible, corrects the errors related to phase unwrapping. The second algorithm is focused on the GB-SAR long-term monitoring. The algorithm proposes a new approach for exploiting the GB-SAR data based on the use of the amplitude component of the SAR images. The approach, which is called non-interferometric GB-SAR, resolves two important limitations of GB-SAR interferometry: it does not suffer phase ambiguity limitations; and it is not influenced by the atmosphere changes occurring between data acquisitions. In addition, the algorithm yields 2D deformation measurements, which represents an improvement with respect to the mono-dimensional measurements coming from standard SAR interferometry. It is worth mentioning that this approach is undergoing the review process to get a European patent (Crosetto and Monserrat, 2011).

The document is structured in four main chapters followed by the conclusions. The Chapter 2 provides an overview of GB-SAR interferometry. It describes the characteristics of GB-SAR imagery, the principle of GB-SAR interferometry and its main applications: the generation of digital surface models and deformation measurement. The latter application is then discussed in detail, introducing the aspects that are the basis of the subsequent chapters. The Chapter 3 describes the GB-SAR processing chain for deformation measurement and monitoring developed at TA. For each step of the procedure the key aspects are discussed, an algorithm is proposed and its results are illustrated by using real data. The second part of the chapter outlines some aspects related to the precision and accuracy of the GB-SAR data. The Chapter 4 presents a new method, named 2+1D phase unwrapping, which addresses one of the most critical steps of SAR interferometry, i.e. the estimation of phase ambiguities or phase unwrapping. The method offers an improved alternative to the standard procedure described in Chapter 3. The chapter starts with the algorithm description, which is followed by the discussion of its performances based on a simulated dataset, and concludes with the analysis of a comprehensive real case study, where the results from the standard procedure from Chapter 3 and the new one are compared. To conclude, the Chapter 5 presents a new procedure for measuring deformation with GB-SAR data using a non-interferometric approach. The chapter starts with the detailed description of the proposed procedure, which is followed by a discussion of the key technical aspects of its implementation. The last two sections are devoted to discuss the results of several validation experiments and to show the use of the procedure in a real case study devoted to landslide monitoring.

Chapter 2

Ground-based SAR interferometry

In the last years the Ground-Based Synthetic Aperture Radar (GB-SAR) has gained an increasing interest as a deformation measurement and monitoring tool. The GB-SAR is a radar-based terrestrial remote sensing imaging system (Rudolf et al., 1999; Tarchi et al., 1999). It consists on a radar sensor that emits and receives a burst of microwaves, repeating this operation while the sensor is moving along a rail track (Bernardini et al., 2007). The imaging capability is achieved by exploiting the Synthetic Aperture Radar (SAR) technique, e.g. see Hanssen (2001). The length of the rail determines the cross-range resolution of the acquired images: the longer the rail, the higher the cross-range resolution. Figure 2.1 shows a scheme of a GB-SAR system with its four main components: the radar head (sensor module), the rail (movement module), the power supply module and the computer for image acquisition control and data storage.

The GB-SAR is a coherent system, i.e. it measures the phase of the radar signal, which can be exploited, by using interferometric techniques, to derive information on the deformation and topography of the measured scene. The high sensitivity to small deformations, the long range of the measurements (up to some kilometres) and the imaging capability, which allows the system to perform a vast number of measurements, are interesting characteristics that make the GB-SAR system complementary to a number of other deformation measurement techniques. In the last decade a number of GB-SAR systems have been developed and used in different types of applications, like landslides, dams and glacier monitoring. Although the GB-SAR offers high potentialities for deformation monitoring, obtaining appropriate deformation estimates it is not a straightforward process. In fact, in order to properly estimate deformations the SAR data have to be processed and analysed according to a correct procedure, which takes into account the specificity of the data at hand.

This section provides an overview of GB-SAR interferometry. First, some GB-SAR principles, including the radar working principle and the concept of SAR, are recalled. Secondly, the main characteristics of GB-SAR imagery and the principle of GB-SAR interferometry are described. Then, the two main GB-SAR interferometry applications are discussed: Digital Surface Model (DSM) generation and deformation measurement. The latter one is then analysed in detail by introducing all the general and technical aspects that are the basics of the subsequent chapters.

2.1. GB-SAR principles

This section introduces the main working principles of a GB-SAR system by making explicit reference to a specific GB-SAR implementation, the IBIS-L system, which has

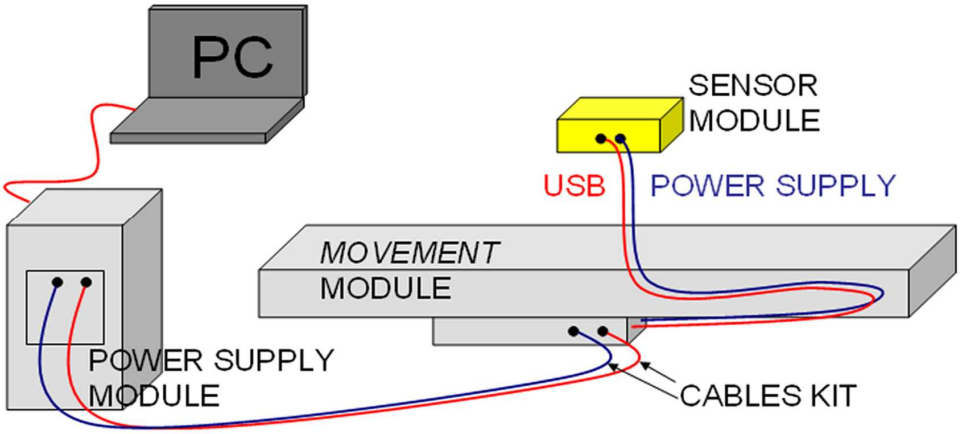

Figure 2.1: Main components of a GB-SAR system. Source: IDS Ingegneria dei Sistemi SpA.

been developed by IDS Ingegneria dei Sistemi SpA. in collaboration with the University of Florence. Most of the GB-SAR data analysed in this dissertation were acquired by this system. However, the results discussed and the algorithms proposed are system independent. It is worth noting that similar working principles are used by other existing systems, e.g. see Antonello et al. (2003), Noferini et al. (2005a), Pipia et al. (2006 and 2008) and Zhou and Motoyuki (2003). Werner et al. (2008) describe a similar system, which, however, does not use the SAR principle. An in depth description of the sensor IBIS-L can be found in Bernardini et al. (2007). This section is divided into two main parts: the GB-SAR working principle and the characteristics of GB-SAR images.

2.1.1. Radar and SAR working principles

The word Radar is the acronym of RAdio Detection And Ranging. The first radars were developed for military purposes, even though nowadays they are used for a broad set of civil applications, like navigation, air traffic, weather predictions, earth observation, etc. A classification of different types of radars can be found in Skolnik (1991).

The basic operating principle of the radar is the emission of pulses of energy and the collection of the energy reflected by the illuminated objects or targets, see Figure 2.2. The radar, located on the left part of the scheme, emits a pulse of duration τ at time t_0. The emitted energy travels through the environment at the velocity of the light, approximately at 299792,458 km/s. This pulse interacts with the illuminated object, the airplane, and a portion of the emitted signal is reflected back towards the radar arriving at time t_0+T_0. It is possible to derive the distance R between the sensor and the target from T_0:

$$R = \frac{c * T_0}{2} \tag{2.1}$$

where c is the speed of light, T_0 is the pulse time of flight, and the factor two reflects the two way path, radar-target-radar, of the pulse. As mentioned above, the radar systems are ranging systems. Their capability of distinguish between two objects located at different distances from the instrument is usually expressed by the range resolution ΔR, which is given by:

$$\Delta R = \frac{c * \tau}{2} \tag{2.2}$$

where τ is the duration of the emitted pulse. It is worth noting that different objects located at the same distance from the radar can not be distinguished.

A single acquisition with a radar system only provides information in one dimension: the system only resolves targets in the range direction. The capability of the radar systems to resolve targets in the direction perpendicular to this one is expressed by the cross-range resolution. This resolution is basically a function of the radar antenna length: the longer the antenna, the higher the cross-range resolution. A powerful way to obtain high cross-range resolutions without using long antennas is using the Synthetic Aperture Radar (SAR) technique. The SAR technique is based on the combination of multiple coherent range images of the same object taken from slightly different positions, which results in an image as it would have been seen by a long real aperture antenna. A technical description of the technique can be found in Curlander and McDonough (1991).

The GB-SAR obtains the synthetic aperture by exploiting the movement of the sensor along a rail, see the “movement module” in Figure 2.1: the sensor moves in a "stop and go" mode, acquiring data at each step. All the acquired mono-dimensional images are then compressed in a single two-dimensional image. The achievable cross-range resolution is given by:

$$\Delta\theta \approx \frac{\lambda}{2L} \tag{2.3}$$

where $\Delta\theta$ is the angular resolution, λ is the radiation wavelength and L is the length of the rail. Note that the angular resolution entails that the size of the pixel footprints in cross-range increases with the distance from the sensor.

2.1.2. GB-SAR image description

The raw data collected by the GB-SAR need to be post-processed in order to obtain the final GB-SAR images. This post-process is called image focusing and it mainly involves generating the image from all the data collected during the movement of the sensor along the rail. Two different examples of GB-SAR focusing algorithms are described in Fortuny-Guash and Sieber (1994) and Fortuny-Guash (2009). The final result

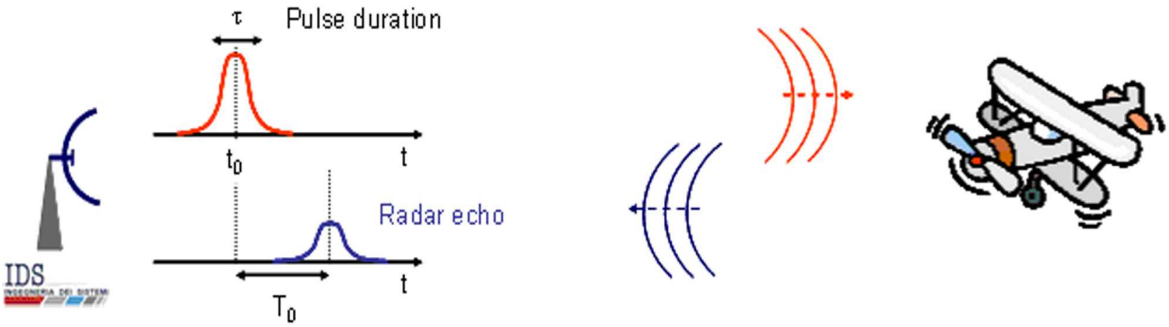

Figure 2.2: Scheme of the radar working principle**.** The radar is located on the left side, while the illuminated object in this case is an airplane. Source: IDS Ingegneria dei Sistemi SpA.

is a two dimensional complex image where each pixel contains the in-phase (I) and the quadrature (Q) components of the radar signal, which can be directly transformed in the amplitude (A) and the phase (φ) using these relations:

$$\varphi = \tan^{-1}\left(\frac{Q}{I}\right) \tag{2.4}$$

$$A = \sqrt{I^2 + Q^2} \tag{2.5}$$

The amplitude is directly related to the power of the scattered signal and is typically used for interpretation of the scene. This is an important aspect provided that the GB-SAR geometry often hampers a straightforward image interpretation. In addition, as it is described in Chapter 5 of this dissertation, the amplitude image can be exploited to derive geometric information of the observed scene. In particular, by using GB-SAR images acquired over time, the amplitude can be used to estimate deformation of the observed scene. The phase component contains the geometric information related to the sensor to target distance, which can be exploited either for deformation measurement or DSM generation purposes. The exploitation of the phase is treated in detail in the following section.

The GB-SAR image geometry is the result of a regular sampling in range coupled with a constant angular sampling. For this reason, the typical visualization of the GB-SAR images uses a polar grid with a constant sampling step in range ΔR and a constant angular step $\Delta\theta$ in cross-range. By contrast, in this dissertation the images are represented as rectangular regular grids, where the pixels are simply ordered according to their columns, x, and lines, y. Starting from the column and line pair of the pixel (x, y) the corresponding polar coordinates (r, β) can be computed by means of the following relation:

$$\begin{aligned} r &= y * \Delta R \\ \beta &= (x - x_c) * \Delta\theta \end{aligned} \tag{2.6}$$

where r is the sensor to pixel distance, β is the angle between the column of the given pixel and the central column of the image, x_c.

A GB-SAR amplitude image represented using a rectangular grid (top) and a photograph of the measured area (bottom) are shown in Figure 2.3. The amplitude image is a black and white image. The black areas of the amplitude image are areas providing a weak response to the radar and the white ones those with strong response. The interpretation of the amplitude image is not straightforward. The green circles highlight corresponding areas in the amplitude image and in the photograph. The identification of common structures eases the correct interpretation of the whole scene. For instance, the circle 4 corresponds to a couple of big cranes, while the circle 5 corresponds to the dike located in the far range of the scene. This dike in the radar image has a parabolic geometry due to the ranging nature of GB-SAR images and the fact that the central part of the dike is closer to the radar than its lateral parts. The circle 3 represents some electrical installations that show a regular pattern in the amplitude image. Finally, several horizontal lines can be observed in the GB-SAR amplitude image. These lines are the effects of strong reflectors which are not well focused in the cross range direction. These effects can be reduced by using different types of filtering during the image focusing process.

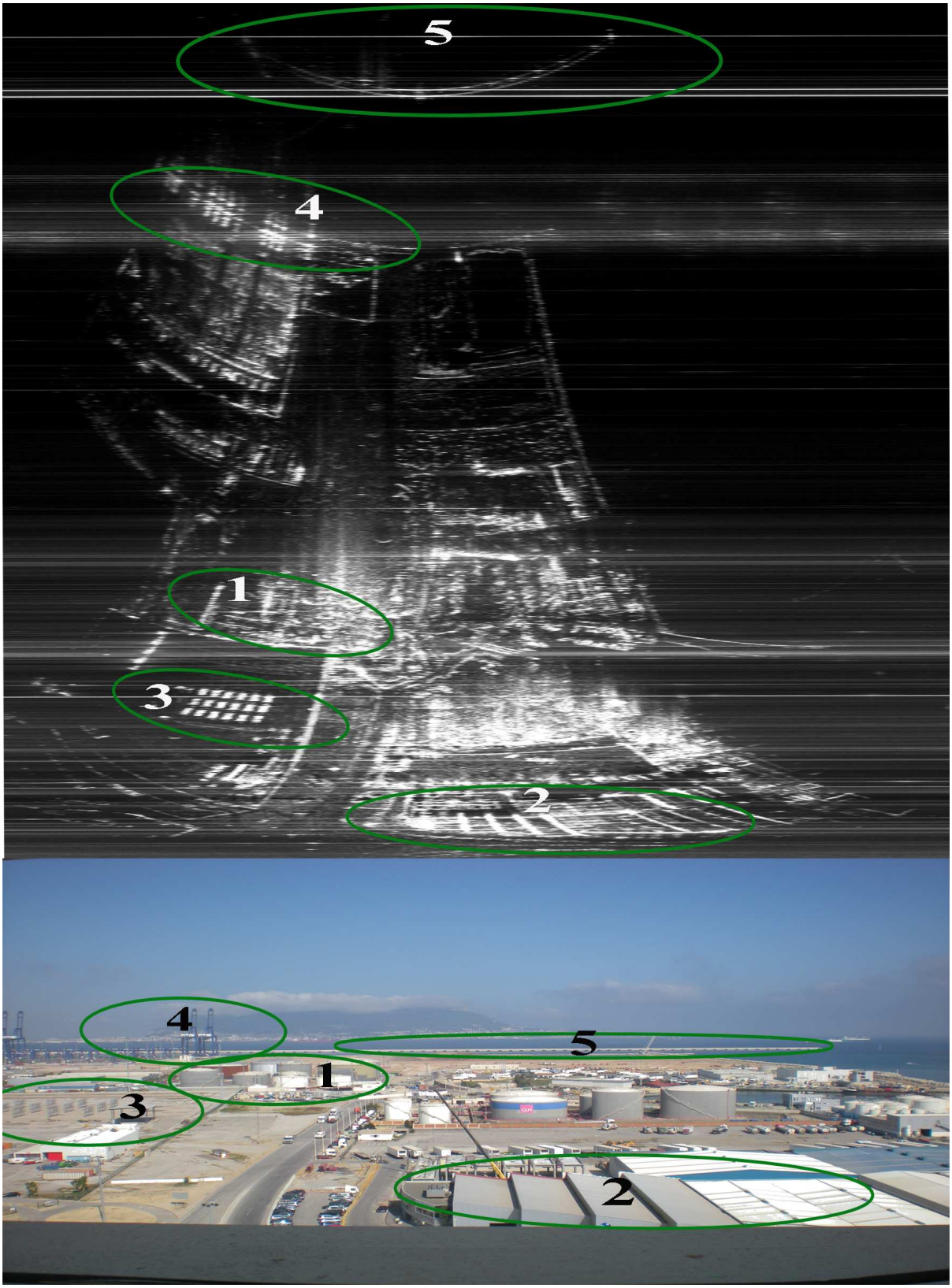

Figure 2.3: GB-SAR amplitude image (top) and photograph of the same scene (bottom). Some key structures of the scene are identified in both the amplitude image and the photograph in order to illustrate the complexity associated with GB-SAR image interpretation.

2.2. GB-SAR interferometry

As previously mentioned, the phase of a given SAR image contains the geometric information related to the distance between the radar and the different objects of the measured scene. This information can be exploited by using the interferometric technique, which is based on the exploitation of the phase difference between at least two GB-SAR images of the same object, which are usually acquired at different moments in time. Let's consider the phase φ_1 and φ_2 of two homologous pixels (i.e. pixels that correspond to the same physical object) from two images acquired at different times or from different positions:

$$\begin{aligned} \varphi_1 &= \varphi_{geom-1} + \varphi_{scatt-1} = \frac{4\pi \cdot R_1}{\lambda} + \varphi_{scatt-1} \\ \varphi_2 &= \varphi_{geom-2} + \varphi_{scatt-2} = \frac{4\pi \cdot R_2}{\lambda} + \varphi_{scatt-2} \end{aligned} \tag{2.7}$$

where R_1 and R_2 are the sensor to target distances at each acquisition, φ_{scatt} is the phase shift generated during the interaction between the microwaves and the measured object, λ the wavelength of the emitted signal, and the factor 4π is related to the two way path, radar-object-radar.

The interferometric phase $\Delta\varphi_{21}$, i.e. the phase difference between both acquisitions is given by:

$$\Delta\varphi_{21} = \varphi_2 - \varphi_1 = \frac{4\pi \cdot (R_2 - R_1)}{\lambda} + (\varphi_{scatt-2} - \varphi_{scatt-1}) \tag{2.8}$$

Ideally, assuming that the shift phase component φ_{scatt} remains constant between the two acquisitions (i.e. its variation over time is negligible) we can simplify the Equation 2.8 to:

$$\Delta\varphi_{21} = \varphi_2 - \varphi_1 = \frac{4\pi \cdot (R_2 - R_1)}{\lambda} \tag{2.9}$$

This equation shows that the main interferometric observable, i.e. the interferometric phase $\Delta\varphi_{21}$, is directly related to the difference of the sensor to target distances, R_1 and R_2. Note that this relation holds for every pair of pixels of the two images. The image that contains, for each pixel, the interferometric phase of a given image pair is named interferogram. Figure 2.4 shows an example of interferogram over an open pit area with its associated amplitude image. The interferogram is colour-coded between $-\pi$ and π and the colours represent the phase changes. Although the above equation is valid in an ideal case, in practice, other important components of the interferometric phase have to be considered:

$$\Delta\varphi_{21} = \varphi_2 - \varphi_1 = \frac{4\pi \cdot (R_2 - R_1)}{\lambda} + (\varphi_{atmo2} - \varphi_{atmo1}) + \varphi_{noise} \tag{2.10}$$

where φ_{atmo2} - φ_{atmo1} is the phase component due to the atmospheric effects on the signal propagation in both images and φ_{noise} is the noise phase component, due to the difference on the phase shifts, φ_{scat2} - φ_{scat1}, and other noise sources, like instrumental noise, etc. In the interferogram shown in Figure 2.4 can be distinguished the areas with high level of noise from those with low noise.

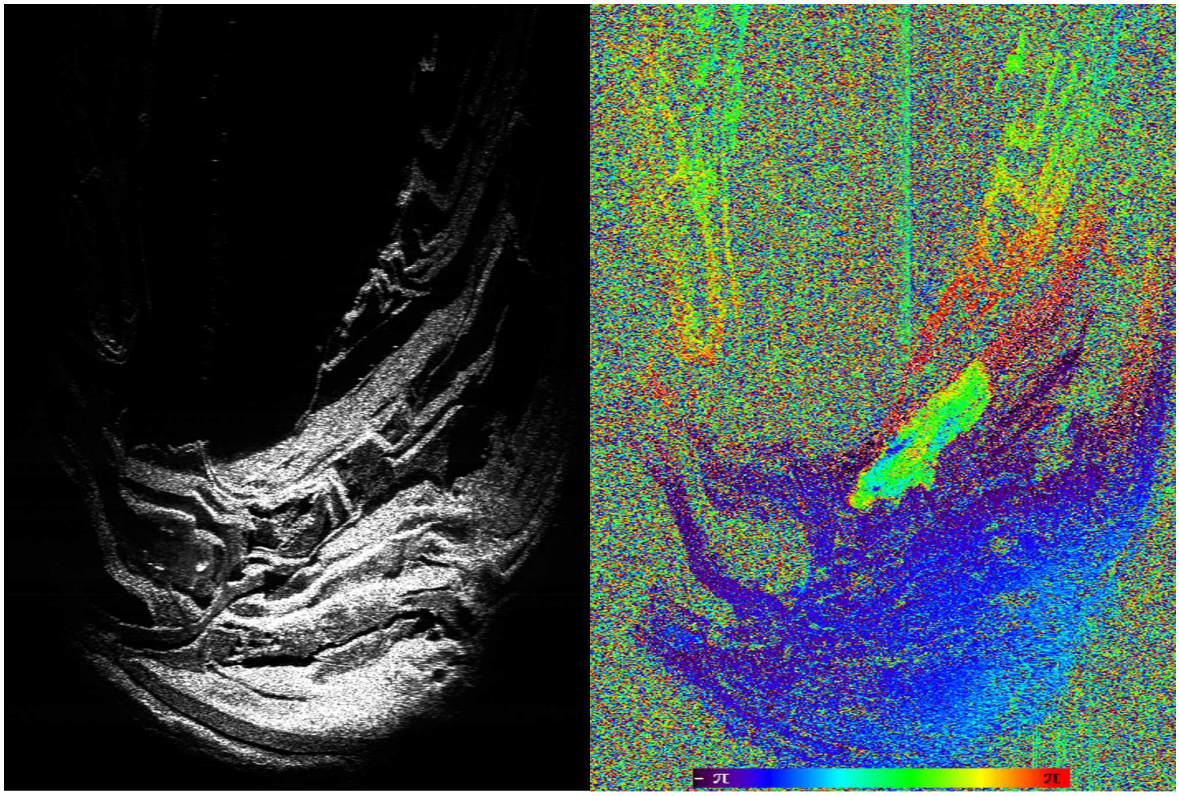

Figure 2.4: GB-SAR amplitude image (left) and associated interferogram (right). The interferogram, with phase values that range between [-π, π], is colour-coded. The black areas on the amplitude image, which correspond to weak measured signals, result in noisy phases in the interferogram.

The SAR interferometry has been widely used during the last 20 years, for DSM generation and deformation measurements, mainly using data acquired from spaceborne platforms (Rosen et al., 2000). The airborne-based SAR interferometry has also been used, at least at experimental level, to perform deformation measurements, e.g. see Perna et al. (2008), even though its main application is DSM generation, e.g. Wimmer et al. (2000) and Rosen et al. (2000). The GB-SAR interferometry is relatively more recent, and has been mainly used for deformation measurement purposes; see Luzi (2010) for a general review. However, it is worth mentioning other interesting applications, such as DSM generation (Antonello et al., 2003; Nico et al., 2004;Noferini et al., 2007; Rödelsperger et al., 2010a), and vegetation monitoring based on a polarimetric GB-SAR (Zhou et al., 2004).

Most of the GB-SAR studies published in the literature concern landslide monitoring, where the GB-SAR can offer good performances with respect to other measurement techniques, such as total stations or terrestrial laser scanner (TLS). Several authors, as Pieraccini et al. (2002), Leva et al. (2003), Tarchi et al. (2003) and Antonello et al. (2004), use a GB-SAR for slope monitoring in a continuous mode, i.e. leaving the instrument installed in situ during the whole monitoring period. Lingua et al. (2008) proposes an integration of TLS and GB-SAR data for landslide monitoring. Luzi et al. (2004) analyze the decorrelation of the phase due to atmospheric effects and instrumental noise while in Noferini et al. (2005a) the persistent scatter technique is used for slope instability monitoring. Herrera et al. (2009) describe the use of continuous GB-SAR data

for improving the forecasting model of a landslide located in the central Pyrenees. Del Ventisette (2011) uses the GB-SAR for an emergency landslide monitoring case in the Calabria region in Italy. Finally, Luzi et al. (2010a) describe a discontinuous landslide monitoring experiment based on the use of artificial reflectors. In this case, the instrument was employed in a number of short campaigns, revisiting the same site over time. This approach, which is widely used by many other techniques, is usually appropriate for the monitoring of slow or very slow displacement phenomena.

Tarchi et al. (1999) and Alba et al. (2008) address the use of GB-SAR for dam monitoring. This application takes full advantage of the GB-SAR imaging capability and its high sensitivity to small displacements. A review of the main pros and cons of using the GB-SAR technique for the monitoring of manmade structures can be found in Luzi et al. (2010b). Other works address the use of GB-SAR for single building monitoring like in Tarchi et al. (2000) or building damage detection as in Pieraccini et al. (2002).

The GB-SAR has been used to monitor a number of natural phenomena, like urban subsidence (Pipia et al., 2007), glacier monitoring (Luzi et al., 2007; Mecatti et al., 2007). Several works show the use of GB-SAR for monitoring volcano slopes. In Casagli et al. (2010) the GB-SAR is used as an operational early warning system over the Stromboli volcano, while the monitoring and the measured deformations occurred during an eruption of the Stromboli volcano are described in Casagli et al. (2009) and Antonello et al. (2009). Rödelsperger et al. (2010b) also describes the monitoring of the volcano caldera located on the Azores. Several works have been addressed to snow covered surfaces monitoring. Luzi et al. (2009) proposes the integration of TLS and GB-SAR for monitoring snow covered slopes. In Schaffauser et al. (2008) the TLS and GB-SAR are used for measuring the snow depth and snow water equivalent. In Martinez-Vazquez et al. (2005) the GB-SAR is used for monitoring the snow cover and Martinez and Fortuny (2007) use the GB-SAR data for detection and classification of snow avalanches.

To conclude, although there are not a lot of examples on the literature, GB-SAR has been successfully used as a tool for monitoring slopes in open pit mines. Mecatti et al. (2010) uses a GB-SAR system which automatically generates the DEM of the measured area for monitoring a quarry.

2.2.1. DSM generation with GB-SAR interferometry

This section describes how GB-SAR interferometry can provide information on the topography of the measured surface, generating a DSM of the observed area. A GB-SAR-derived DSM is certainly useful in all cases where there is no a priori available DSM or digital terrain model (DTM) of the measured area. In fact, as it is described later in this dissertation, the knowledge of a DSM of the monitored area is fundamental to properly geocode the GB-SAR data and, hence, correctly interpreting and exploiting the GB-SAR results. GB-SAR DSM generation is discussed in depth by different authors, see for example Antonello et al. (2003) and Noferini et al. (2007). Its principle is briefly outlined below.

Assuming than the observed scenario is stable (see Figure 2.5), if two images are taken slightly shifting the GB-SAR position, from M_1 to M_2, the interferometric phase contains a phase component which is due to the geometry of the observed scene, i.e. to the terrain topography of the measured scene. The topography is estimated pixel-wise by applying the following procedure:

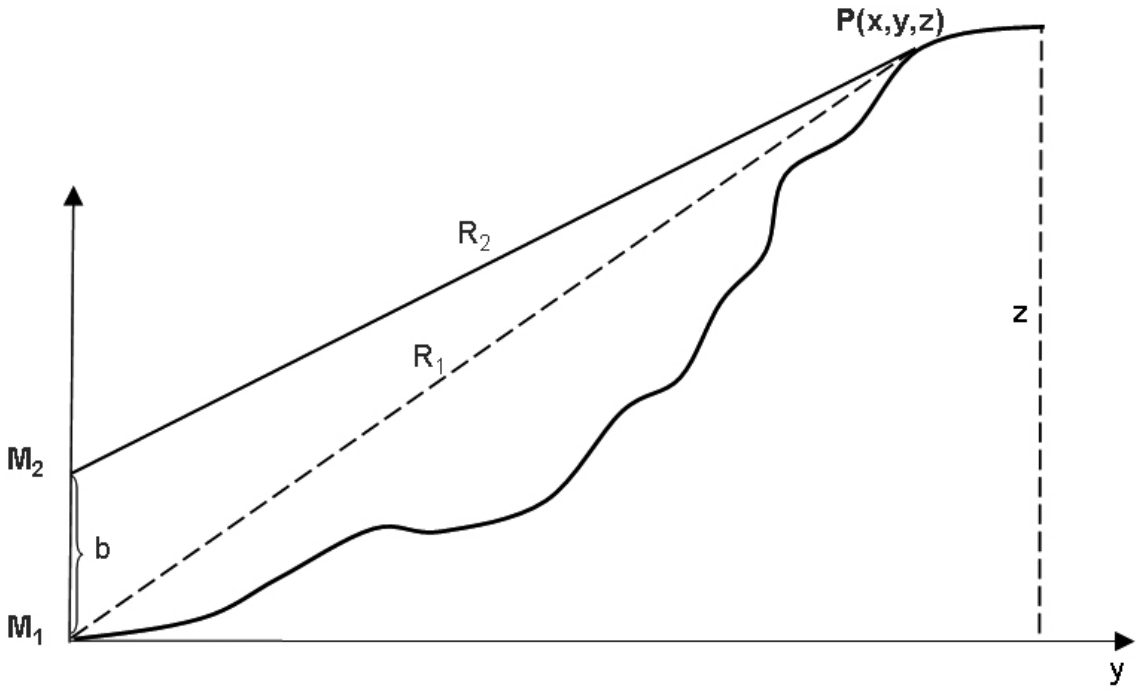

Figure 2.5: DSM estimation using GB-SAR interferometry. M_1 and M_2 are the positions of the GB-SAR at the first and the second acquisitions. R_1 and R_2 are the distances between the sensor and the point P at each acquisition, z is the height of the given point P and b is the distance (baseline) between M_1 and M_2.

1) Given the pixel (*line*, *column*) calculate the first sensor to target distance, R_1, from the radar measurement:

$$R_1 = \Delta R * line \tag{2.11}$$

where ΔR is the pixel spacing in range.

2) Using the interferometric phase compute the sensor to target distance, R_2, see Figure 2.5:

$$R_2 = R_1 + \Delta\varphi_{21} * \frac{\lambda}{4\pi} \tag{2.12}$$

3) The position of P can be derived by triangulation if the positions of the radar, M_1 and M_2, are known.
4) Repeat the above three steps for each pixel of the interferogram.

Some geometric considerations are made in the following. The relation between the topography and the interferometric phase can be written as:

$$\Delta\varphi_{21} = \frac{4\pi}{\lambda} \cdot [R_1 - R(b)] = \frac{4\pi}{\lambda} \cdot R_1 \cdot \left[1 - \sqrt{1 - \frac{2zb}{R_1^2} + \left(\frac{b^2}{R_1^2}\right)}\right] \tag{2.13}$$

where b is the distance (baseline) between M_1 and M_2 and z the elevation (height) of the point, see Figure 2.5.

Assuming that $(b/R) << 1$, and using the Taylor expansion of the square root, it can be derived:

$$z = \frac{\lambda}{4\pi}\frac{R_1}{b}\Delta\varphi_{21} \tag{2.14}$$

It can be noticed that the relationship between z and $\Delta\varphi$ strongly depends on the factor (b/R). From this equation, the standard deviation of the error in the elevation z can be derived:

$$\sigma_z = \frac{\lambda}{4\pi}\frac{R}{b}\sigma_{\Delta\varphi} \tag{2.15}$$

Table 2.1 shows different values of σ_z, assuming that λ is 1.76 cm, which corresponds to Ku-band GB-SAR data, and two different scenarios. The first one is a strong reflector, characterized by very low phase noise standard deviation ($\sigma_{\Delta\varphi} = \pi/100$ rad); in this case σ_z is rather small, being equal to 0.26 m in the worst scenario, i.e. at a distance of 1200 m. However, it has to be considered that in the practice such strong reflectors are very rare in a natural scene. In addition, it is worth underlining that a DSM needs to have a uniform coverage, which is only achievable using the majority of the pixels of a given interferogram: the performances of a DSM are rather a function of the average reflector available in a scene. Considering a typical surface, e.g. covered by grass, it is reasonable to expect an $\sigma_{\Delta\varphi}$ equal to $\pi/5$ rad. In this case, see Table 2.1, the expected σ_z is much higher, in the order of metres. For instance, at a distance of 1200 m the σ_z is equal to 5.2 m.

The values shown in Table 2.1 just provide rough information on DSM performances. With the typical reflectors of natural scenes σ_z is of the order of metres. This number could be improved by using sufficiently large baselines, but this has operational drawbacks. Given the above performances, it is often easy to get a DSM or a DTM of a given area with better characteristics than those derivable from GB-SAR interferometry. If this is not the case, GB-SAR DSM generation can provide an alternative solution. It is worth noting that all the considerations made in this section rely on Equation 2.9, which represents an ideal case: a reliable GB-SAR based DSM generation has to properly consider both the atmospheric phase component and the noise phase component included in Equation 2.10. A way to reduce the influence of both components is by generation the DSM using multiple interferograms of the same scene.

b [m]	R [m]	σ_z [m] with $\sigma_{\Delta\varphi} = \pi/100$ rad	σ_z [m] with $\sigma_{\Delta\varphi} = \pi/5$ rad
0.1	250	0.1	2.5
0.1	500	0.2	4.3
0.2	500	0.1	2.2
0.2	1200	0.3	5.2

Table 2.1: GB-SAR DSM generation: standard deviation of the error in elevation (σ_z) for two different targets, which are characterized by different phase noise standard deviation ($\sigma_{\Delta\varphi}$), at different distances (R) and using different baselines (b).

2.3. GB-SAR interferometry for deformation measurement

This section describes deformation measurement based on the GB-SAR interferometric technique. Figure 2.6 illustrates the measurement principle. Let's assume that we want to measure the displacements of point P. We install the GB-SAR system in front of it and obtain the first phase φ_M. Let's suppose that the point suffers a displacement d, and that a second GB-SAR measurement is made, obtaining a second observation φ_S at the time t_1. The interferometric phase can be calculated from the two measured phases:

$$\Delta\varphi_{MS} = \varphi_S - \varphi_M = \frac{4\pi * (SP' - MP)}{\lambda} = \frac{4\pi}{\lambda} * d \tag{2.16}$$

And then, the displacement d of P can be obtained by isolating d in Equation 2.16:

$$d = \Delta\varphi_{MS} * \frac{\lambda}{4\pi} \tag{2.17}$$

where λ is the wavelength of the used signal.

The above formulation is based on Equation 2.9, which does not consider disturbing effects, like atmospheric effects or phase noise. A more accurate approximation is given by Equation 2.10, where these effects are included. Furthermore, if we consider the possibility of removing and reinstalling the instrument we have to add a new term to the equation that include the phase shift due to the sensor repositioning. Finally, we have to consider the unwrapping term, $2k\pi$, which is discussed in Section 2.3.2. The final formulation is:

$$\Delta\varphi_{Int} = \varphi_{Geom} + \varphi_{Defo} + \varphi_{Atmo} + \varphi_{Noise} + 2k\pi \tag{2.18}$$

Chapter 3 is devoted to describe in depth all steps needed to properly separate each of the above components, obtaining therefore an estimate of the deformation. In the following sections some considerations about the logistics and the main limitations of the technique are addressed.

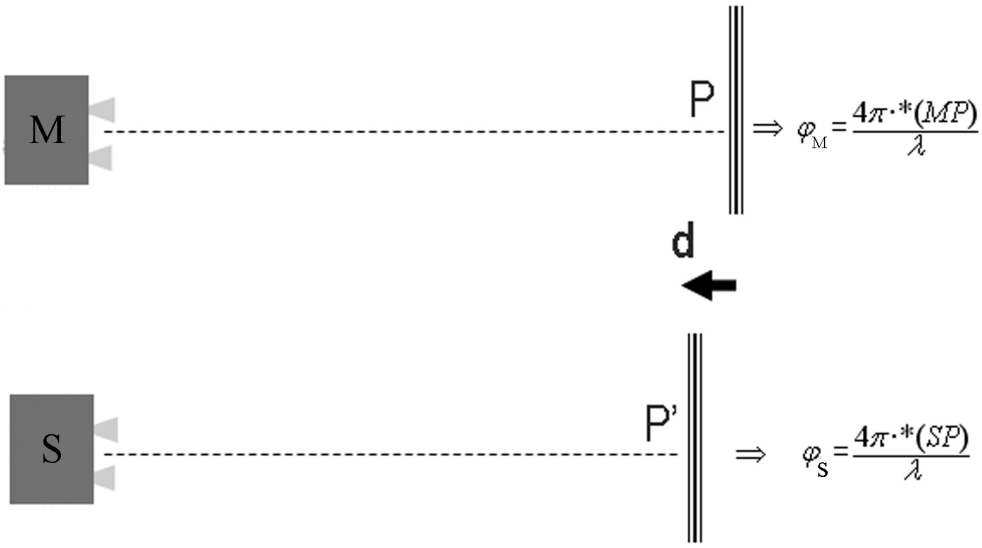

Figure 2.6: Working principle of GB-SAR interferometry for deformation measurement. A given point P, which undergoes a displacement d, is measured by GB-SAR twice, before and after the displacement.

2.3.1. GB-SAR deformation measurement: general aspects

In this section some fundamental aspects of GB-SAR deformation measurement, which have to be taken into account to properly understand and exploit GB-SAR based deformation measurements, are discussed. These aspects are listed below; the type of acquisition mode, continuous vs. discontinuous; the importance of the noise phase component; the use of artificial Corner Reflectors (CRs); the observed direction of GB-SAR measurements, i.e. the Line-of-Sight (LOS) direction; and the relative nature of the GB-SAR observed displacements.

- ***Type of acquisition mode: continuous vs discontinuous GB-SAR.*** GB-SAR interferometry can be exploited in two different ways: the continuous monitoring mode, by leaving the instrument installed in situ and acquiring data on a regular base, and the discontinuous mode, by installing the instrument at each campaign, revisiting a given site periodically. The continuous approach allows the user to have a "near real-time" monitoring of the site of interest, e.g. obtaining an image and hence a deformation estimate every few minutes. In this case, the component φ_{Geom} of Equation 2.18 does not exist. The continuous approach is appropriate to measure fast deformation phenomena, e.g. with displacements ranging from some mm/day to m/day, providing a monitoring tool that can support the management of emergency scenarios. On the other hand, when the movements are slower or when the "near real time" monitoring is not demanded, the continuous approach is not recommendable due to both logistic and cost reasons: in these cases, the discontinuous approach is more adequate. As it is discussed later in this dissertation, the discontinuous monitoring faces two main important problems: temporal decorrelation and aliasing.

- ***Noise phase component.*** Although the radar is an imaging system which delivers a regular grid of measured points, not all observed points can be exploited for deformation measurement. The exploitability of the points is mainly driven by the φ_{Noise} component: the higher the φ_{Noise}, the lower the capability to derive deformation information. The level of phase noise is mainly due to the difference in the phase shifts, φ_{scat2} - φ_{scat1} shown in Equation 2.8, which in turn depends on the physical and geometric characteristics of the measured objects and their changes over time and, specifically, over the time elapsed between the GB-SAR image acquisitions. The objects characterized by high interferometric phase quality are usually those that backscatter a lot of energy towards the radar and, at the same time, whose response does not undergo significant changes over time. By contrast, many types of surfaces provide either a very weak backscatter or their physical and geometric properties change critically over time. This is usually the case for different types of vegetated areas, while man made objects, metallic structures, rocks, etc. can maintain a good response to the GB-SAR signal even over long periods.

The quality of the interferometric phase is usually measured by the so-called coherence, see the next section: the lower the phase noise φ_{Noise}, the higher the coherence. It is important to emphasize that it is not possible to exploit the interferometric observations with low coherence and, as a consequence, no deformation measurement can be obtained. In other words, the availability of interferometric observations of sufficient

quality, where the φ_{Noise} component represents a sufficiently small fraction of the whole phase, is *conditio sine qua non* to perform GB-SAR based deformation measurement. Even though in many cases the coherence behaviour can be predicted *a priori*, in many others it is difficult to know it without performing the GB-SAR data acquisitions. In this sense, the technique can be seen as an "opportunistic deformation measurement method", which is able to measure deformation only over the available coherent objects.

- ***Artificial corner reflectors***. For the areas where it is clearly expected a low coherence behaviour and, at the same time, a deformation monitoring is needed, the use of artificial Corner Reflectors (CRs) can offer a solution. A CR is an artificial reflector with an optimal geometry from the radar point of view: its key characteristics, i.e. the geometric shape and metallic nature, guarantee a strong response to the microwaves. As example, Figure 2.7 shows CRs used on some of the experiments showed in this work. In terms of GB-SAR, a CR results in interferometric observations characterized by low φ_{Noise}, even in the discontinuous GB-SAR configuration. The use of CRs can guarantee the availability of measurements in those places where there is no or little coherence. However, this requires the accessibility to the studied area and an important effort in terms of *in situ* CR installation (Luzi et al., 2010a). This is the major disadvantage of CRs: they require evolving from "pure remote sensing" to a "hybrid remote sensing supported by in-situ installed devices". An interesting advantage of the CRs is that they allow measuring specific locations, which are supposed to be strategically located and materialized with respect to the expected deformation signal of interest. By contrast, as mentioned above, given the opportunistic nature of GB-SAR measurements, this cannot be guaranteed without using CRs. Figure 2.8 shows an example of deformation map obtained over an incoherent area (grass and forest land cover) using artificial CRs. In this case, the measurements over the CRs are mixed with those coming from reflectors available at the scene. The map shows some stable areas with high density of points, which mainly correspond to rocky and building areas. The moving area, located inside the red circle, is an area where the only possible measurements are those based on CRs. This deformation map was obtained from a 35-day interferogram.

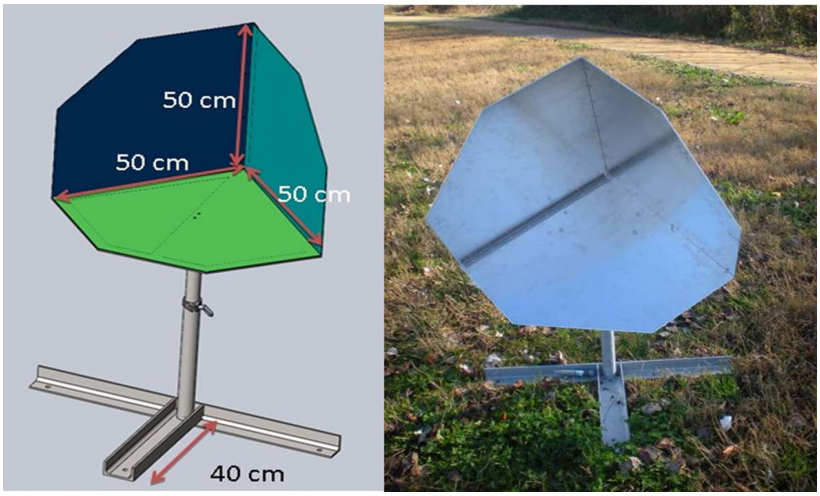

Figure 2.7: Example of corner reflector developed at the IG.

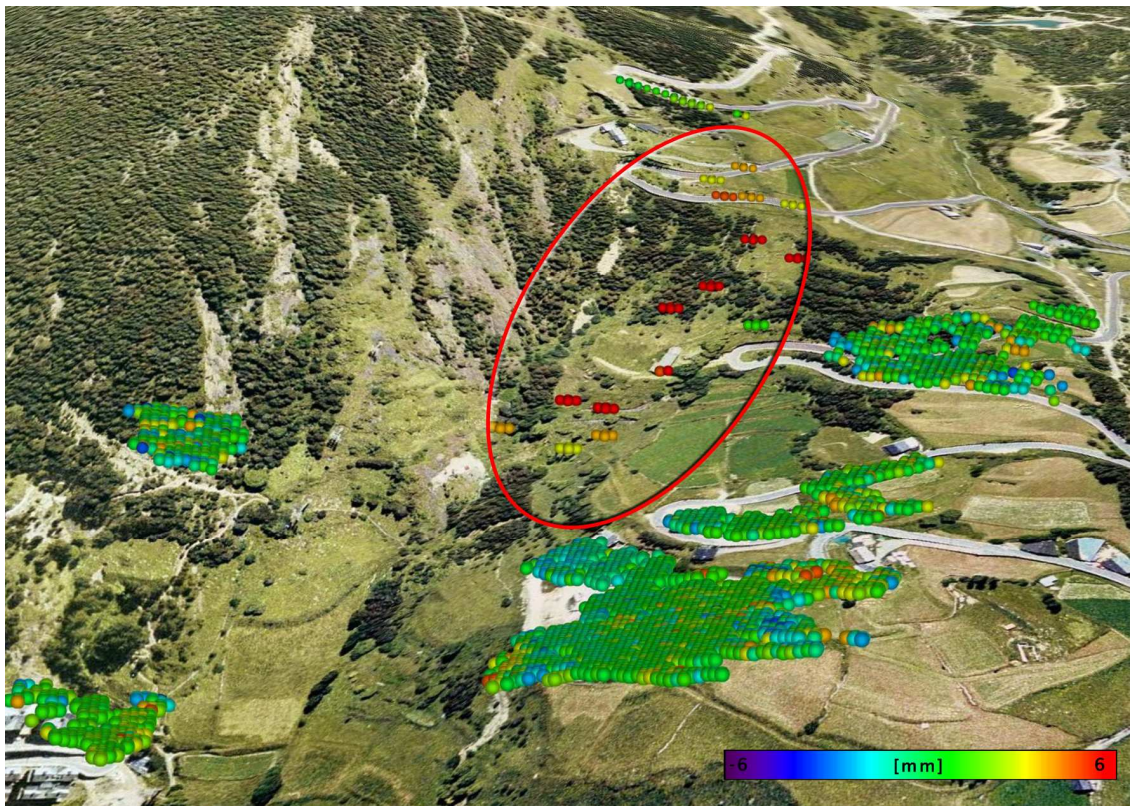

Figure 2.8: Deformation map obtained from an interferogram with temporal baseline of 35 days. The area bounded by the red circle is the area of interest. The measured points are artificial corner reflectors installed during the measurements.

- ***Deformation measurements in the radar line-of-sight.*** The GB-SAR deformation measurements refer to the line between the sensor and the measured object, the radar Line-of-Sight (LOS). That is, we only see the projection of the actual observed displacements along this LOS direction. This represents an important limitation of the technique with respect to all other techniques able to estimate the full 3D deformation field. In addition, this requires a particular attention in choosing the location of the GB-SAR: the ideal case is to have the LOS direction as parallel as possible to the displacement direction. The worst case scenario is when the LOS direction is perpendicular to the displacement direction. For instance, this occurs by observing a subsidence area from a neighbouring area located at the same height.

- ***Relative deformation measurements.*** GB-SAR deformation measurements are usually relative to a given reference point. In fact, even though the absolute measurements are certainly more interesting from the application viewpoint, they could theoretically be achieved if: (i) the GB-SAR could remain perfectly stable or its position over time was accurately known during the measurement; (ii) the atmosphere between GB-SAR and the scene was perfectly stable over time or its physical properties (humidity, temperature and pressure) accurately monitored over time and in the whole space between GB-SAR and the imaged scene. In most cases the above conditions are not satisfied and, for this reason, there is a need to identify a reference point or a set of reference points in the scene. This

usually implies a previous knowledge of the measured area: a wrong selection of the reference point can be misleading, when analysing results. On the other hand, if no *a priori* knowledge of the observed area is available, any arbitrary pixel in the scene can be chosen bearing in mind that all other measurements will refer to this point.

2.3.2. GB-SAR deformation measurement: two technical aspects

The objective of this section is to introduce two important technical aspects of the GB-SAR deformation measurement: the coherence of the interferometric observations, which was already mentioned in the previous section, and the phase unwrapping and associated problem of phase aliasing.

- ***Interferometric SAR coherence.*** As discussed in the previous section, obtaining coherent interferometric GB-SAR images over time is a necessary condition for GB-SAR deformation measurement. The complex coherence γ of a given pair of interferometric SAR images M and S is a statistical index that measures the degree of correlation between an image pair of complex SAR images:

$$\gamma = \frac{\mathrm{E}\left[M \cdot \mathrm{S}^{*} \right]}{\sqrt{\mathrm{E}\left[|\mathrm{M}|^{2} \right] \cdot \mathrm{E}\left[|\mathrm{S}|^{2} \right]}} \tag{2.19}$$

where $E[.]$ is the expected value and * the complex conjugate. The coherence is usually estimated by using windows of n by m pixels:

$$\gamma = \frac{\sum_{n}\sum_{m} M \cdot S^{*}}{\sqrt{\sum_{n}\sum_{m} |M|^{2} \sum_{n}\sum_{m} |S|^{2}}} \tag{2.20}$$

The reliability of the coherence depends on the number of pixels of the window. A comprehensive discussion of the coherence is provided in Rosen et al. (2000), Bamler and Hartl (1998) and Hanssen (2001). The absolute value of γ, which ranges between 0 and 1, provides fundamental information on the quality of the SAR interferometric phase. Bamler and Hartl (1998) show the relation between the standard deviation of the interferometric phase noise and the coherence, see Figure 2.9: the highest coherence values correspond to the lowest phase standard deviation.

The loss of coherence over time is also named temporal decorrelation. During the GB-SAR interferometric data analysis, a coherence threshold value has to be chosen: usually it represents a trade-off between the quality of the phase, which requires high coherence thresholds, and the spatial density of the selected pixels, which needs lower thresholds. Coherence and temporal decorrelation are discussed in several papers, e.g. Bamler and Just (1993), Ferretti et al. (2001) and Rosen et al. (2000).

It is worth emphasising that the coherence behaviour depends on the type of microwaves used. Most of the results shown in this dissertation were acquired with a GB-SAR system working with Ku-band data (λ = 1.76 cm). Over the same scenarios, systems working with longer wavelength, e.g. X-band, C-band, S-band, etc. can perform sensibly better both in terms of coherence and temporal decorrelation.

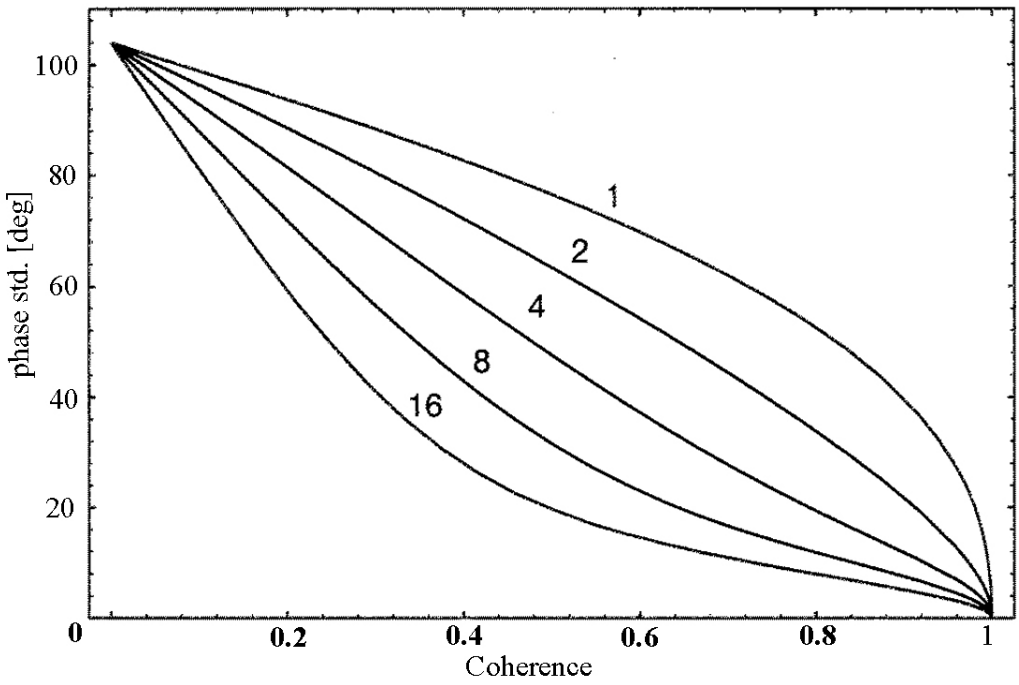

Figure 2.9: Relation between the standard deviation of the phase noise and the coherence for different number of interferogram looks, from Bamler and Hartl (1998).

The loss of coherence plays a different role in the continuous and discontinuous acquisition modes. Figure 2.10a shows a possible measurement scenario: a sliding slope that affects a highway. Figures 2.10b and 2.10c show the coherent points obtained for this area, which correspond to two interferograms with a temporal baseline of several hours and of one month, respectively. In the last case the vegetated area prevents the availability of dense set of coherent points: only the points measured on the man made rock wall remain coherent over one month time span. This example clearly shows how severe coherence loss can occur in the case of discontinuous GB-SAR applications.

- ***Phase unwrapping and aliasing***. As shown in Equation 2.4, the phase of a given GB-SAR image is calculated by using an inverse tangent. This implies that the phase values are known modulo 2π, ranging in the interval $[-\pi, \pi]$: these are the so-called wrapped phases. Figure 2.11 illustrates the concept of wrapped and unwrapped phases. Since the full interferometric phases are wrapped around the 2π interval, the full phase values need to be reconstructed by estimating the integer number of cycles to be added to their wrapped version:

$$\Delta\varphi_{Int\_unwrapped} = \Delta\varphi_{Int\_wrapped} + 2 \cdot k \cdot \pi \tag{2.21}$$

where k is an integer number. This operation is named phase unwrapping. In the context of this dissertation, the phase unwrapping discussed in this section is called 2D, because it concerns 2D fields of interferometric phases, which can have either a raster or vector structure. By contrast, the so-called 2+1D phase unwrapping discussed in Chapter 4 concerns stacks of interferograms that are unwrapped jointly, both in space and time. It is worth noting that, from the mathematical viewpoint, phase unwrapping is a hill-posed problem and, therefore, one of the most critical steps of SAR interferometry.

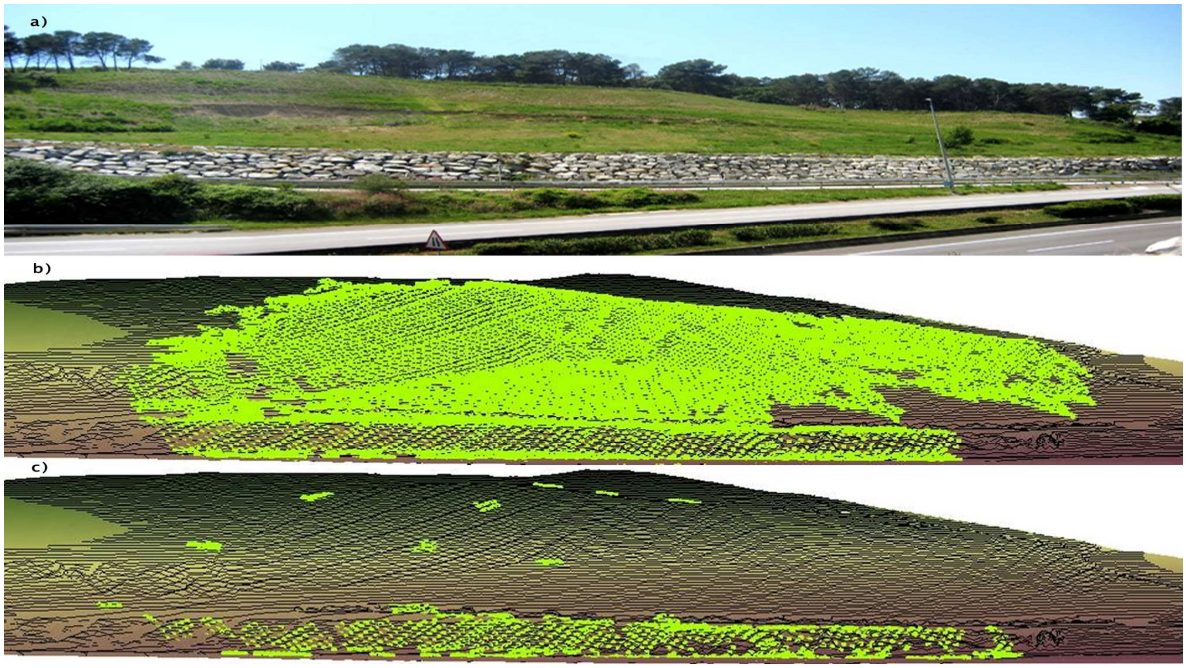

Figure 2.10: Role of coherence in the continuous and discontinuous acquisition modes. Photograph of the measured slope (a). The coherent points of a GB-SAR image pair acquired with few hours of time separation are shown in green (b). Same as (b), but with 1-month time separation (c).

The importance of phase unwrapping is clearly revealed by the considerable number of scientific publications devoted to this topic. In the last twenty years many phase unwrapping approaches have been proposed. Some of them are briefly mentioned below; for a systematic review see Ghiglia and Pritt (1998). The Ghost-line approach (also known as Branch-cut, Residue-cut, or Minimum Spanning Tree) is based on the direct integration of phase differences, avoiding some determined paths where aliasing occurs, see Goldstein et al. (1988). Another important type of phase unwrapping is based on the least squares (LS) principle (Ghiglia and Romero, 1989). Another method was derived from LS, which is based on the Green function formulation (Fornaro et al., 1996). The Minimum Cost Flow algorithm, presented by Costantini (1998), uses a L_1 norm estimation approach. Another minimization criterion using the norm Lp, with $0 \leq p \leq 2$, was suggested by Ghiglia and Romero (1994). Other different algorithms, e.g. those based on Kalman filter, the Region Growing approach, etc. are described in Ghiglia and Pritt (1998). An implementation of the Minimum Cost Flow method described in Constantini (1998) and Costantini et al. (1999) is used in this work.

As mentioned above, the phase unwrapping is a hill posed problem and thus an infinite number of different solutions can be found. This issue represents an important and intrinsic limitation of SAR interferometry, which has important consequences from the point of view of deformation measurement and monitoring. The majority of phase unwrapping algorithms are based on the assumption that the full interferometric phases vary smoothly over a given interferogram. More precisely, they are based on the following hypothesis on the unwrapped phases:

$$\left|\Delta\varphi_{Int\_unwrapped}(i,j) - \Delta\varphi_{Int\_unwrapped}(k,l)\right| < \pi \tag{2.22}$$

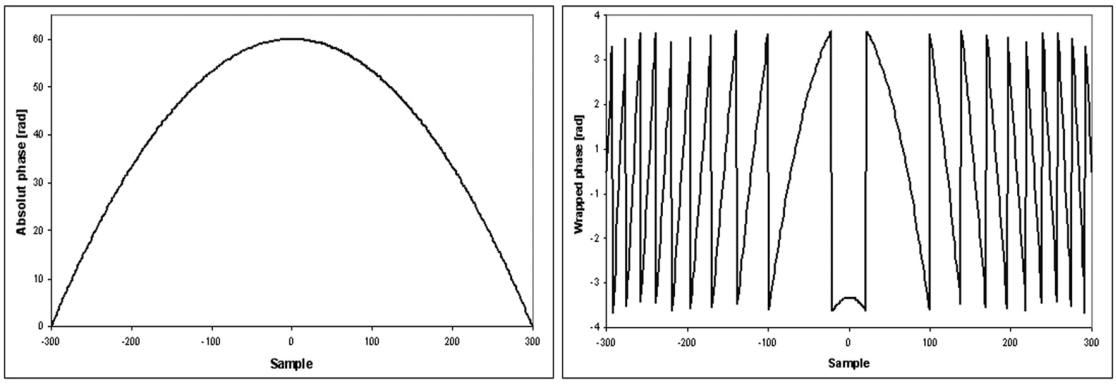

Figure 2.11: Phase unwrapping. Profile along a hypothetical interferogram with full interferometric phases, ranging approximately between 35 and 60 radians (left). This profile represents the unwrapped version of the profile shown on the right side, which contains wrapped phase values that range in the interval $[-\pi, \pi]$.

where (i,j) and (k,l) represent neighbouring pixels. Discontinuities in the full interferometric phases, where the phase variation between neighbouring pixels is greater than π radians, cause phase unwrapping or aliasing errors that are multiple of 2π and, as a consequence, severe errors in the deformation estimates. 2π correspond to a displacement of half wavelength which is about 9 mm in Ku band: the unwrapping related errors are at least one order of magnitude bigger than the precision of the deformation estimates. From the practical viewpoint, it is more informative to express the above condition in terms of displacement:

$$\left|Deformation\_\Delta t(i,j) - Deformation\_\Delta t(k,l)\right| < \frac{\lambda}{4} \tag{2.23}$$

where λ is the wavelength, and $Deformation\_\Delta t$ is the deformation occurred in the time interval between two image acquisitions. The condition is particularly severe for short wavelength, like the Ku band: differential displacements between (i,j) and (k,l) of 4.5 mm can be correctly estimated at the most (at least from the phase unwrapping viewpoint). In practice this requires to properly adjust the time interval, Δt. This condition is critical for many discontinuous GB-SAR applications, while in the continuous mode, where the time interval Δt can be as short as a couple of minutes, this issue does not represent a major limitation (4.5 mm in 2 minutes correspond to 13.5 cm/h, a displacement rate very seldom met in the practice).

To conclude, it is worth noting that Equations 2.22 and 2.23 refer to (phase or displacement) differences between pairs of neighbouring pixels. In this sense, two remarks are needed. The first one is that the concept of "neighbouring pixels" is strongly conditioned by the φ_{Noise} component. In low coherence areas, where many pixels have to be discharged, the distance between "neighbouring pixels" can be remarkably bigger than that of a highly coherent area, where all pixels can be used. The second remark concerns the difference between pixel pairs. Provided that a pixel usually has multiple neighbouring pixels, the above condition is somehow relaxed. In fact, many phase unwrapping algorithms use all the paths to reach a given pixel. Unfortunately, there are many situations where all the paths that connect a given set of pixels do not satisfy the Equations 2.22 and 2.23. In these cases, GB-SAR cannot usually provide a correct estimation of the deformation.

Chapter 3

Interferometric GB-SAR for deformation measurement

This chapter describes the GB-SAR data processing and analysis procedure used by the author for deformation measurement and monitoring. It covers the end-to-end sequence of steps that starts from survey preparation and finalizes with the generation of the geocoded deformation maps and the deformation time series. Some of the basic tools of the GB-SAR chain are shared with the IG data processing and analysis software chain used for satellite-based interferometric SAR and Persistent Scatterer Interferometry, e.g. see Crosetto et al. (2010) and Crosetto et al. (2011).

The chapter starts with an overview of the whole GB-SAR chain. The main data processing and analysis steps are then described, showing and discussing results based on different GB-SAR campaigns. The last section of the chapter outlines several aspects related to the precision and accuracy of the deformation measurements achievable with the proposed GB-SAR procedure.

3.1. The interferometric GB-SAR procedure

This section provides an overview of the GB-SAR procedure developed at the IG for deformation measurement. Most of these data processing and analysis steps are directly related to the main GB-SAR observation model already introduced in Chapter 2:

$$\Delta\varphi_{ij} = \varphi_{Geom} + \varphi_{Defo} + \varphi_{Atmo\_j} - \varphi_{Atmo\_i} + \varphi_{Noise} + 2k\pi \tag{3.1}$$

where $\Delta\varphi_{ij}$ is the interferometric phase computed with the master image j and the slave image i, φ_{Geom} is the phase term generated by removing and reinstalling the instrument, φ_{Defo} is the phase component related to the deformation occurred between the acquisition of the master and slave images, φ_{Atmo} is the atmospheric phase contribution, φ_{Noise} is the phase noise term and $2k$ is the phase unwrapping term, where k is an unknown integer number.

The entire process of deformation estimation aims to properly separate the deformation component from the other components shown in Equation 3.1, using a set of N GB-SAR images. This process involves a sequence of operations as shown in Figure 3.1. The following sections will deal with the main processing steps of the procedure:

- image coregistration,
- interferogram and coherence image generation,
- pixel selection,

- 2D phase unwrapping,
- phase integration,
- estimation of the atmospheric component,
- displacement computation and geocoding.

The remaining steps are not directly discussed in this chapter. The survey preparation and the data acquisition are partially discussed in Chapter 2, while the focusing of SAR images is a well documented process, e.g. see Fortuny-Guash (2009) and Curlander and McDonough (1991). The focusing implemented in the procedure here described is based on Fortuny-Guash and Sieber (1994).

To conclude, it is important to mention that even though data processing and analysis chain slightly differs for the continuous and discontinuous modes, it is basically based on the same tools. For this reason, the content of this chapter is valid for both types of acquisition mode.

3.2. Image coregistration

An interferometric analysis can only be performed if the SAR images used to generate the interferogram are properly coregistered, i.e. pixels with equivalent location in the two images have to match the same footprint on the ground. The coregistration step is fundamental in interferogram generation since it ensures that each ground target contributes to the same (range, azimuth) pixel in both the master and the slave images (Ferretti et al., 2007). This is a standard process in satellite-based SAR interferometry, given that satellite images only approximately cover the same area: they are usually acquired from different viewpoints and from not exactly parallel orbits. Different image coregistration algorithms can be found on the literature, e.g. see Lin et al. (1992). For a discussion of coregistration for SAR interferometry see Gabriel and Goldstein (1988).
From the GB-SAR point of view, image coregistration is mandatory in the discontinuous mode, where the GB-SAR is re-positioned at each campaign, especially in the cases where a “light positioning” is performed by simply materializing the GB-SAR location using some marks. Note that the “light positioning”, which can easily result in repositioning errors of several millimetres, is necessary in many practical application cases where it is not possible to build a concrete base or any other precise mechanical positioning structure. In addition, even in the cases where the GB-SAR position can be materialized mechanically, ensuring in principle an accurate repositioning, the coregistration is recommended in order to minimize the effect of any repositioning error that could occur. It is worth noting that a non perfect match of the GB-SAR position at the acquisition of two images causes two effects: coherence loss and the phase term φ_{Geom}, which is included in Equation 3.1.

To perform the coregistration, the transformation from the slave image geometry to the master geometry has to be found and then the slave image has to be resampled to the master geometry. This operation has to be carried out with sub-pixel accuracy in order to preserve the interferometric phase quality. In fact, a registration error of the order of one image pixel may yield a complete coherence loss. This issue prevents carrying out interferometric measurements using discontinuous GB-SAR without performing a coregistration. This is illustrated in Figure 3.2, which shows an interferogram generated by

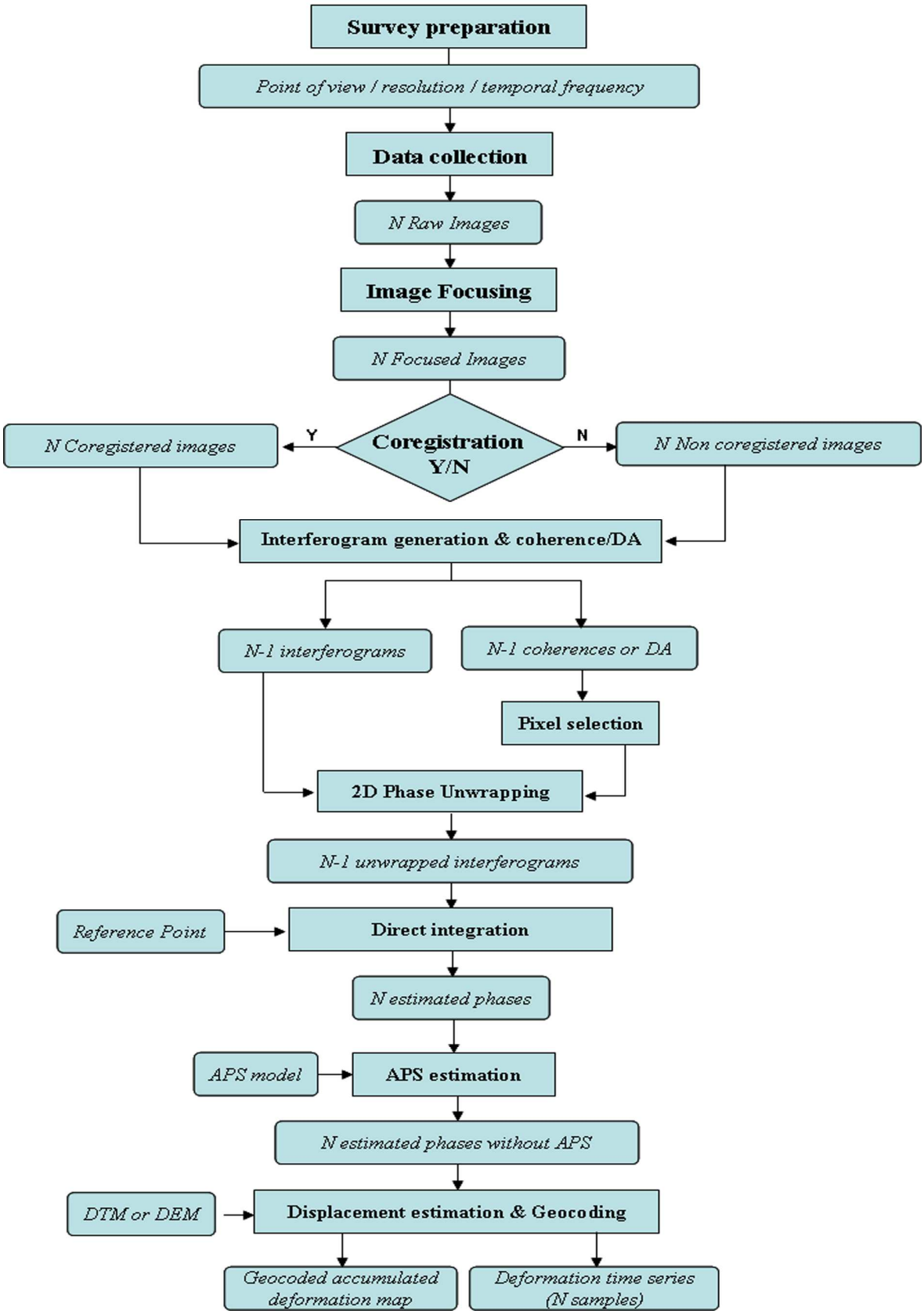

Figure 3.1: Flow chart diagram for deformation estimation with GB-SAR data.

using discontinuous GB-SAR without performing a coregistration. In the same figure is shown the interferogram computed from the same images, which were properly coregistered. The difference is evident and underlines the need of performing a good coregistration: the first interferogram is noisy and it is not possible to distinguish any structures, while the second one shows several coherent features where the phase can be exploited.

As mentioned above, when two GB-SAR images are acquired from non coincident viewpoints, an additional term in the interferometric phase, φ_{Geom}, appears (see Equation 3.1). An example of this term is shown in Figure 3.3, which corresponds to an image pair collected over the Eixample (Barcelona), rotating the GB-SAR about 2º-3º between the first and the second acquisitions. There is a strong phase pattern, even though the two images were correctly coregistered, which is due to the rotation of the sensor. It is worth noting that the coregistration operation makes the "supports" of two images geometrically identical, neglecting the errors associated with this operation. However, coregistration does not compensate for the φ_{Geom} phase term, i.e. it has to be properly considered in subsequent data analysis steps, see the APS estimation stage.

In principle, coregistration can be usually avoided when continuous GB-SAR data is used since the sensor remains stable during the acquisition period. However, it is necessary when measuring at long distances, to account for a particular type of image distortions, due to atmospheric variations during the acquisition of single images. Figure 3.4 describes this phenomenon. If the atmosphere does not vary during image acquisition, the refractive index (n_1) at the end of the acquisition will be the same as that at the beginning. In this case, the propagation paths Δr_1 and Δr_2 will be properly estimated, and the resulting image will not suffer any distortion due to atmospheric effects. On the other hand, if there is a variation in the atmosphere, there will be a change of the refractive index: n_1 at the beginning, and n_2 at the end. Since image formation assumes a constant refractive index (e.g. n_1), the distance Δr_1 will be properly estimated while Δr_2 will be underestimated (if $n_1 < n_2$). The resulting SAR image will provide a missed position for point p. This point will appear closer to the sensor than it actually is: the image will appear to have been formed by a linear aperture rotated by an angle ξ with respect to the previous acquisitions. This effect can, at least partially, be compensated by the image coregistration.

3.2.1. Image coregistration algorithm

This section describes the image coregistration procedure implemented in this chain. Let's consider two complex SAR images where the master image M is the reference image, and the slave image S is the image to be coregistered to M. The process of image coregistration involves three main steps, described below: image matching, transformation estimation and image resampling.

- ***Image matching***. Image matching involves the identification of common points in both images, estimating the image shifts, in azimuth and range, between the point position in both images M and S. The shift estimation can be performed using different methods, see Bamler and Eineder (2004). In the procedure at hand, the used method is the so-called Incoherent Correlation, which estimates the shifts by using the cross-correlation of the squared amplitudes of the two images.

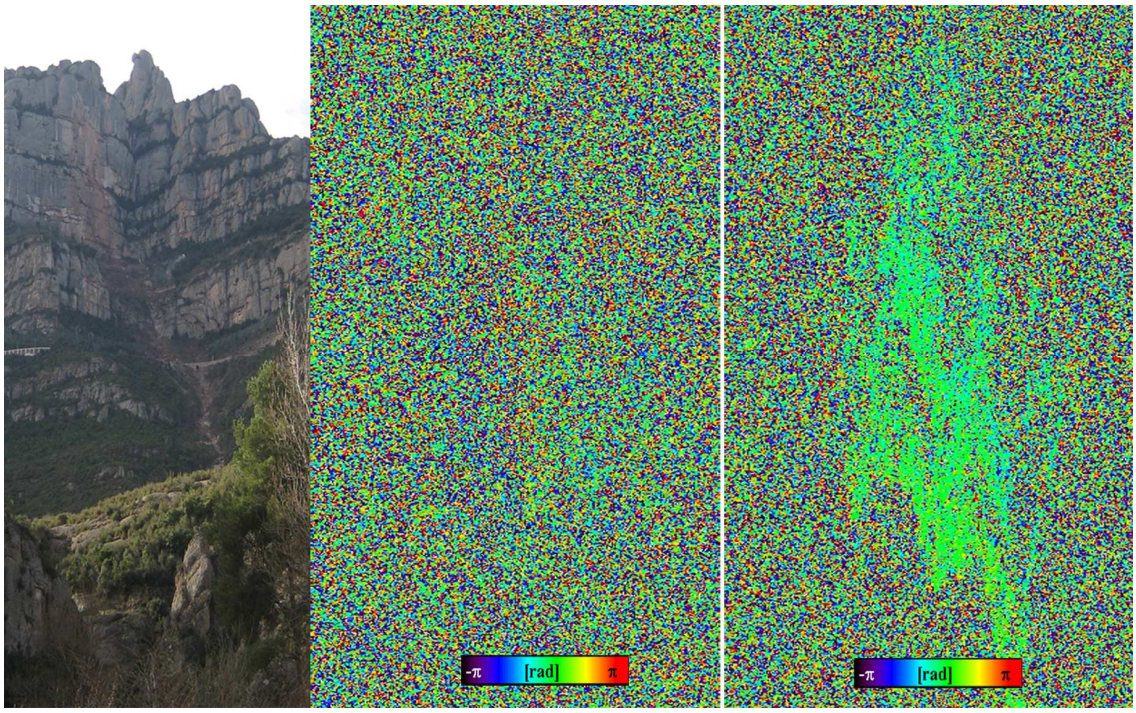

Figure 3.2: GB-SAR interferogram generated using two images from discontinuous GB-SAR and without coregistration (middle), and the interferogram computed from the same images but previously coregistered (right).

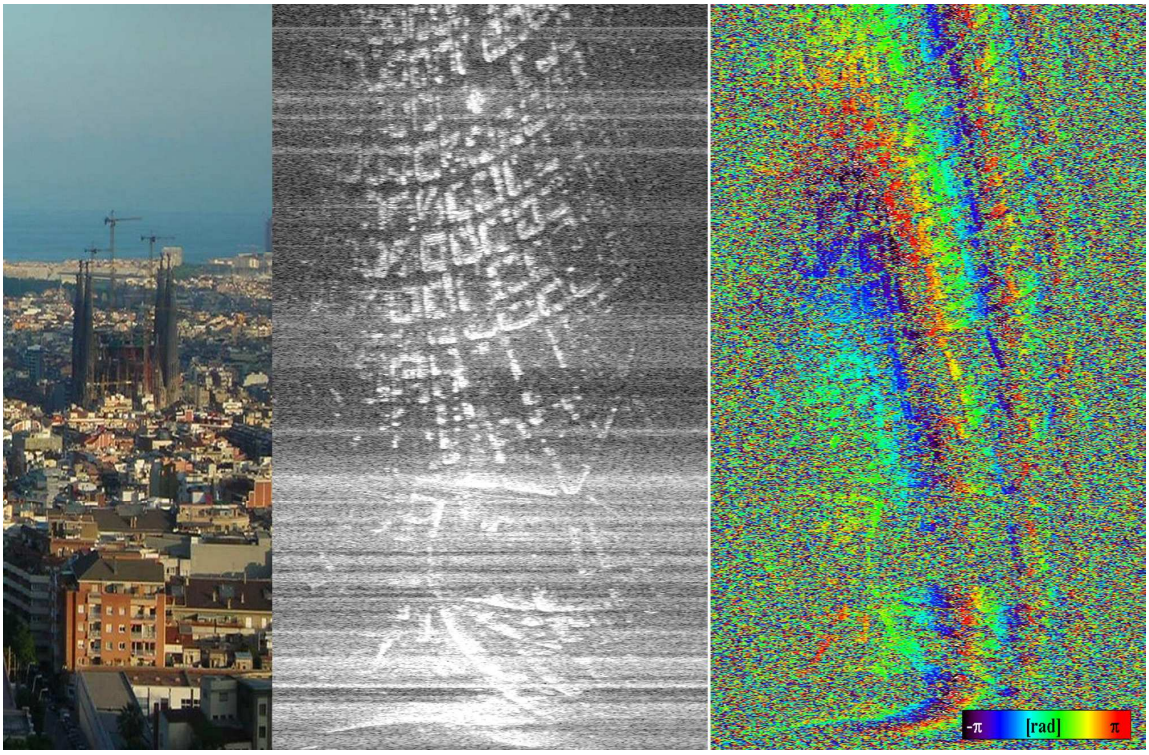

Figure 3.3: Example of φ_{Geom} phase term of an interferogram (right) and amplitude image of the same scene (centre). The interferogram comes from an image pair collected over a portion of Eixample (Barcelona), by rotating the GB-SAR of about 2º-3º between the two image acquisitions.

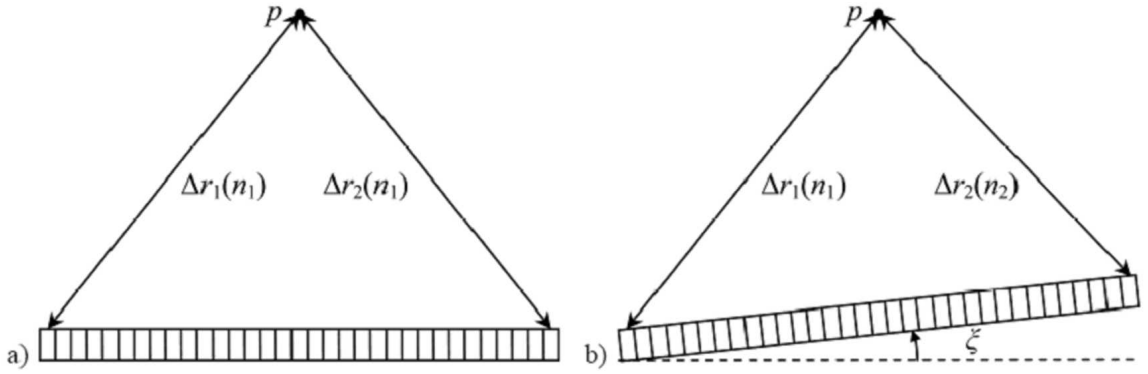

Figure 3.4: Image distortion due to atmospheric changes during the acquisition of a single image. Case with no changes in the atmosphere occur during image acquisition (left), and case where a change in the atmosphere, causes the image to appear as it was acquired from a rail rotated by an angle ξ with respect to the previous acquisitions, from Martinez-Vazquez (2008).

The maximum of the correlation function indicates the shift vector between S and M. When the correlation is higher enough, the estimated shifts can be obtained with a precision of up to 0.05 pixels (Hanssen, 2001). The estimation of the shifts is performed over a set of selected points of the master image M. The selection of the points has to guarantee a good spatial distribution in the whole scene in order to avoid systematic effects on the final interferogram or coherence loss. For each selected pixel $(x,\ y)_M$ of the master image, the estimated shifts are given by the 2D vector, $h_{xy} = (h_x,\ h_y)$, which maximizes the normalized cross-correlation function:

$$C(h_{xy}) = \frac{\sum_{i,j \in W_{xy}} \left[M(i,j) - \mu_M\right]\left[S(i-h_x, j-h_y) - \mu_S\right]}{\sigma_M \sigma_S} \quad .(3.2)$$

where W_{xy} is a n by m window centred in $(x,\ y)_M$, μ_M, μ_S, σ_M and σ_S are the means and the standard deviations of M and S in W_{xy}. The function C, which takes values between [0, 1], measures the degree of correspondence between M and S in W and W-h, respectively. By using this procedure, a shift in range, a shift in azimuth and its cross-correlation value is obtained for each selected pixel. The main input parameters for this step are the size of W_{xy}, the oversampling factor that will drive the resolution of the method, and the number of samples used in the oversampling. For GB-SAR data coregistration, typical values are a window size W_{xy} of 32 by 32 pixels, an oversampling factor of 16, and 8 samples for oversampling.

- ***Transformation estimation***. The transformation parameters between S and M are estimated in this step. The used model is a second-degree 2D-polynomial:

$$\begin{cases} p_x(x,y) = a_x + b_x \cdot x + c_x y + d_x x^2 + e_x \cdot x \cdot y + f_x \cdot y^2 \\ p_y(x,y) = a_y + b_y \cdot x + c_y y + d_y x^2 + e_y \cdot x \cdot y + f_y \cdot y^2 \end{cases} \quad (3.3)$$

where $(x,\ y)$ are the master image coordinates of a given point. The transformation parameters $(a_x,\ b_x,\ c_x,\ d_x)$ and $(a_y,\ b_y,\ c_y,\ d_y)$ are estimated by least squares. The observation model is:

$$\left.\begin{aligned} x_S &= x_M + p_x(x,y) + \xi_x \\ y_S &= y_M + p_y(x,y) + \xi_y \end{aligned}\right\} \tag{3.4}$$

where (x_S, y_S) are the image coordinates on the slave image of the point (x_M ,y_M) in the master image and (ξ_x, ξ_y) are the residual observation errors. Equation 3.4 can be rewritten in terms of the estimated shifts (h_x, h_y):

$$\left.\begin{aligned} h_x &= p_x(x,y) + \xi_x \\ h_y &= p_y(x,y) + \xi_y \end{aligned}\right\} \tag{3.5}$$

The observations are the estimated shifts obtained in the matching step. Only those pixels with high correlations are selected for the estimation: typically a cross-correlation threshold of 0.7 is enough for obtaining good parameter estimation. It is recommended to analyse the above residuals to obtain a good estimation. The following measures can be taken to ensure the quality of the estimation: (i) checking the distribution of the points: ideally they should be well distributed across the scene; and (ii) checking the distribution of the residuals, which should be uniformly distributed: the existence of clusters of high residuals can result in systematic effects in image coregistration.

- ***Resampling***. In this step, the (I, Q) value on the position (x_S, y_S) of the slave image S is calculated for every pixel (x_M, y_M) of the master image M. Different interpolation methods are discussed in the literature, e.g. Laakso et al (1996). The Truncated Sinc Interpolation has been selected for our procedure because it shows the better behaviour with respect to the phase, according to Hanssen and Bamler (1999), which discuss the influence of several interpolation kernels on the coherence. The size of the truncated sinc is one of the key inputs. The used kernel size is typically 8 pixels, which is good enough in terms of coherence (Hanssen and Bamler, 1999). The final output of this step is the transformation of the slave image S to the master geometry, i.e. each pixel (i,j) of the master and slaves images matches the same portion of terrain of the measured area.

3.3. Interferogram and coherence image generation

The main inputs for the deformation estimation procedure, the interferograms and the associated coherence images, are generated in this step from the stack of N coregistered GB-SAR images. Interferogram generation is preceded by the design of the interferogram network, which defines how the N images are connected through a set of M interferograms. The interferogram network design can be decided following different criteria; in the procedure here described M is equal to N-1, with the interferograms connecting consecutive images. This network entails that all images are interconnected using the minimum number of interferograms, i.e. it is a zero-redundancy network.

Each of the M interferograms is computed starting from the pair of complex SAR images, M and S. Even though each interferogram is a complex image, only the interferometric phase is usually computed:

$$\varphi_{MS} = \arg(M \cdot S^*) \tag{3.6}$$

where φ_{MS} is the interferometric wrapped phase (φ_M - φ_S), M is the master image and S^* is the complex conjugate of S. The result is an image where each pixel contains the wrapped difference of phases between the image M and the image S.

For each interferograms its corresponding coherence image is generated using Equation 2.20 and keeping the module of the complex coherence. The coherence images are then used to perform the pixel selection as discussed in the following section.

3.4. Pixel selection

As previously mentioned, the interferometric phase can only be exploited over a fraction of the measured pixels. The exploitability of a given pixel basically depends on the φ_{Noise} phase term: only those pixels whose interferometric phase is characterized by low φ_{Noise} have to be selected. Different selection criteria tailored to the application at hand can be used to select these pixels. Two selection criteria, the coherence-based and amplitude-based selection, are discussed below.

3.4.1. Coherence-based selection

The coherence is a statistical parameter that measures the degree of correlation between a pair of SAR images, which is directly related to the standard deviation of the interferometric phase noise. In this sense, high coherence values correspond to low phase noise standard deviation of the phases. This property can be directly used to perform the pixel selection. An example is shown in Figure 3.5, where it is evident that the noisy interferometric phases correspond to low coherence areas. It is worth to note that in this example, which concerns a 15-days interferogram of the Montserrat test site, most of the pixels have low coherence and hence noisy phases.

The challenge of the coherence-based selection is choosing the appropriate threshold to discriminate between "bad" and "good" pixels or, more precisely, between pixels that can be exploited to estimate the deformation and those that have to be discarded. Unfortunately, we do not have a fixed rule to choose the coherence threshold. Figure 3.5 shows three examples of pixel selection based on three thresholds: 0.85, 0.9 and 0.95. The first threshold select a lot of pixels in the noisy area: it is probably not sufficiently selective, while the last one is probably selecting pixels of good quality, at the expense of drastically reducing the number of selected pixels. Often the threshold is fixed by adjusting the trade-off between phase quality and density of the selected pixels, i.e. spatial density of the deformation measurement. An empirical way to check is to analyse the phase unwrapping results, which depend both on the quality of the phase and the pixel density.

Figure 3.6 shows a 35-days interferogram over the Canillo test site (Andorra), and the corresponding coherence image. Built-up areas, highlighted by green circles, basically remain coherent, while the rest of the scene, mainly vegetated areas, displays low coherence and noisy phases. In this type of scenes, using the discontinuous GB-SAR mode, even with relatively short temporal baselines, it is difficult to achieve reliable deformation measurements.

As already mentioned in Chapter 2, the loss of coherence usually increases with time and, thus, this issue is even more critical in discontinuous GB-SAR than in the continuous acquisition mode. Figure 3.7 illustrates how coherence loss increases even over relatively short time intervals and over built-up areas. In this case, which concerns the Port of Algeciras, there is a remarkable loss of coherence between a 10-minute interferogram and a 1-day one.

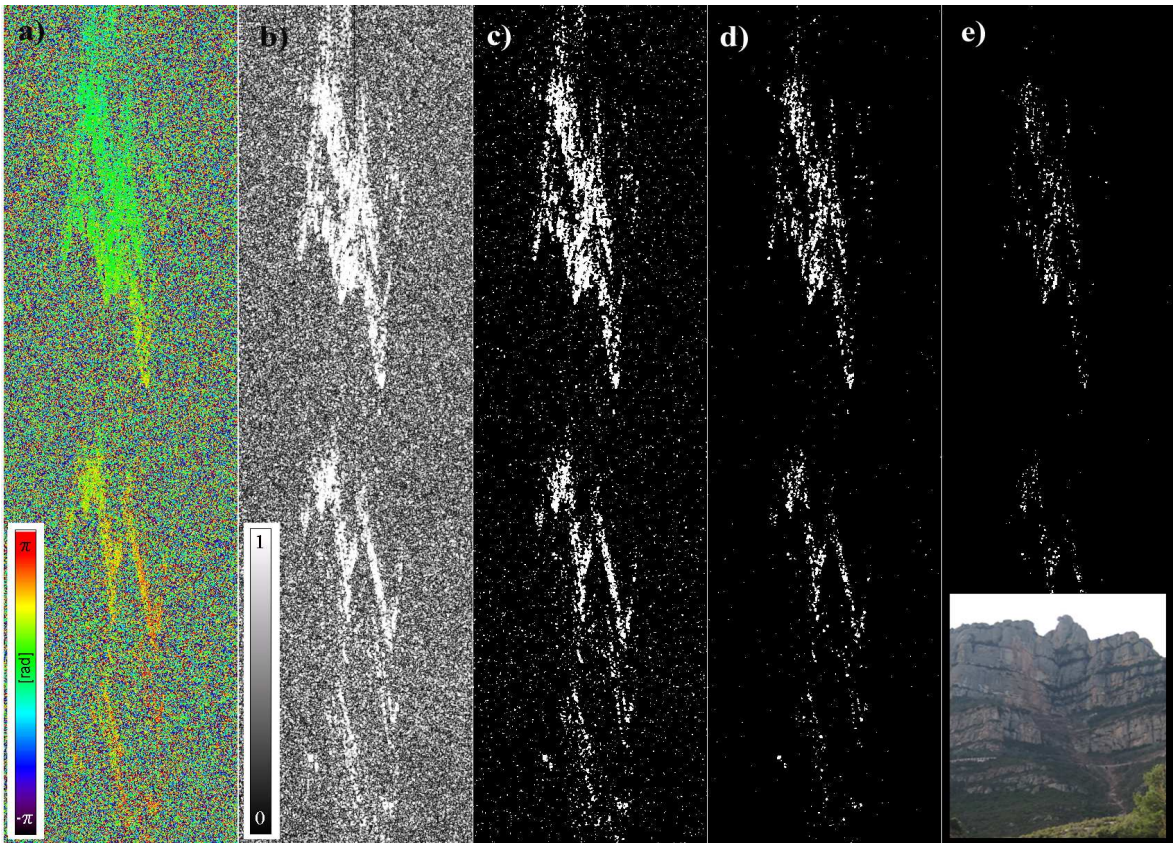

Figure 3.5: 15-days interferogram of the Montserrat area (a); corresponding coherence image (b). Pixels with coherence bigger than 0.85 (c), 0.9 (d) and 0.95 (e) appear white.

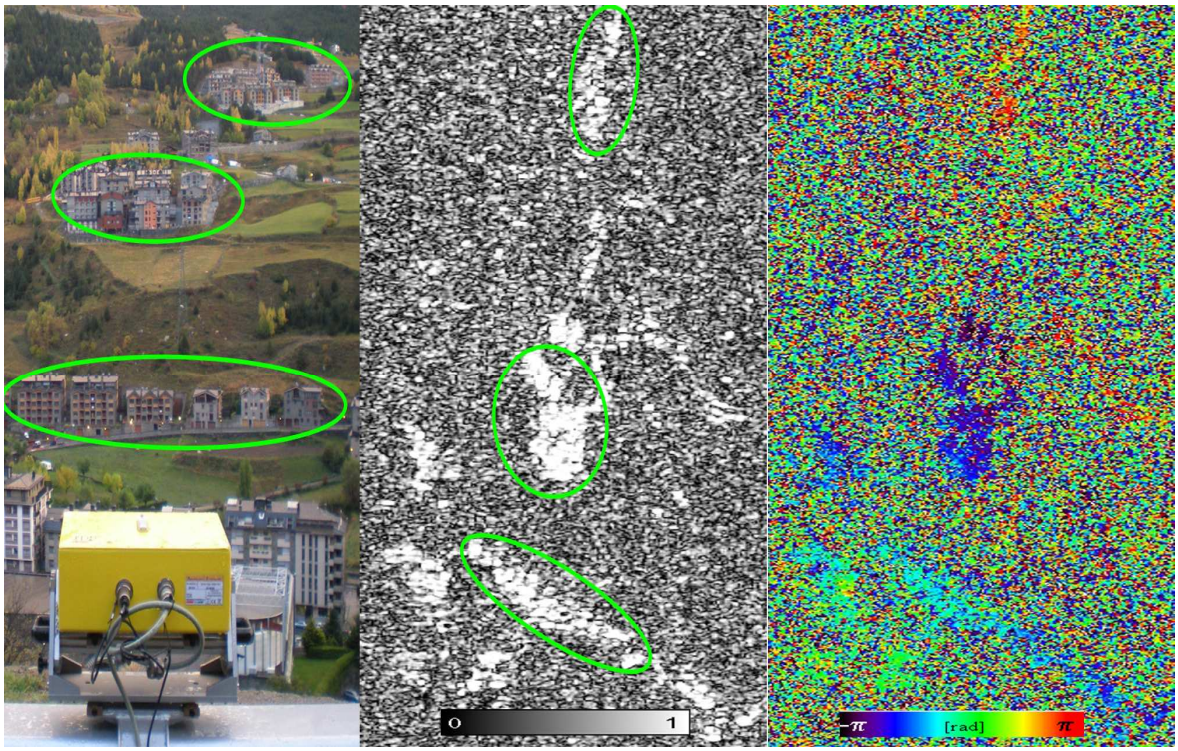

Figure 3.6: Picture of the Canillo test site (left). Coherence of a 35-day interferogram (middle), and the corresponding interferometric wrapped phase (right).

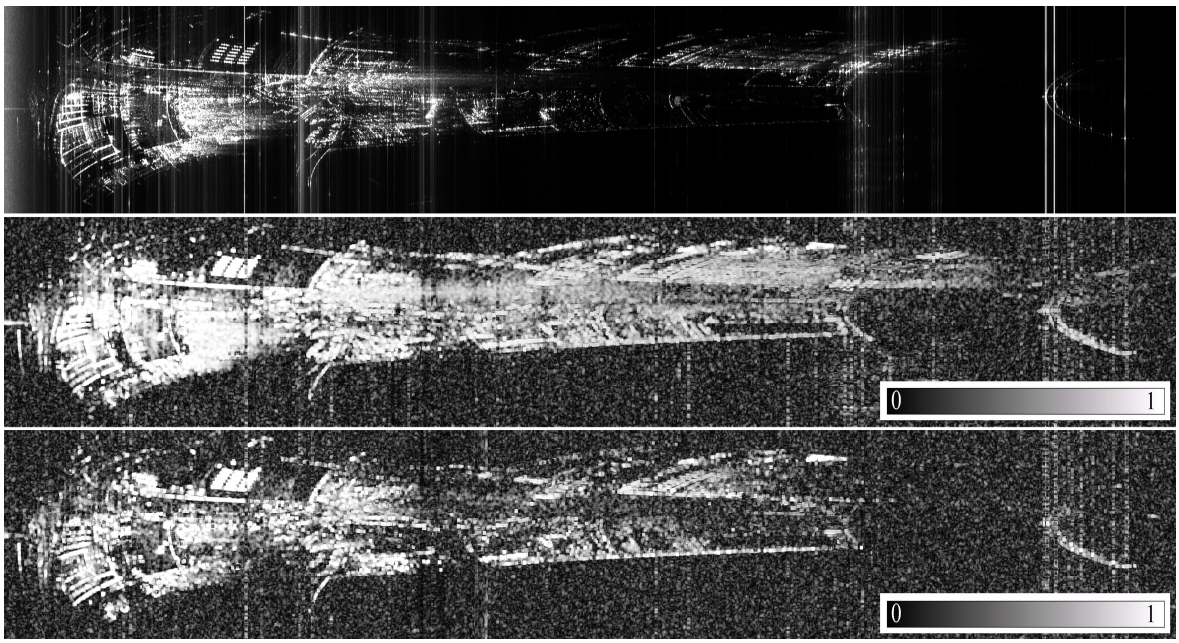

Figure 3.7: GB-SAR amplitude image over the Algeciras harbour (above), coherence of a 10-minutes interferogram (middle), and coherence of a 1-day interferogram (bottom).

To conclude it is important to underline an important limitation of the coherence-based pixel selection. Since the coherence of a given pixel is estimated using an area centred on this pixel, see Equation 2.20, the coherence map is implicitly a low-resolution map, which is not adequate to precisely discriminate coherent features such as points or very thin linear elements. Either these elements are masked out by the surrounding noisy pixels (false negative), or the coherent elements dominate over the neighbouring noisy pixels, making them to appear, wrongly, as coherent (false positive). An example of this latter case is shown in Figure 3.8, where a portion of the dike, which clearly appears as a thin structure in the amplitude image, corresponds to a rather larger coherent area. In this case, the dike is a coherent structure that dominates over the surrounding pixels, which correspond to water. Although these pixels are definitely noisy because water surfaces decorrelate in a matter of seconds, they appear to be coherent and hence could be wrongly selected using a coherence-based pixel selection. Due to this important limitation, in this dissertation, the coherence is usually used to analyse single GB-SAR interferograms, while the second selection criteria (described below) is preferred to process large stacks of multiple interferograms.

3.4.2. Amplitude-based selection

This criterion is based on the analysis of the behaviour of the amplitude of each point along the stack of N images. It cannot be used to select pixels on a single interferogram. This principle was made popular by Ferretti et al. (2001) to select the so-called permanent or persistent scatterers, even though it was already proposed earlier, e.g. see Bamler and Hartl (1998). The key pixel selection parameter is the so-called dispersion of amplitude (DA). Given a set of N complex SAR images, the mean amplitude (MA) of a given pixel (i, j) is calculated:

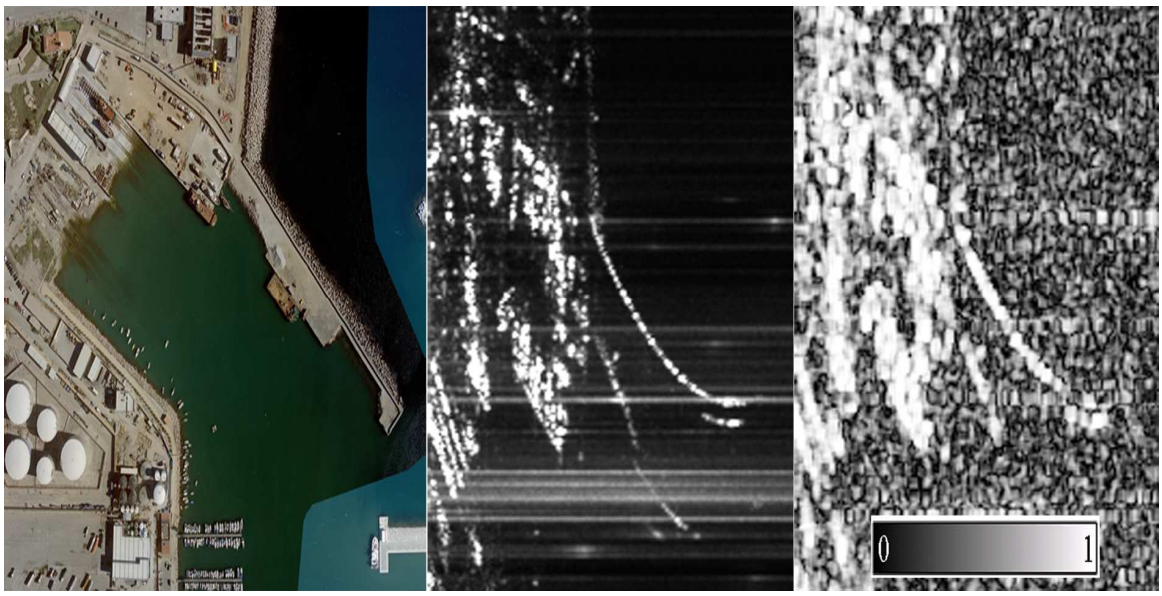

Figure 3.8: Ortho-image of the Algeciras harbour (left) GB-SAR amplitude (middle), and coherence of a 15-min interferogram computed with a window of 3 pixels in azimuth by 5 pixels in range (right).

$$MA(i,j) = \frac{1}{N}\sum_{i=1}^{N} A_i(i,j) \tag{3.7}$$

where A_i is the amplitude of the image i. The mean amplitude is used for visualization purposes and the DA is used for selecting the points. The DA is then calculated as:

$$DA(i,j) = \frac{Stdev\left[A_1(i,j),.....,A_N(i,j)\right]}{MA(i,j)} \tag{3.8}$$

Bamler and Hartl (1998) show that there is a linear relation between the DA and the standard deviation of the phase noise, which holds for small DA values. Even though this criterion was developed for satellite data it is used in the context of this work for ground-based data.

Low DA values indicate "good" pixels, characterized by low phase noise. Again, we face the challenge of fixing a threshold to select the "good" pixels, which require adjusting the trade-off between phase quality and density of the available deformation measurements. In satellite-based PSI, Ferretti et al. (2001) suggest a DA threshold of 0.2 to select the so-called candidate persistent scatterers. However, in the practice, we often face the problem of finding a trade-off between the quality of the selected points and the need of guarantee a sufficient number of samples in the area of interest. This occurs in all those areas characterized by low spatial density of good pixels.

An example of amplitude-based pixel selection, concerning an instable slope in an open pit site, is shown in Figure 3.9. In this example, data acquired over a 5-day monitoring campaign were processed. A set of 50 images were used to calculate the MA and the DA. In this case the pixel selection seems to be, at least qualitatively, appropriate. As for the coherence-based criterion, an empirical way to prove it is to analyse the phase unwrapping results.

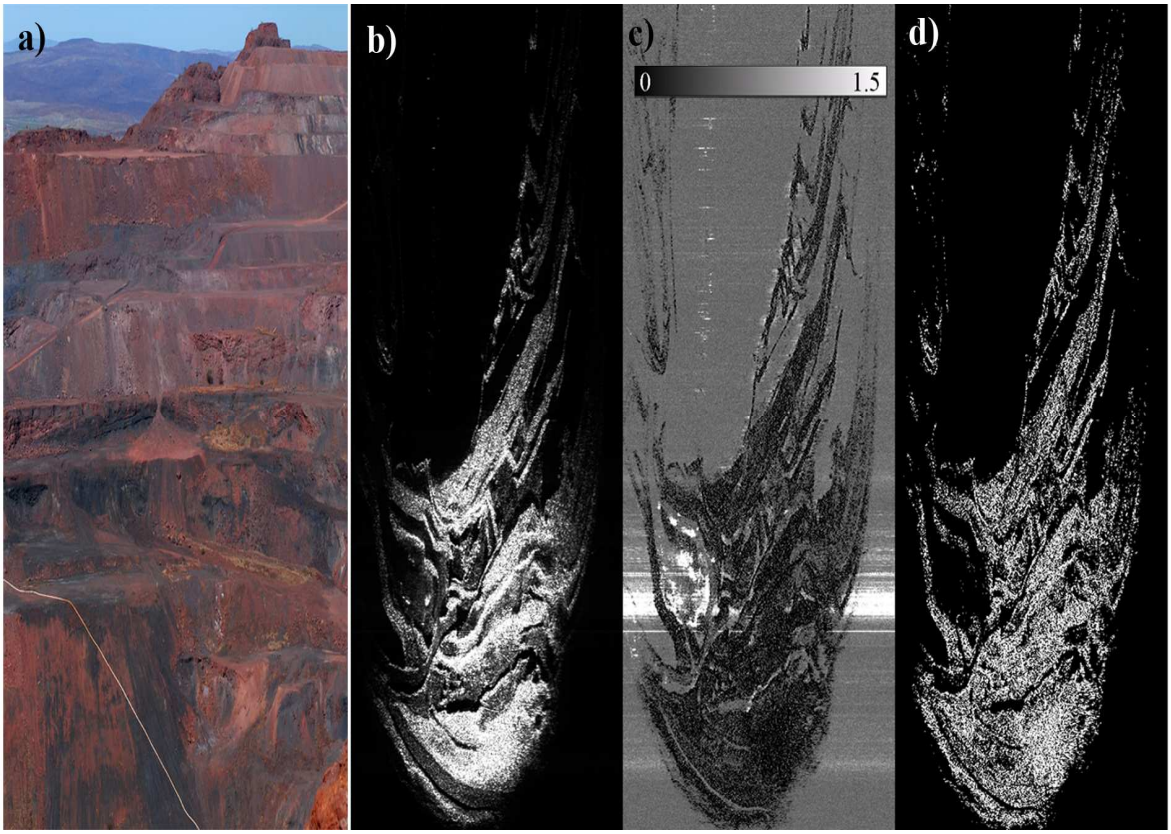

Figure 3.9: GB-SAR data acquired over an open pit for slope instability monitoring. Picture of the site (a), 50-image mean amplitude (b); amplitude dispersion (c); selected pixels with *DA* below 0.25 (d).

An important advantage of this criterion is that it is point-based. Thus, as it is computed considering the data of a single pixel, it does not suffer the limitation of coherence, which is area-based. However, a limitation of this approach, which is particularly evident when large data stacks are analysed, is that it is based on global statistics over the whole data stack. This has two drawbacks. On one hand, pixels that contain valuable interferometric phases, but not during the whole monitoring period, may be discarded: more advanced pixel selection techniques need to be developed to fully take advantage of such pixels. On the other hand, pixels that contain, on average, good interferometric phases, but which are contaminated by a number of anomalous or noisy phases could be selected. Again, more elaborated techniques should be employed to clean the anomalous and noisy data. This will imply getting an insight of data quality within the data stack at hand, and to handle an irregular temporal sampling of the deformation, which may differ from one pixel to another.

3.5. 2D phase unwrapping

In this step, the wrapped interferometric phases of the N-1 generated interferograms are unwrapped, i.e. the unwrapping constant k of Equation 3.1 is estimated. Since this operation is performed interferogram by interferograms, without exploiting time component, it is called 2D phase unwrapping. As mentioned above, an implementation of

the Minimum Cost Flow method (Constantini, 1998; Costantini and Rosen, 1999) is used in this dissertation. It is worth noting that this step is only performed over the points selected in the previous step.

The condition needed to perform a correct phase unwrapping is discussed in Chapter 2, see Equations 2.22 and 2.23. If this condition is not satisfied aliasing or phase unwrapping errors may occur, which can drastically corrupt the quality of the deformation estimates. It is worth noting that many other deformation measurement techniques do not suffer this type of limitation: all aspects related to phase unwrapping errors have to be treated with particular care. Given the importance of phase unwrapping, in this dissertation a whole chapter, Chapter 4, is devoted to describe and illustrate the performances of a new 2+1D phase unwrapping approach.

Three main classes of phase unwrapping errors are described below together with a discussion about its implication from the GB-SAR deformation measurement point of view. The three classes are: "fast deformation", φ_{Noise} component, and atmospheric component.

- **"Fast deformation"**. Fast deformation phenomena cause a very insidious type of unwrapping error. In fact, it occurs in all areas where deformation is more severe, i.e. in the priority areas of any deformation monitoring activity. It is worth emphasising that the expression "fast deformation" in fact applies to the specific technique at hand: it should be said "fast from the interferometric GB-SAR viewpoint". That is to say, a phenomenon can be considered very slow, slow, etc. from the viewpoint of a given application and, at the same time, being a too fast phenomenon to be measured by the technique at hand, i.e. the GB-SAR.

As already discussed in Chapter 2, GB-SAR temporal sampling, i.e. the time interval between image acquisitions, plays a fundamental role in phase unwrapping errors caused by deformation. An example is shown in Figure 3.10, which concerns the Formigal (Pyrenees, Spain) test site. Four unwrapped interferograms, which concern the same deformation phenomenon with an almost constant deformation rate, are shown. The 9.3-day unwrapped interferogram correctly captures the deformation field, which is shown on the top left side of the figure. The 18.7-day interferogram is affected by unwrapping errors in the bottom part of the image and, thus, part of the deformation field is incorrectly measured. The entire deformation area seems to have undergone a recession in the 26.6-day interferogram, i.e. the deformation appears to be more moderate than that observed over 9.3 days. Finally, the deformation pattern is lost almost completely in the 38.5-day interferogram. Thus, assuming a constant deformation rate, in this case, the GB-SAR can be used in discontinuous mode with a revisiting time of approximately 9 days.

Another interesting example of aliasing errors is shown in Figure 3.11, which concerns the Port of Algeciras (Spain). The blue line shows the change of the sea level observed in the GB-SAR LOS caused by tidal effects: the periodical sea level pattern, which in the LOS ranges from 23 to 30 cm, is followed correctly by the GB-SAR data. This was obtained with a temporal sampling of one image every 10 minutes, approximately. The pink line shows the time series of the same point, which however was derived with a reduced temporal sampling, with one image every 100 minutes. In this case the accumulated movement between consecutive images does not satisfy the basic condition of Equations 2.22 and 2.23, and the aliasing errors completely mask the main deformation signal: the deformation estimate is completely erroneous. Again this example shows the importance of properly choosing the right GB-SAR temporal sampling.

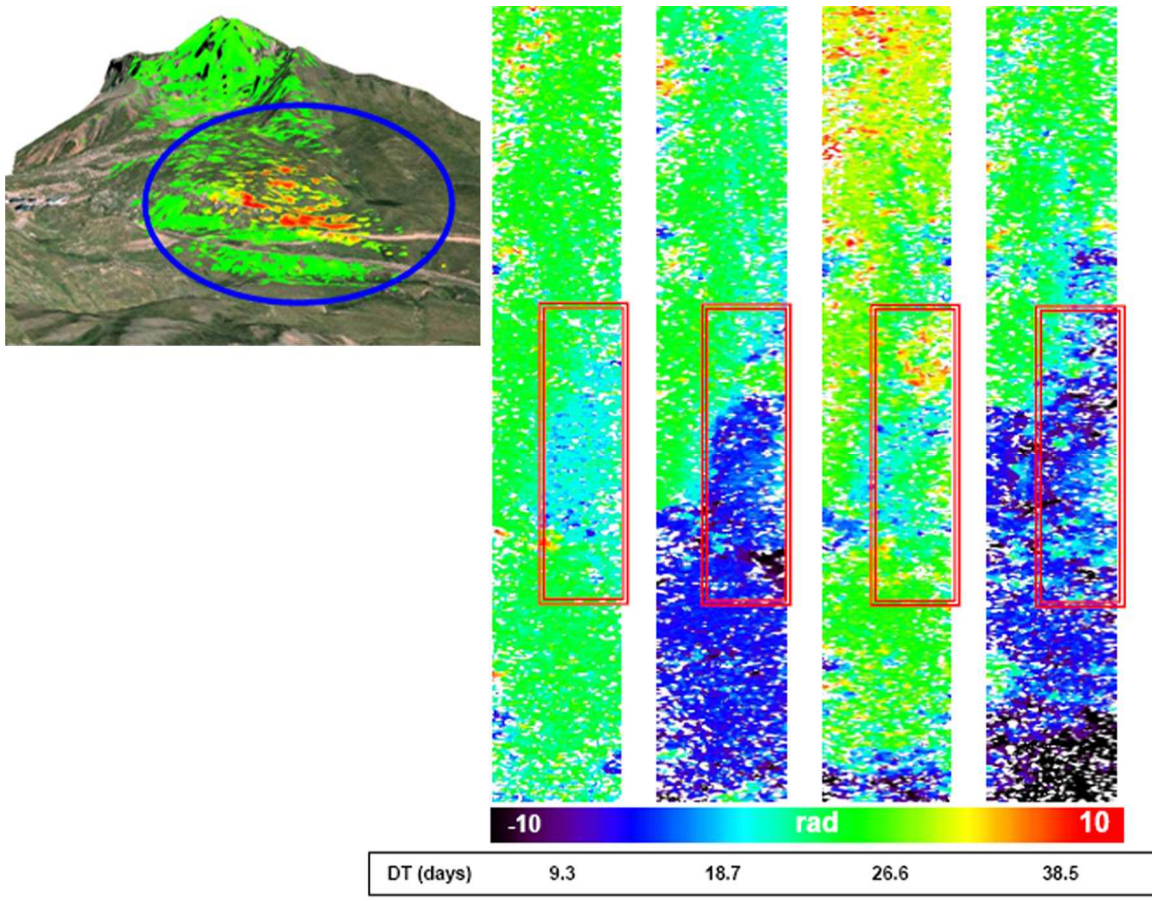

Figure 3.10: Deformation monitoring of the Formigal (Pyrenees, Spain) landslide. The accumulated deformation map is shown in the upper left part of the figure. Four unwrapped interferograms are shown, which correspond to the same deformation phenomenon, which is characterized by a constant deformation rate. The interferograms have different time intervals, which range from 9.3 days to 38.5 days.

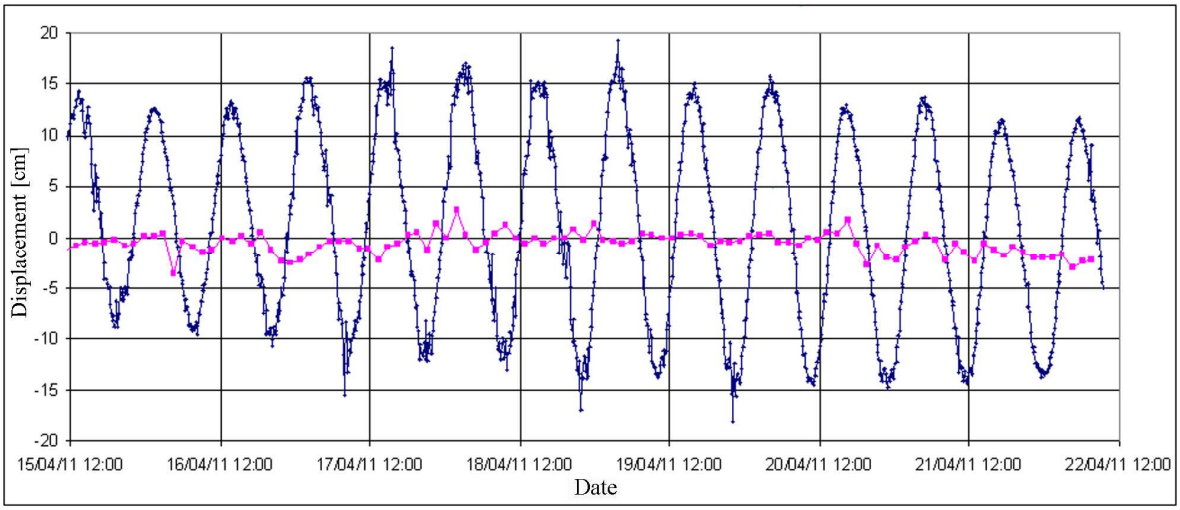

Figure 3.11: Example of aliasing errors from the Port of Algeciras (Spain). Deformation time series which corresponds to the change of the sea level caused by tidal effects. This was observed in the GB-SAR LOS using one image every 10 min (blue line). Time series of the same point observed with a reduced temporal sampling of one image every 100 min (pink line).

- φ_{Noise} **component.** The noise phase component can critically affect the phase unwrapping. This can be avoided by selecting points with low φ_{Noise}, e.g. by choosing high coherence thresholds. However, in some cases, we do not get enough points in the area of interest, and the pixel selection criteria must be relaxed, including noisier points. Figure 3.12c and d show some examples of phase unwrapping errors, highlighted by red circles, which are probably due to φ_{Noise}. These errors can be identified in a relatively easy way because their phase differences with adjacent pixels are multiples of 2π.

- **Atmospheric component**. The combined effect of low pixel density and strong atmospheric effects can produce aliasing errors. For this reason, isolated pixels have to be analysed with particular care. An example is shown in Figure 3.12a and b. This type of aliasing errors differs from the other previous two ones: it can even occur over very coherent and stable areas that are isolated from the rest of pixels, like the one shown in Figure 3.12b.

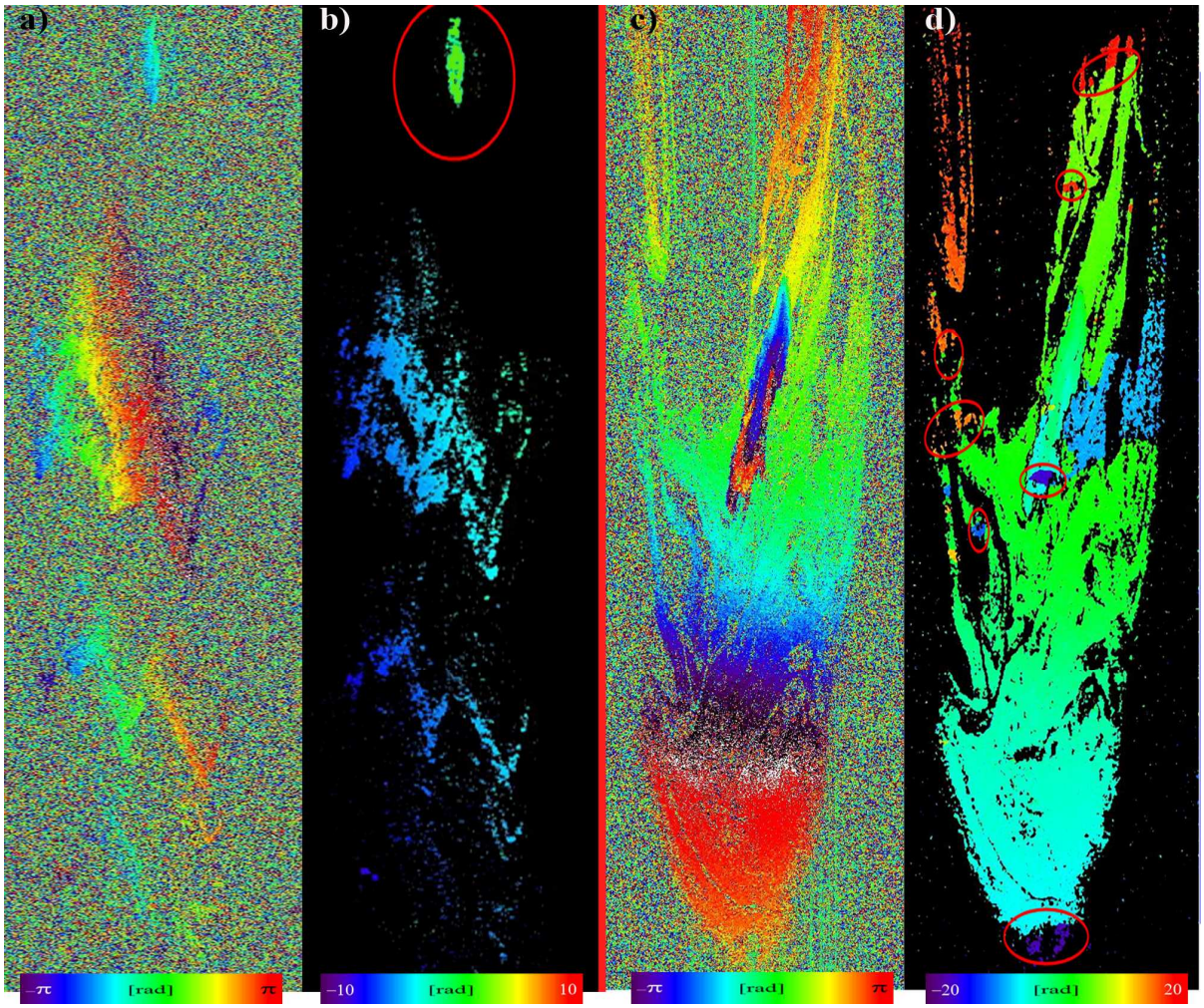

Figure 3.12: Wrapped and unwrapped interferograms from the Montserrat (Barcelona) test site (a, b), and from an open pit mine (c, d). The red circle in (b) shows an aliasing error, which is caused by the combined effect of low pixel density and strong atmospheric effects. The red circles in (d) highlight examples of phase unwrapping errors, which are probably due to φ_{Noise}.

3.6. Direct phase integration

In this step are estimated the interferometric phases in correspondence to each acquired image, starting from the set of unwrapped interferometric phases. This is done by assuming the phase values of the first image equal to zero. The results are N phases that contain the accumulated phase increment $\tilde{\varphi}_i$ with respect to the first one, i.e.:

$$\tilde{\varphi}_i = (\varphi_{Geom} + \varphi_{Defo} + \varphi_{Atmo} + \varphi_{Noise})_i - (\varphi_{Atmo})_{ori} \tag{3.9}$$

where φ_{Geom} is the phase term due to instrument repositioning errors between the first image acquisition and the i^{th} acquisition, φ_{Defo} is the deformation phase component related to the deformation occurred between the 1st acquisition and the i^{th} acquisition, φ_{Atmo} is the atmospheric phase contribution corresponding to the i^{th} image, φ_{Noise} is the phase noise term of the i^{th} image, and finally $(\varphi_{\text{Atmo}})_{\text{ori}}$ is the atmospheric phase contribution of the 1st image. The phase estimation is performed for each selected point and for the N acquired images. In order to do so, the phase integration works point wise and in the "temporal dimension". In the chain here described this estimation can be performed in two different ways: by direct integration or by using the so-called Interferogram to Image (int2ima) algorithm discussed in detail in Chapter 4.

It is worth noting that the direct integration is the simplest way to reconstruct the N phases, which are obtained by integrating the N-1 interferograms formed by consecutive images. With such an integration the simplest network is needed, which requires the minimum set of interferograms to connect all the images. Figure 3.13 shows the difference between the network used in the direct integration and the redundant one required by the int2ima algorithm. The direct integration requires a lower computational effort but it does not allow checking the quality of the observations: it is a zero redundant system where error propagation, especially the one due to 2D-phase unwrapping errors, cannot be controlled. Despite this limitation, the direct integration is a useful tool, which can be used at least in not problematic cases, e.g. with good phase quality, smooth deformation evolution, etc.

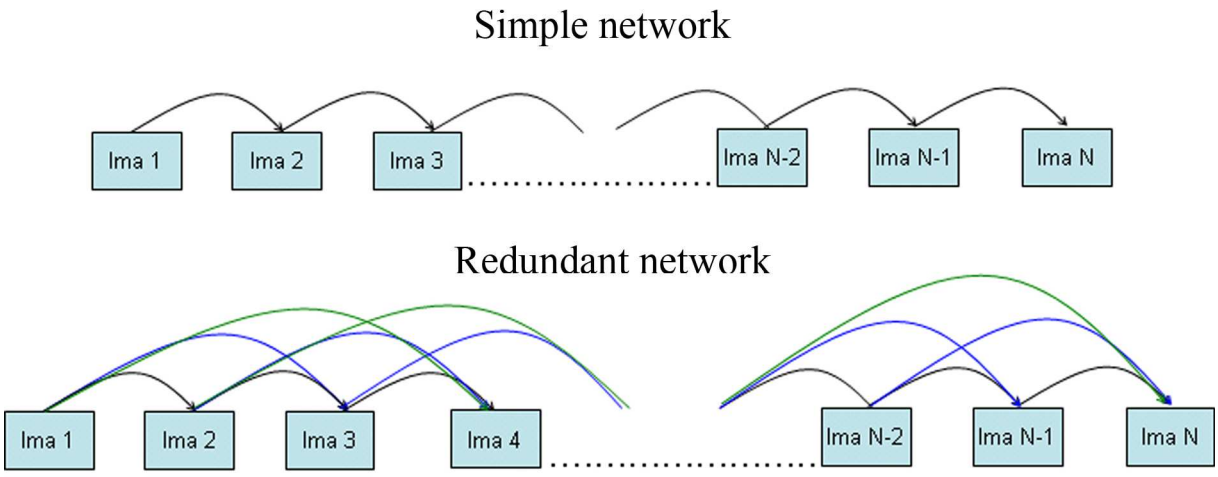

Figure 3.13: Comparison of the network of images and interferograms used in two integration approaches: the direct integration network and the int2ima network. The former one uses the simple network with a minimum configuration, while the latter one is a redundant network, which is useful to detect and correct for phase unwrapping errors.

3.6.1. Direct integration algorithm

Let's consider N-1 unwrapped interferograms, which form the "simple network" shown in Figure 3.13:

$$\Delta\varphi_i = (\varphi_{Defo} + \varphi_{Atmo} + \varphi_{Noise} + \varphi_{Geom})_i - (\varphi_{Defo} + \varphi_{Atmo} + \varphi_{Noise} + \varphi_{Geom})_{i-1} \tag{3.10}$$

The algorithm involves the following steps:

1. Selecting a reference point, usually located in a stable area. A set of points can be chosen instead of a single point. The selected point or points have to be part of the pixel set selected in the pixel selection step.
2. Referencing all the N-1 interferograms to the reference point(s):

$$\Delta\varphi_i(i,j) = \Delta\varphi_i(i,j)_{ori} - \Delta\varphi_i(i_{refe}, j_{refe})_{ori} \tag{3.11}$$

   where $\Delta\varphi_i(i_{\text{refe}}, j_{\text{refe}})_{\text{ori}}$ is the original phase of the reference point of the i^{th} interferogram, and $\Delta\varphi_i(i, j)_{\text{ori}}$ is the original phase of a given pixel (i, j). If a set of reference points is chosen, the last term of the equation is the mean phase computed over the reference points.

3. Integrating the phases over time:

$$\left.\begin{aligned} \tilde{\varphi}_0(i,j) &= 0 \\ \tilde{\varphi}_i(i,j) &= \tilde{\varphi}_{i-1}(i,j) + \Delta\varphi_i(i,j) \end{aligned}\right\} \tag{3.12}$$

   where the $\tilde{\varphi}_i$ (i, j) is the accumulated phase of the image i^{th} with respect to the first one, $\tilde{\varphi}_0$.

The final result of the direct integration is, for each selected pixel (i, j), the temporal evolution of the phase during the acquisition period. The integration is performed for each selected pixel. The unwrapping errors arising from the 2D phase unwrapping stage can be propagated along the whole estimated time series. This is an important drawback of using a simple network, which does not provide any redundant observation. In order to improve the results, a step detector can be added to the above algorithm, which basically exploits the fact that the unwrapping errors are multiples of 2π. This can be accomplished, for instance, by checking the phase differences between consecutive images: if it is greater than a given threshold, the "jump" is corrected by adding or subtracting the correspondent multiple of 2π:

$$\begin{aligned} &if\ (\left|\tilde{\varphi}_i(i,j) - \tilde{\varphi}_{i-1}(i,j)\right| > 2\pi - \varepsilon)\ \Rightarrow \\ &\Rightarrow\ \tilde{\varphi}_{i\_new}(i,j) = \tilde{\varphi}_i(i,j) - \left[\frac{\tilde{\varphi}_i(i,j) - \tilde{\varphi}_{i-1}(i,j) + \pi}{2\pi}\right] \cdot 2\pi \end{aligned} \tag{3.13}$$

where $[\cdot]$ indicates the integer part and ε is the given tolerance. To the author experience, the tolerance must be not higher than 0.6 radians. In some cases, bigger tolerance values could provide false corrections, which can hardly be detected later by a simple quality check. A simple step detector like the one from Equation 3.13 is sometimes sufficient to detect and correct for aliasing errors. However, as it is discussed extensively in Chapter 4, a more complex strategy is often needed to properly detect and correct the aliasing errors.

3.7. Estimation of the phase atmospheric component

The atmospheric phase component is mainly caused by changes in the basic properties of the atmosphere that interferes with the GB-SAR signal during different image acquisitions, e.g. see Iannini et al. (2009), Luzi et al. (2004) and Noferini et al. (2005b). This component, which is often called Atmospheric Phase Screen (APS), mainly affects the sensor to target distance, i.e. it mainly varies with the distance from the GB-SAR, but can also affect in a different way targets in the cross-range direction. In general its effect is strongly correlated spatially, i.e. it varies smoothly in space. In this step of the procedure we estimate and remove the atmospheric component $(\varphi_{\text{Atmo}})_{\text{i}}$ - $(\varphi_{\text{Atmo}})_{\text{ori}}$ shown in Equation 3.9. However, at the same time we may estimate other systematic effects that have similar spatial characteristics, like the φ_{Geom} phase term due to instrument repositioning errors. In order to simplify the notation, from now on we consider that the φ_{Atmo} term includes both the APS and the φ_{Geom} phase term.

Several authors have studied the APS estimation for GB-SAR data, proposing different algorithms. In Noferini et al. (2005a) the APS is modelled as a quadratic function of the distance, and it is estimated by using just two Ground Control Points (GCPs). A similar approach is used by other authors by slightly changing the model, e.g. from quadratic to linear, or by varying the number of GCPS, e.g. see Pipia et al. (2006). These approaches are easy to implement and, considering that they do not require extra data, quite effective. However, in these methods, the APS estimation is performed on unwrapped data, which are assumed to be aliasing-free, and, more importantly, they are only modelling the APS changes as a function of the distance. From the author experience, this is not sufficient because, even though the APS is mainly a function of the distance, it can also affect in a different way the targets along the cross-range direction. Furthermore, if we want to include the errors due to the repositioning, we need to properly model these effects in the azimuth or cross-range direction. A different approach is presented in Iannini and Monti Guarnieri (2009). In this case, the authors propose a method based on in situ acquired meteorological data and an initial calibration of the humidity function. The method has one main advantage with respect to previous approaches: it is not affected by unwrapping errors, because the APS is estimated using the acquired meteorological data and it is directly removed from the wrapped interferogram. According to its authors this method shows good performances. However, it is less accurate than the method commented above and it is not reliable in situations where strong changes in the atmospheric parameters along the scene occur.

3.7.1. APS estimation proposed algorithm

In our procedure a least squares (LS) estimation method is proposed. Its main assumption is that the APS is strongly correlated spatially. Examples of APS smoothly varying in space are shown in the first column of Figure 3.14. The model used for the APS component is a 2D-polynomial of variable degree g:

$$\varphi(\mathrm{i},\mathrm{j}) = a_{00} + \sum_{r=0}^{g} a_{r,(g-r)} * (i - i_0)^r * (j - j_0)^{g-r} \tag{3.14}$$

where (i, j) are the pixel coordinates of a given pixel, φ is the phase that includes both APS and the φ_{Geom} phase term, a_i are the polynomial parameters, (i_0, j_0) are the coordinates of the reference point. The observations to estimate the above model

parameters are pixels which are located in stable areas, which have to be known a priori. For such pixels φ_{Defo} can be assumed to be nought:

$$\varphi(\text{i, j}) = (\cancel{\varphi_{defo}(\text{i, j})} + \varphi_{\text{atmo}}(\text{i, j}) + \varphi_{\text{noise}}(\text{i, j})) \tag{3.15}$$

The proposed algorithm involves the following steps.

1. Identification of stable areas using a priori available information. The ideal situation is provided by a scenario with stable areas entirely surrounding the movement area at hand.
2. Estimation of the APS over the selected stable areas using Equation 3.14. The estimation is done by LS adjustment with outlier rejection. The estimated APS and φ_{Geom} phase term are given by:

$$\varphi(\text{i, j}) = a_{00} + \sum_{r=0}^{g} \tilde{a}_{r,(g-r)} * (i - i_0)^r * (j - j_0)^{g-r} \tag{3.16}$$

   where $\tilde{a}_i$ are the estimated parameters, (i, j) are the image coordinates of the selected points and (i_0, j_0) are the pixel coordinates of the reference point.
3. Finally, Equation 3.16 is used to estimate (predict) the APS and φ_{Geom} phase term over the non stable areas. This term is then subtracted from the original phases to obtain phases cleaned by APS and φ_{Geom} for the whole set of selected points.

The main output of the APS estimation is a stack of N phases sorted out by time. Each pixel of the estimated phases contains the APS-free accumulated phase with respect to the first acquisition.

Some examples of results of the procedure are shown in Figure 3.14, which concerns the monitoring of an open pit mine. The deformation area is highlighted by a red circle. The phase fringes in the first column are mainly caused by atmospheric artefacts. A slight azimuth term is visible in the second interferogram (a.2). The second column shows the wrapped interferograms, which are cleaned by the APS and φ_{Geom} phase term: the main phase fringes were globally removed. However, some residual fringes remain, which are mainly caused by local APS artefacts which are not modelled by our approach, e.g. see the red artefact on the bottom part of the movement area in b.5. Further research is needed to correctly model and remove such local APS effects.

The quality of the estimated APS component depends on different factors: the distribution of the stable areas with respect to the area of interest, the phase quality over these areas, and the accuracy of the chosen model, which mainly depends on the complexity of the observed scene, and in particular on its topography. A scheme of the distribution of stable vs. area of interest is illustrated in Figure 3.15. The best configuration is given by the stable areas that completely surround the area of interest. When the optimal configuration cannot be used, particular care should be taken to predict the APS over the area of interest and to interpret the results. Figure 3.16 illustrates a case where, due to the particular topography of the area, the APS effects may be strongly correlated with the expected deformation phenomenon. The figure shows a deformation map derived from a pair of images with 2 months of time separation. The measured object of interest is a landslide affecting most of the urban area. Unfortunately, the unavailability of a stable area around the area of interest makes impossible to discriminate between deformation and APS. In this specific case and for the above reason it was not possible to obtain reliable deformation estimation.

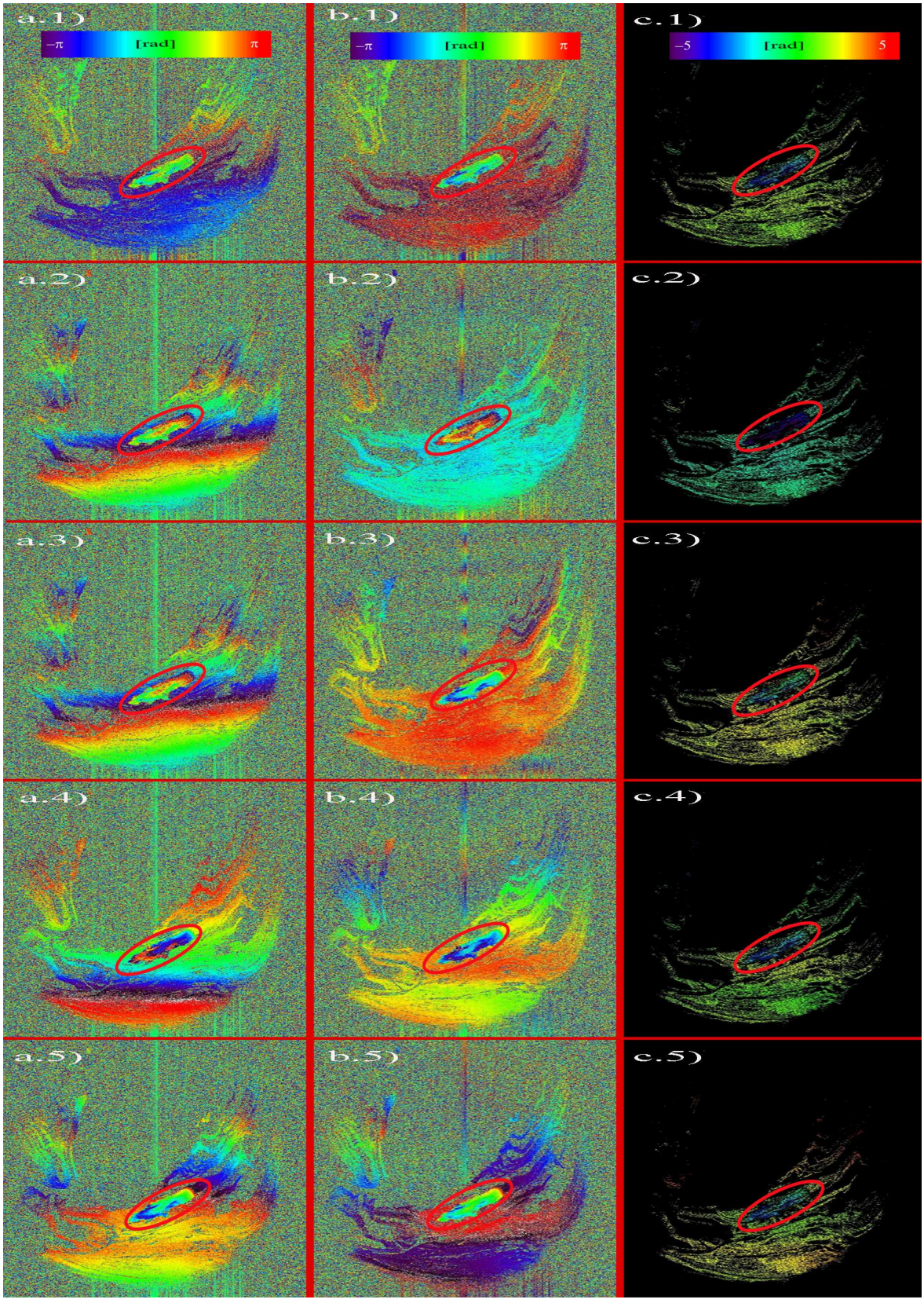

Figure 3.14: Interferograms from the same area shown in Figure 3.9. Original wrapped interferograms (left), APS-cleaned wrapped interferograms (middle), and APS-cleaned unwrapped interferograms (right).

Figure 3.15: Distribution of stable areas with respect to the area of interest. The best configuration is where the stable area completely surrounds the area of interest (left).

3.8. Displacement computation and geocoding

The generation of the geocoded deformation maps and time series is discussed in this section. This step of the process is fundamental for GB-SAR data interpretation and exploitation. This operation involves a transformation from the image space, where each pixel is identified by its position in the image (column and line), to the object space, by assigning 2D map projection coordinates or geographic coordinates and height. This operation is also called 3D geocoding or geo-referencing. The outputs of this step are:

- A 3D position vector on a given reference system, typically cartographic coordinates (E, N) plus orthometric heights (H) or geographic coordinates (ϕ, λ) plus an ellipsoidal height (h), is obtained for each processed pixel of the master SAR image.
- The estimated deformation parameters, i.e. the time series and other parameters, like the accumulated deformation, etc., are obtained for each 3D location.

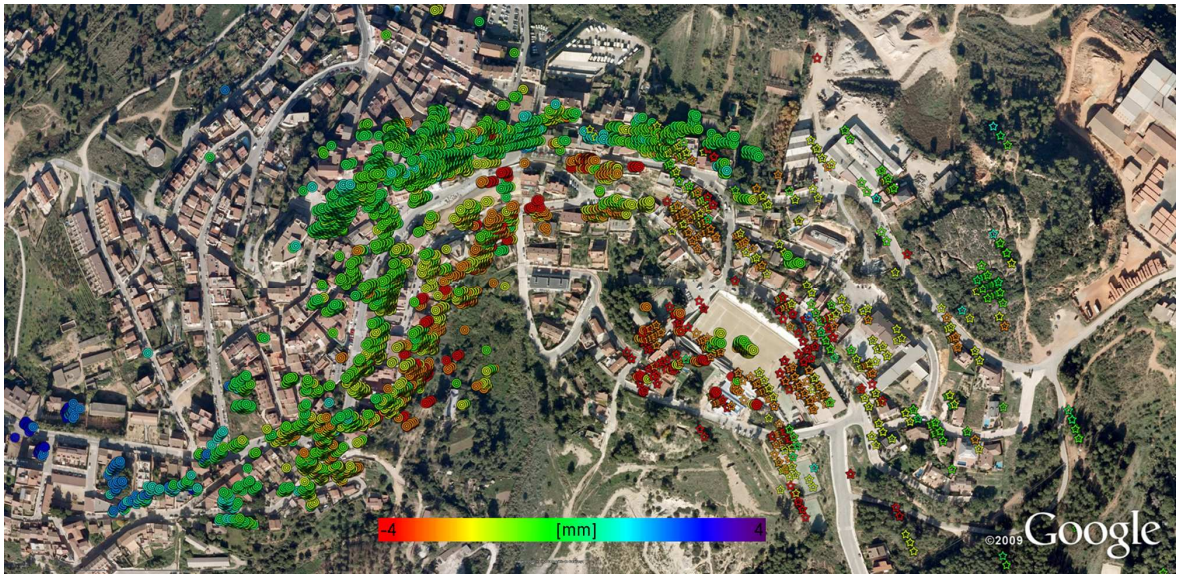

Figure 3.16: Deformation map on the Papiol (Barcelona) site, characterized by a weak APS estimation: there are no stable areas properly distributed around the deformation area. This map may contain an APS contribution with a pattern that is strongly correlated with the potential deformation pattern: it was not possible to separate the APS from the deformation.

A rigorous 3D geocoding requires knowledge of the corresponding sensor model, which describes how the image and object spaces are connected according to the geometric and physical properties of the sensor. In addition, it requires the determination of the sensor parameters that characterize the specific geometric and physical properties of the acquisition of the image. The sensor model used with GB-SAR data, which connects a given pixel to its corresponding geocoded point P, is given by:

$$\left.\begin{aligned} r &= \sqrt{(E-e_0)^2+(N-n_0)^2+(Z-z_0)^2} \\ \theta &= \arctan\left(\frac{E-e_0}{N-n_0}\right) \end{aligned}\right\} \tag{3.17}$$

where (e_0, n_0, z_0) are the three coordinates of the centre of the GB-SAR in a given reference system of the object space, (E, N, Z) are the coordinates of the geocoded point P in the same reference system of (e_0, n_0, z_0), r is the slant range distance, and θ is the azimuth of the geocoded point P. The first equation is named radar range equation, while the second one is the azimuth or cross-range equation. The GB-SAR 3D geocoding needs a third equation, which is given by the surface $Z=S(E, N)$, which is based on an external DEM or DSM of the observed scene. The sensor parameters are given by the GB-SAR position (e_0, n_0, z_0), and the azimuth of the antenna pointing direction θ_0, which is described in the following section.

3.8.1. Geocoding algorithm

Before starting the 3D geocoding the interferometric phases coming from the previous processing steps are transformed in displacements or deformations. For each pixel and for each phase the following equation is used:

$$\Delta R_{LOSi} = \frac{\lambda \cdot \varphi_i}{4\pi} \tag{3.18}$$

where $\Delta R_{\mathrm{LOS}i}$ is the accumulated displacement in the LOS of the *i-th* image, λ is the wavelength, φ_i is the *i-th* estimated phase and the factor 4 is due to the two way radar-object-radar of the received signal.

The next step is the 3D geocoding. In this procedure is used the so-called inverse geocoding, which computes the corresponding image coordinates starting from the object coordinates of a point on the observed surface provided by a DEM or DSM of the scene. Given a DEM or DSM $Z=S(E, N)$ and the sensor parameters (e_0, n_0, z_0) and θ_0, the geocoding algorithm involves the following steps:

1. For each P of the DEM or DSM compute r and θ by using the Equation 3.17.
2. Finding the corresponding image coordinates:

$$\left.\begin{aligned} line &= \frac{r}{\Delta R} \\ column &= column_{central} + \frac{\theta-\theta_0}{\Delta\theta} \end{aligned}\right\} \tag{3.19}$$

where ΔR is the GB-SAR sampling step in range, $column_{\mathrm{central}}$ is the central column of the GB-SAR image, $\Delta\theta$ is the GB-SAR constant angular sampling step in cross-range.

By repeating the steps 1 and 2 for all the points of the DEM or DSM we get the object to image space transformation for the whole scene. To run the geocoding, which involves an image to object transformation, an interpolation is needed to find the object space coordinates corresponding to the centre of each image pixel.

The DEM or DSM quality is fundamental to correctly geocode and interpret the data. It is recommended to use a DEM or a DSM, if available, instead a simple DTM. As described in Chapter 2, a DEM generated using a GB-SAR could be used. In this case the DEM should be generated from the same position of the GB-SAR used for the deformation measurements. Figure 3.17 shows an example of geocoded GB-SAR data acquired over the Nativity Façade of the Sagrada Familia (Barcelona). The data were geocoded using a DSM generated by TLS. In this example, the geocoded points are colour-coded according to their height. The results indicate an adequate 3D positioning of the GB-SAR data on the building.

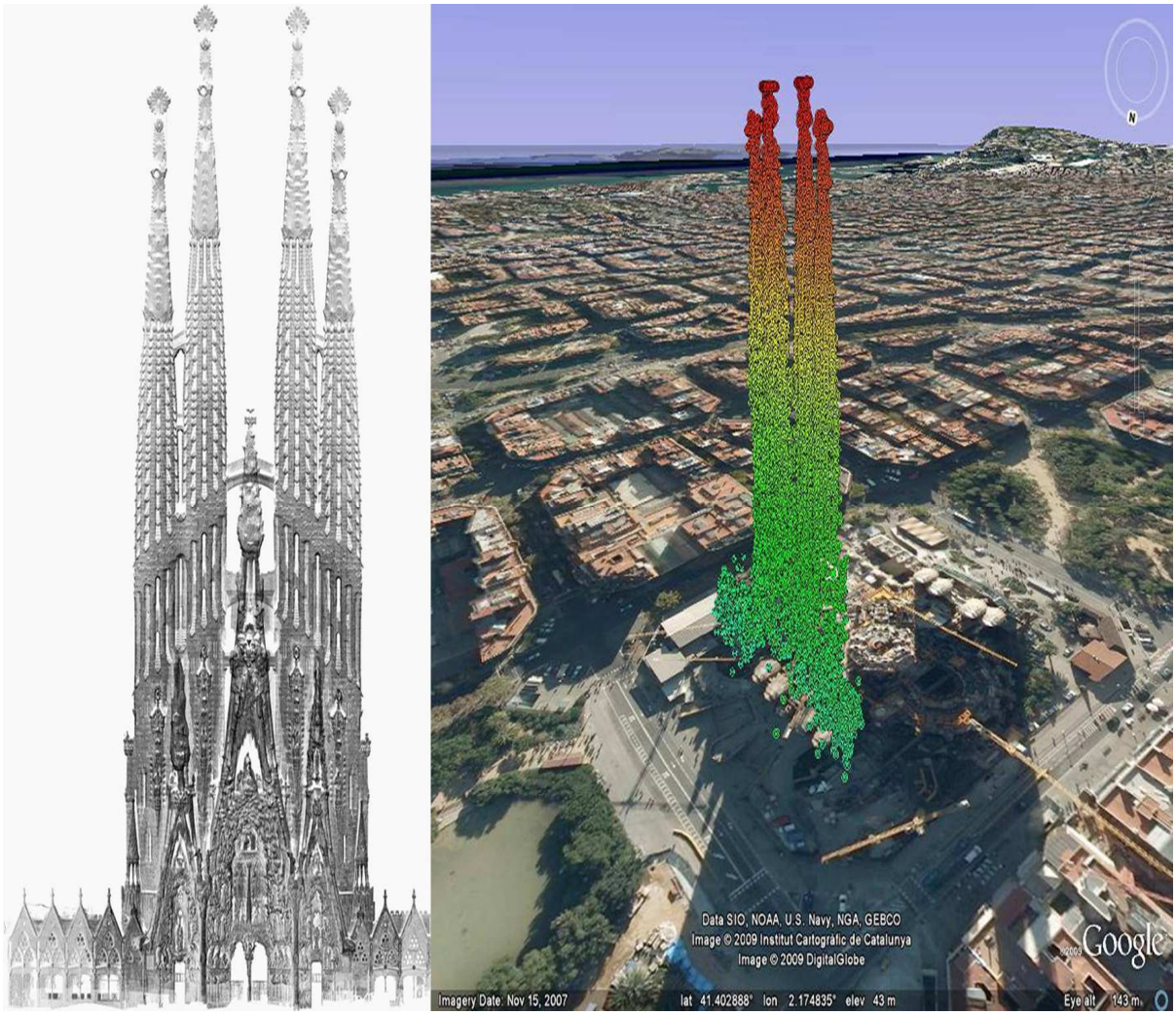

Figure 3.17: Example of GB-SAR geocoding over the Nativity Façade of the Sagrada Familia (Barcelona) based on a DSM generated by TLS. TLS amplitude image (left). GB-SAR geocoded data, with colour-coded heights. DSM provided by "Laboratori de modelitzacio virtual de la ciutat" (LMVC-UPC)

3.9. Precision and accuracy of deformation measurements

The precision and accuracy of any deformation measurement technique are key characteristics that influence its applicability and acceptability. This section describes a serie of experiments carried out to characterize the performances of the GB-SAR deformation measurement. The results shown in this section were obtained from data acquired by the IBIS-L GB-SAR system manufactured by IDS Ingegneria dei Sistemi SpA.

Precision refers to the dispersion of the estimates of a given parameter. A typical measure of the dispersion is the variance. The precision of deformation estimates can be evaluated from the precision of the original observations (i.e. the interferometric phases), typically using variance propagation, or other numerical methods for error propagation. Section 3.9.1 discusses some aspects of the GB-SAR precision based on experimental results. Accuracy is the extent to which the mean of the population of the estimates approaches the true value of the parameter. It can be defined as the closeness to the true. The accuracy of a given estimate cannot be assessed by simple error propagation and requires a validation based on independent data characterized by higher quality. A validation experiment performed to assess the accuracy of the GB-SAR instrument is described in Section 3.9.2. Finally, reliability refers to the robustness of a given technique against not modelled errors in the observations (outliers, blunders, etc.). In GB-SAR, the most important type of not modelled error is given by the phase unwrapping errors, which despite the high precision of deformation measurements affect its reliability.

An experiment devoted to measure the sensitivity to small displacements of the instrumentation used was carried out. The experiment employed the radar of the IBIS-L GB-SAR but in the Real Aperture Radar (RAR) mode. In this mode, the radar acquires data without using the rail and, thus, it has no imaging capability (this mode only provides 1D measurement), but it can measure with a high temporal sampling, which in the experiment was 100 Hz. The object of interest was the building shown in Figure 3.18.

Figure 3.18: Scenario of the sensitivity experiment based on a Real Aperture Radar.

Besides the building, the scene includes a streetlight indicated by a blue circle in the same figure. Using the RAR a displacement time series over an observation period of several minutes was derived, which includes approximately 100 displacement estimates per second. Figure 3.19 shows a portion of the estimated deformation time series over three different points located on the building. These points, which are characterized by high SNR, basically show the same oscillation pattern. The blue one (Rbin77) is clearly noisier, because it has a slightly lower SNR than the other two ones. The most relevant result is that oscillations with amplitudes as small as 2-3 µm are observed. Figure 3.20 shows a time series of a point located on the streetlight. Despite its relatively low SNR, the time series show a periodical pattern of displacements: these are oscillations with amplitudes between 400-500 µm: this is clearly a different oscillation regime than the one shown in Figure 3.19. The results shown in Figures 3.19 and 3.20 are particularly interesting: very seldom in geomatics one can meet such displacement time series. Different analyses were performed to confirm these results, which are promising to measure the natural oscillations of buildings. Luzi et al. (2011) analyse this application, by assessing the potentialities of this technique for monitoring the health state of buildings.

In the context of this dissertation, the above experiment demonstrates the high sensitivity of the IBIS-L sensor to very small displacements (up to a few micrometers). This is, in terms of sensitivity, an upper limit which concerns extremely short term interferometric measurements (where the time separation Δt is 0.01 sec), a close range scenario (between 9 and 35 m, approximately) and targets characterized by high SNR. In addition, it concerns a RAR experiment: for this reasons, its results cannot be straightforwardly applied to the GB-SAR, as it is briefly explained in the next section. However, it surely indicates the great potential of RAR and GB-SAR to measure small displacements.

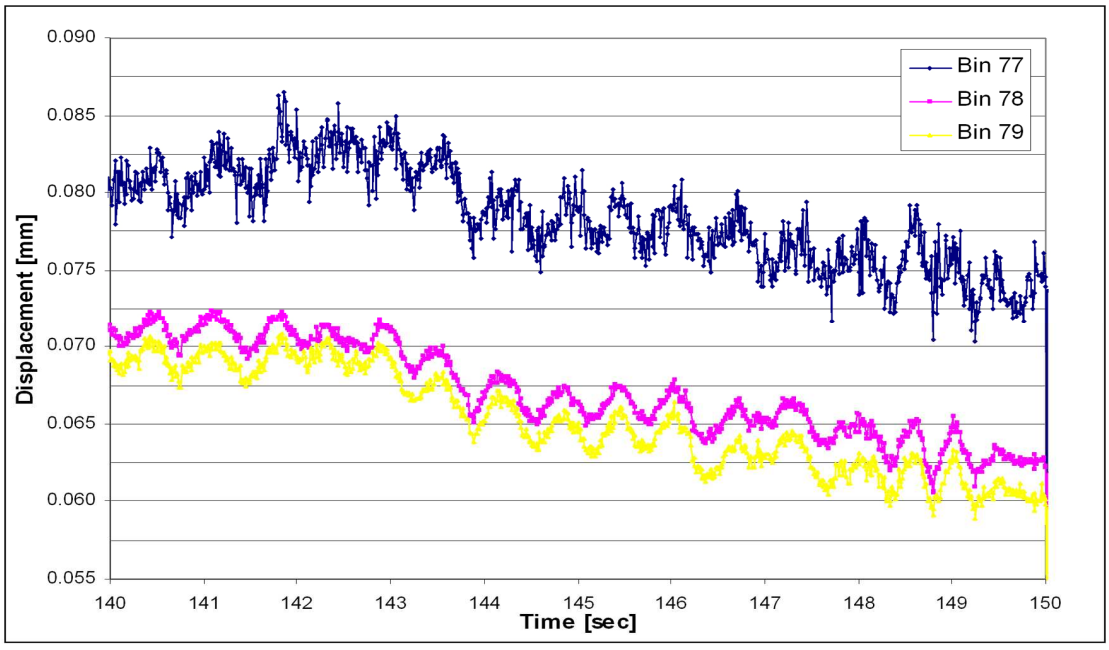

Figure 3.19: Displacement time series obtained from 10 seconds of RAR measurements over three different points located on the building shown in Figure 3.18. These points have oscillations with amplitudes up to 3µm.

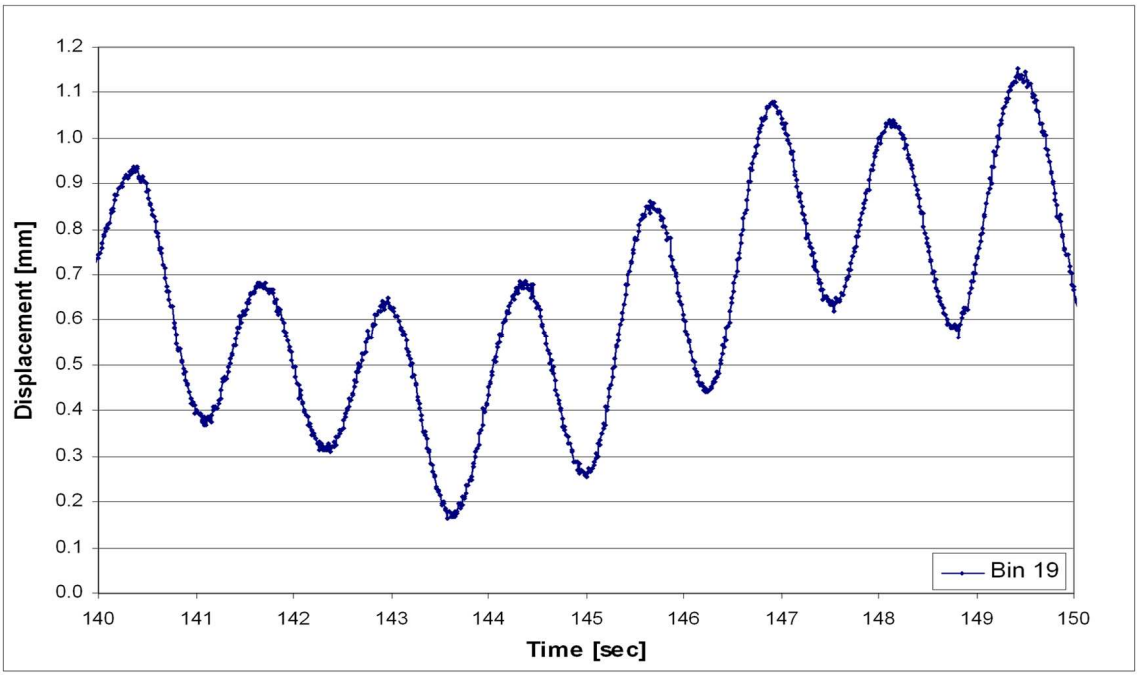

Figure 3.20: Displacement time series obtained from 10 seconds of RAR measurements of a target located on the streetlight (see blue circle in Figure 3.18). The measurement shows larger oscillations than those of the Figure 3.19, with amplitudes of about 0.3 mm.

3.9.1. Analysis of the precision

The precision of the GB-SAR interferometric phase, whose components are shown in Equation 3.1, is analysed in this section. In this context, the phase components φ_{Noise} and φ_{Atmo} are the most important from the point of view of error budget.

The φ_{Noise} includes the sum of different components, like the internal noise of the system, the temporal decorrelation, the effects of image coregistration errors, etc. The most relevant components are mentioned below, without aiming at providing a comprehensive description of all possible error sources. An interesting study of the noise of a GB-SAR system was performed within Galahad, "Advanced Remote Monitoring Techniques for Glaciers, Avalanches and Landslides Hazard Mitigation", a project of the 6$^{\text{th}}$ Framework Programme, see www.galahad.eu. The study focused on the main error sources of the interferometric phase, which were classified in short-term, mid-term and long-term error sources. The magnitude of each type of error was assessed by using both theoretical considerations and experimental results. Table 3.1 summarizes the contribution of the short-term instrumental errors in the LOS displacements. These results were published in 2005 and refer to the Galahad Ku-band GB-SAR prototype.

The IBIS-L GB-SAR instrument is surely better from the instrumental viewpoint than the Galahad prototype. Its performances in the RAR mode (with quasi-instantaneous measurements, $\Delta t = 0.01$ sec) are described in the previous section, see Figures 3.19.and 3.20 It is worth emphasising that even using comparable measurement conditions, especially close measurement distances of tens of metres and high SNR targets, the GB-SAR performances in terms of displacement sensitivity are notably poorer than the RAR ones. On one hand, the GB-SAR has the advantage of using multiple RAR acquisitions of

Cause of short term error	Contribution to the interferometric measurement standard deviation (mm)
Thermal noise	*0.0150*
Demodulator unbalancing I/Q	*0.0265*
Stable Local Oscillator instability	*0.0067*
Spurious	*0.1700*
Total	***0.2182***

Table 3.1: Estimation of the contribution of the short-term instrumental errors in the LOS displacements of a GB-SAR system, from Galahad, D2-2 (2008).

the same scene. In fact, the GB-SAR phase is the result of averaging hundreds of RAR acquisitions. On the other hand, these acquisitions are taken under slightly different atmospheric conditions affecting the sensitivity of the GB-SAR phase.

An example of atmospheric effects on the RAR measurements is shown in Figure 3.19. The measurements are affected by a trend which accumulates 10 μm within the 10 seconds period displayed. This is due to micro-changes in atmosphere in the 30 m distance between sensor and target. However, their effect is three times bigger than the amplitude of the observed oscillations. Figure 3.21 shows the displacement time series of Rbin78 shown in Figure 3.19, but covering a time lapse of more than 4.5 minutes. In this case, the integrated global trend caused by atmospheric effects is of about 135 μm. It is worth noting that the trend is globally increasing over the observed period of time; over much longer periods the atmospheric effects result in zero-mean fluctuations. This is, if two consecutive GB-SAR acquisitions are taken in exactly the same conditions of the 4.5-min RAR data shown in Figure 3.21 (2 GB-SAR acquisitions lasting 2.25 minutes each) and if the sensor and the instrument are static over the 4.5 minutes period (over such periods the average building and GB-SAR oscillations are basically zero), zero displacements would be observed. Unfortunately, a displacement between the two acquisitions of about 58 μm will be measured, which is the difference between the average displacements displayed in Figure 3.21 in the first and second half of the plot (38 vs. 96 μm, respectively). The atmospheric effects would cause an error of 58 μm in the GB-SAR deformation estimate. For this reason the GB-SAR sensitivity and precision are at least one order of magnitude worse than those of the RAR.

The external components of φ_{Noise} have to be considered together with the internal noise of the instrument. The most important is temporal decorrelation, which has been extensively discussed in other sections of this dissertation. This particular component of φ_{Noise} is particularly insidious because it depends on the type of measured object. Furthermore, it is more critical in the discontinuous than in the continuous mode. Another source of error worth mentioning, which is strictly related to the data processing, is coherence loss. As already discussed, see Figure 3.2, errors in the image co-registration can cause a loss of coherence and hence an increase of φ_{Noise}. Considering the case of satellite images, Hanssen (2001) estimates a noise standard deviation related to the co-registration of around 0.06 mm. Again, this error source is more important in the discontinuous mode.

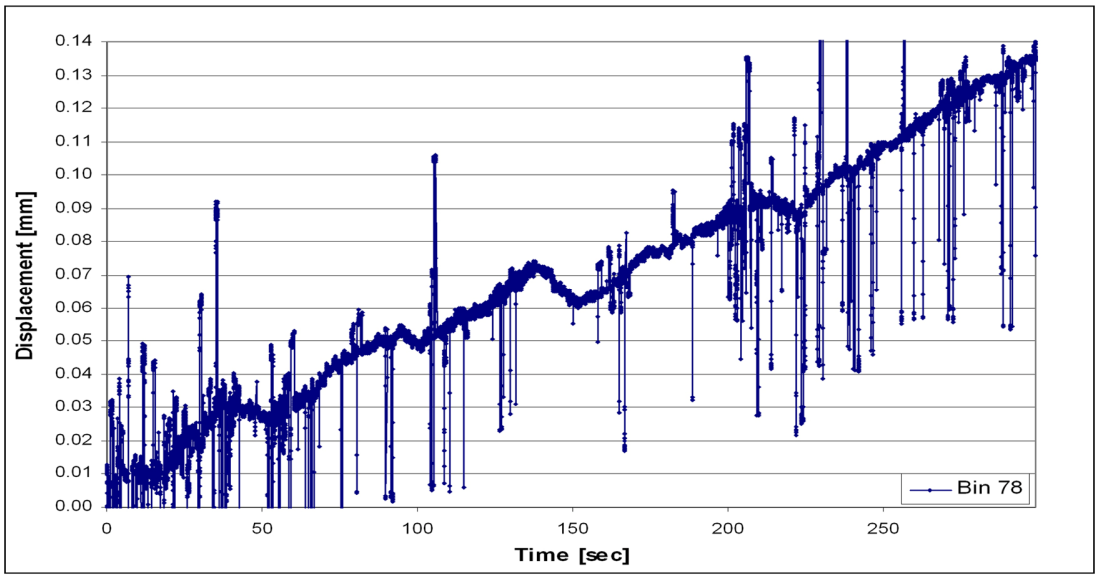

Figure 3.21: Displacement time series of the bin Rbin 78 shown in Figure 3.21, covering a period of 4.5 minutes and measured with a RAR.

The contribution of the φ_{Atmo} component is analysed by studying the dispersion of the displacement time series of points known to be stable. The results were obtained by analysing original GB-SAR data, without estimating and removing the atmospheric component. In order to highlight the contribution due to φ_{Atmo}, CRs of high quality (low φ_{Noise}) were used, considering different distances to the reference point (where φ_{Atmo} is zero by definition). Data were collected at two different sites with different environments (sea in the case of Algeciras and mountain in the Vallcebre test site), and working at different ranges from the radar: 2000 m and 600 m, respectively. The use of CRs allowed minimizing the effects of temporal decorrelation. Using CRs located at different distances from the reference point allowed to separate the errors related to φ_{Noise} from those related to atmosphere, which are mainly distance-dependent.

The results from the Vallcebre test site are shown in Table 3.2. Four CRs, located at different distances from the reference point and at 600 m from the radar, are considered. The table shows that the standard deviation of the time series increases with the distance of the CR with respect to the reference. This result is clearly due to the atmospheric contribution. A standard deviation of 0.5 mm is reached at 65 m, which represents a relatively small distance if compared to typical application scenarios. Table 3.2 shows also the results from the second test site where two CRs were installed at a distance of less than 100 m from the reference point. The numbers obtained are similar to the previous ones. It is worth underlining that in this case the mean distance of the CRs to the radar is approximately 2000 m.

An additional result is shown in Figure 3.22. The plot corresponds to both sites and shows the loss of precision as a function of distance to the reference point, which was computed over CRs and natural reflectors. The latter ones are reflectors which have small DA (less than 0.2). The standard deviation reached for both natural reflectors and CRs is of the same order of magnitude, which indicates that atmosphere is the dominant component. Similar results are shown by the green dots (Algeciras measurements), even though in this case the CRs were located at about 2000 m from the radar.

	Point name	Distance to reference [m]	Standard deviation [mm]
Vallcebre	*P1*	*27.6*	*0.2*
	P2	*43.5*	*0.2*
	P3	*55.0*	*0.3*
	P4	*65.2*	*0.5*
Algeciras	*P1*	*90.0*	*0.5*
	P2	*98.0*	*0.7*

Table 3.2: Dispersion of displacement time series, which correspond to four CRs (P1-P4) located in stable areas of the Vallcebre test and two located in the Algeciras site. The CRs are ranked according to their distance to the reference point. The dispersion is measured by the standard deviation of the displacements.

Two main conclusions can be drawn from these results. Firstly, that at very short distances, below 20-30 m, where the APS effects are practically negligible, the time series dispersion over CRs has a standard deviation of 0.2-0.3 mm. Working with highly coherent natural reflectors should not suppose a significant increase of this number. Secondly, the precision decreases linearly with respect to the distance to the reference point: this is due to the APS effects. It is worth noting that all the results shown in this section refer to original GB-SAR data, without removing the atmospheric phase component. The decrease of the precision can be minimized by properly modelling and removing the APS.

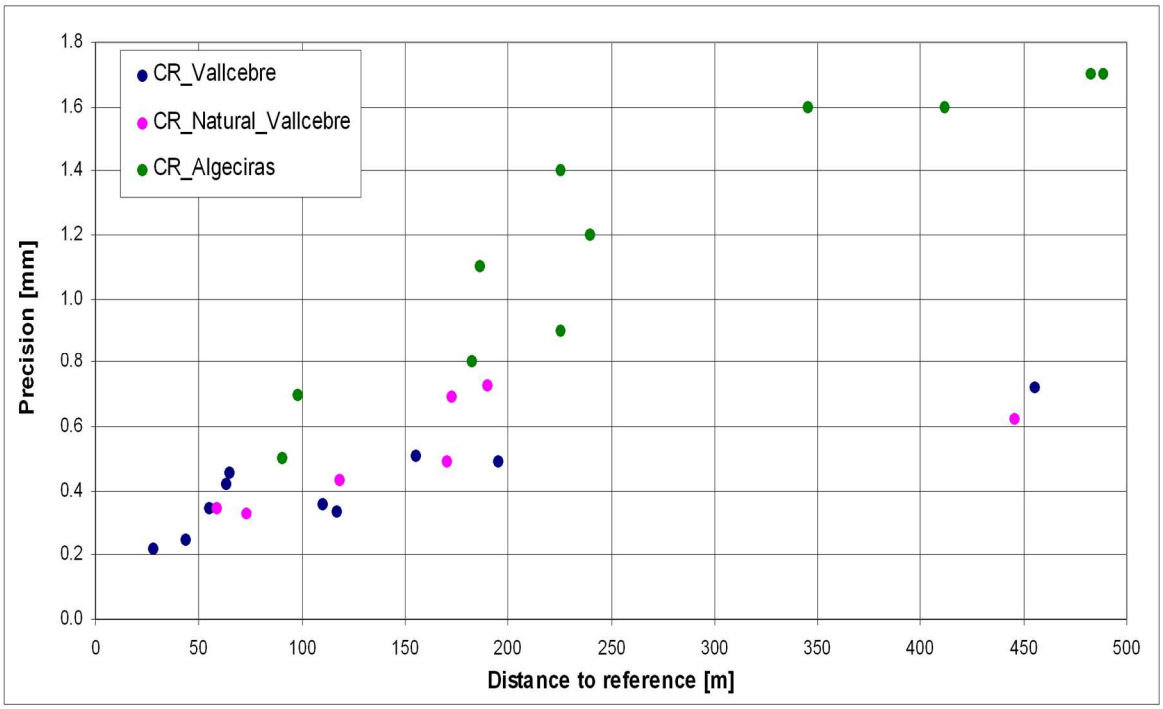

Figure 3.22: Dispersion of displacement time series plotted against the distance to the reference point. The plot displays data from the Vallcebre (Barcelona) test site, including CRs and natural reflectors, and from the Algeciras (Spain) test site.

3.9.2. Analysis of the accuracy: a validation experiment

This section describes a validation experiment performed to characterize the Ku-band GB-SAR system IBIS-L. The validation test was based on the GB-SAR estimation of the displacements imposed to a CR, which were measured independently, with sub-millimetre precision, using a micrometer. In this experiment the sensor to target distance was 44 m and a series of 12 images was acquired. The CR was shifted between consecutive acquisitions while the GB-SAR remained stable. The micrometre indicated a maximum displacement of 12 mm. In this experiment image co-registration was not performed. The GB-SAR procedure described in this chapter was applied to obtain the displacement time series shown in Figure 3.23.

The differences between the reference displacements, measured by the micrometer, and the estimated GB-SAR displacements are shown in Figure 3.23. The differences range from -270 to 100 μm; the mean difference is 90 μm with a standard deviation of 110 μm. This experiment is useful to show the sub-millimetre accuracy of close-range GB-SAR measurements. To correctly interpret these results it is worth recalling that they refer to a specific GB-SAR system: the results may be sensibly different for other systems. Furthermore, they were achieved using a CR: they apply to very good reflectors. The obtained numbers can not be extrapolated to natural reflectors.

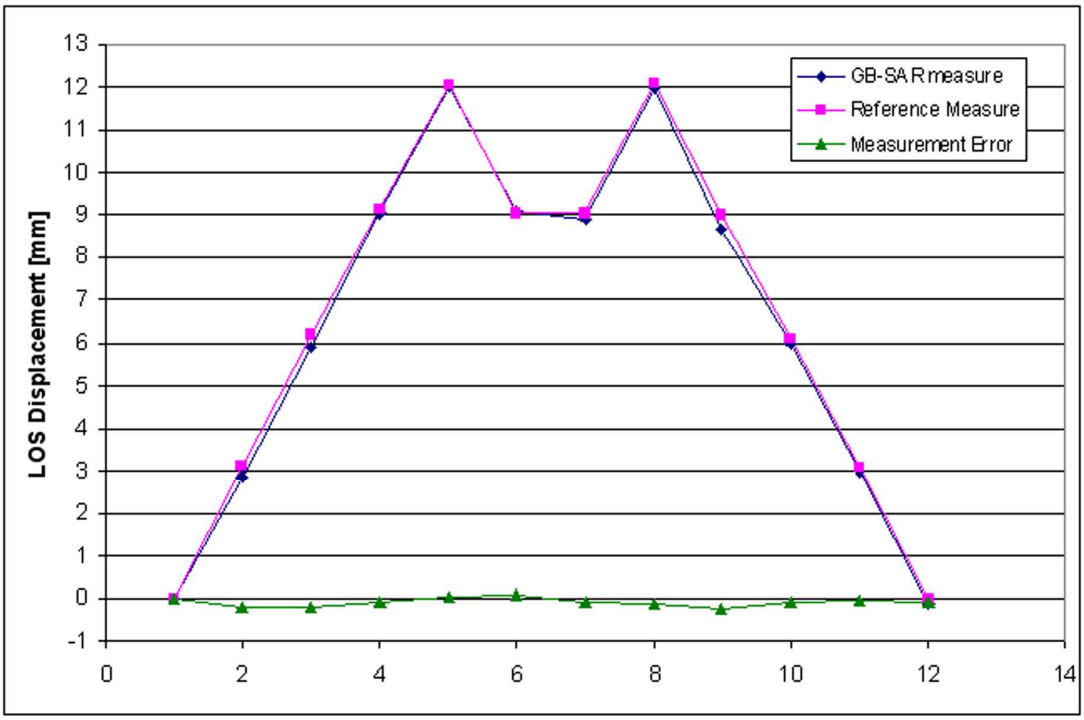

Figure 3.23: GB-SAR validation experiment using a CR and a micrometer. The plot shows the reference displacements, which were measured by using a micrometer (pink line), the displacements estimated by GB-SAR (blue line) and the difference between these measurements (green line), which represent the estimated displacement errors.

Chapter 4

A 2+1D phase unwrapping algorithm

This chapter presents an alternative method to the direct integration step described in Chapter 3. The method is designed to improve the robustness of the whole interferometric procedure by introducing independent controls on one of the main error sources, i.e. 2D phase unwrapping. It involves a two-stage procedure: a 2D phase unwrapping, which is followed by a 1D pixel wise unwrapping. The procedure, which is named 2+1D phase unwrapping, represents a new unwrapping algorithm, which works separately on the space and time domains.

In the first part of this chapter the algorithm is fully described, step by step, and its behaviour is illustrated by using a set of simulated data. The second part of the chapter describes a real case study, where the relative displacements of a dike were monitored. This part describes the obtained results and the problems that have arisen during one month of continuous monitoring. Finally, in the last part of the chapter, a comparison between the direct integration and the 2+1D phase unwrapping algorithm is performed by using a subset of the dike monitoring dataset. The comparison demonstrates the improvements offered by the proposed phase unwrapping algorithm.

4.1. Interferogram to image transformation: 2+1D phase unwrapping

This section describes an unwrapping method developed by IG in collaboration with the Department of Earth Sciences of the University of Milan. In this development the author was deeply involved. The complete procedure involves two main stages. The first part includes a 2D phase unwrapping. Then the estimation, for each pixel, of the phase value of each SAR image (unknown parameters), is performed starting from the stack of M unwrapped differential interferometric phases (observations). The main goal of the phase estimation is detecting and, if possible, correcting the errors generated in the 2D phase unwrapping stage. This operation, which makes use of an iterative procedure based on the Single Value Decomposition (SVD) least squares (LS) method (Golub and Van Loan, 1989; Strang, 1998), fully exploits the integer nature of the unwrapping errors. In the case that the errors can not be corrected, they are rejected from the original set of observations. The second part of the proposed procedure makes a kind of 1D phase unwrapping, which is called interferogram to image transformation (int2ima): it performs, pixel by pixel, the unwrapping along the time. As said above, since this operation follows a 2D phase unwrapping, the whole procedure is named "2+1D phase unwrapping".

The main input of the complete procedure is a set of M wrapped interferogram network built from a set of N phase images, with ideally M >> N. The algorithm here

described starts once the M wrapped interferograms are 2D-unwrapped and the unwrapped interferograms are referred to a common reference point using Equation 3.11. It is worth noting that the proposed strategy is not dependent on the used 2D phase unwrapping algorithm. The proposed 2+1D phase unwrapping is fully compatible with the GB-SAR deformation estimation procedure described in Chapter 3, see Figure 4.1.

4.1.1. 1D phase unwrapping strategy

The proposed phase unwrapping strategy involves a pixel wise procedure based on the following observation equation:

$$\Delta\varphi_{MS} = \varphi_S - \varphi_M = \varphi_{Defo} + \varphi_{Atmo\_S} - \varphi_{Atmo\_M} + \varphi_{Noise} + 2k\pi \tag{4.1}$$

where $\Delta\varphi_{MS}$ is the 2D unwrapped interferometric phase, S and M are the slave and master images, respectively, φ_{Defo} is the phase component due to deformation, φ_{Atmo} is the term due to atmospheric effects, k is an integer number and φ_{Noise} is the phase noise. In the above model the observation is given by the interferometric phase $\Delta\varphi_{MS}$, while the unknowns are the master and slave image phases, φ_M and φ_S. The final estimated phases are described by:

$$\left.\begin{aligned} \widetilde{\varphi}_i &= \widetilde{\varphi}_{Defo\_i} + \widetilde{\varphi}_{Atmo\_i} \\ \widetilde{\varphi}_0 &= 0 \end{aligned}\right\} \tag{4.2}$$

where i = 1, …, N-1. Note that we estimate, for each image, the sum of the two phase terms, and not the single terms separately. For each pixel we write M equations, where M is the total number of unwrapped interferograms, and N-1 unknowns, where N is the number of images. The phase estimation is made by assuming the phase values of the first image $\tilde{\varphi}_0$ equal to zero.

There are two key parameters that drive the entire procedure. The first one is given by the so-called residuals *res* associated with the observations, which represents the difference between the original interferometric phase $\Delta\varphi_{MS}$, i.e. the input observation, and the a posteriori estimated observation:

$$res = \Delta\varphi_{MS} - (\widetilde{\varphi}_M - \widetilde{\varphi}_S) \tag{4.3}$$

The second parameter is given by the redundancy of the network of interferograms and images. For each image, it is important to consider the number of interferograms that are directly tied to it, i.e. the number of interferograms where the given image appears either as master or slave. The estimation procedure is iterative. We consider the observations whose residuals are bigger than a given threshold at each iteration, and opportunely treat them in order to improve the phase estimation. The algorithm consists of the following main steps, see also Figure 4.2:

1. Performing the first phase estimation, by means of SVD LS, and computing the corresponding residuals.
2. Identifying the residuals that are above a fixed threshold, selecting the residual that has the bigger absolute value. The observation associated with this residual is called “outlier candidate”.
3. Temporally removing the outlier candidate from the network, and performing a new LS estimation.

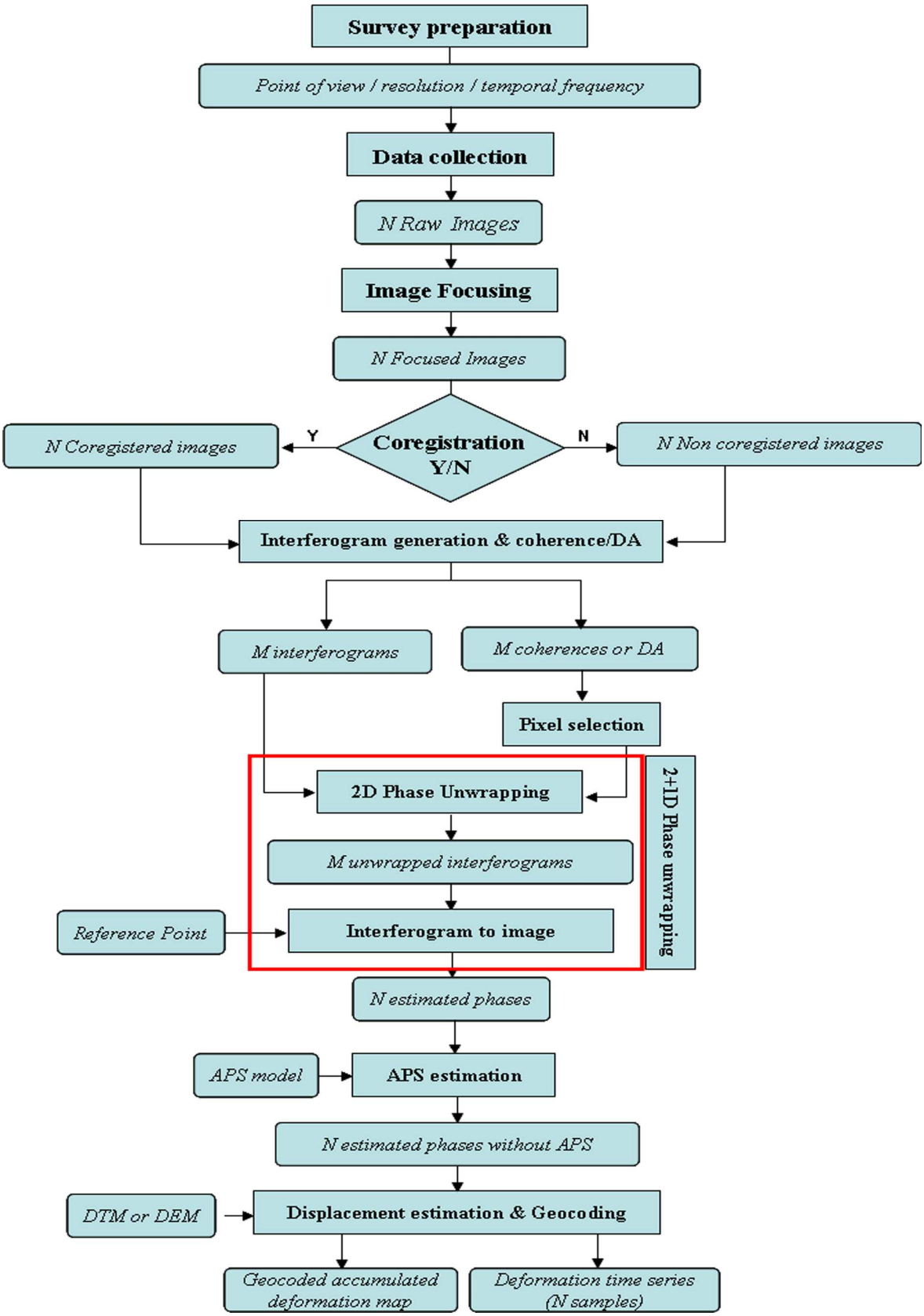

Figure 4.1: Flow chart diagram of the whole GB-SAR deformation estimation procedure, which includes the 2+1D phase unwrapping (highlighted by the red box).

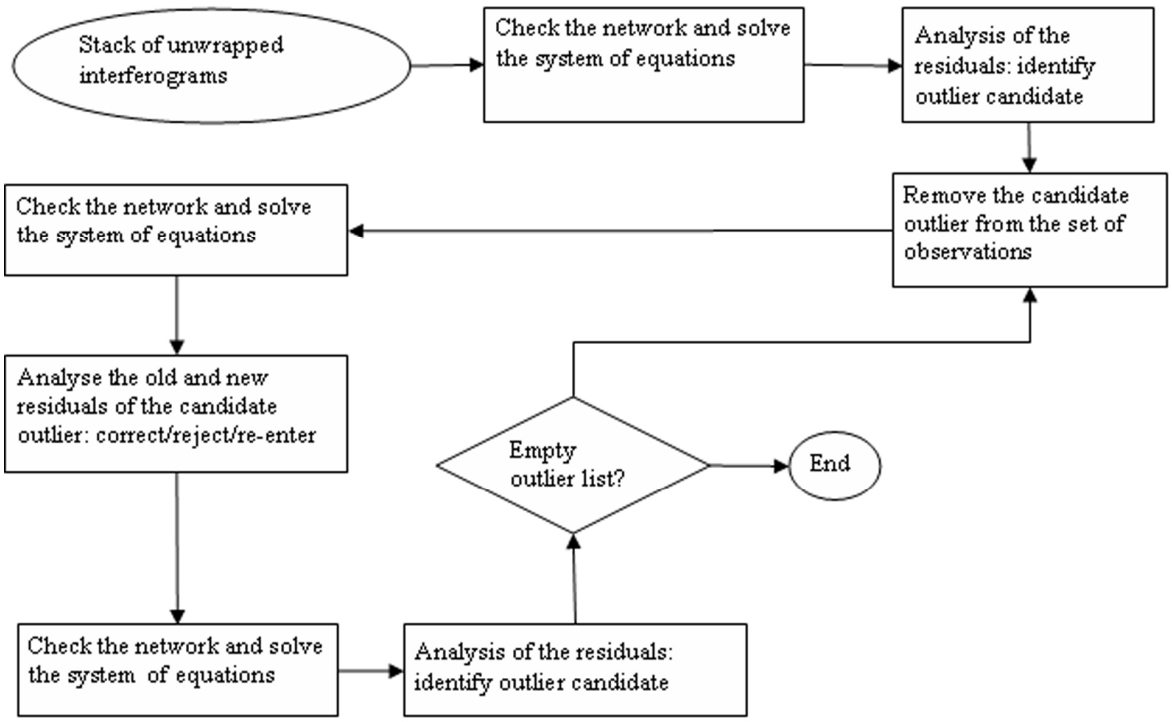

Figure 4.2: Flow chart of the proposed 1D phase unwrapping algorithm.

4. Checking the residual of the outlier candidate. If it is a multiple of 2π (within a given tolerance), the observation is corrected and reaccepted. In this way it is possible to correct for the unwrapping errors. Otherwise, the decision of re-entering or rejecting the outlier candidate is based on the comparison of its old and new residuals.
5. Performing new phase estimation, computing the residuals, and restarting the procedure from step (2). The procedure is executed iteratively from (2) to (5) until there are no remaining outlier candidates, i.e. there is no residual above the given threshold. In addition to the outlier candidates, the correction of the unwrapping-related errors is extended to all residuals that, within a given tolerance, are multiple of 2π.

As commented above, the available redundancy is a critical parameter of the procedure, which directly influences the correction, rejection or re-acceptation of outlier candidates. It is also worth noting that the elimination of an observation (interferometric phase) characterized by a low redundancy could result in a weak network. In order to avoid this, the algorithm checks the available network of images and interferograms at every iteration, and, in case of insufficient redundancy, a residual above the given threshold is not considered as an outlier candidate, i.e. it is left untouched by the algorithm. If this occurs, the corresponding parts of the network have to be checked off-line, after concluding the automatic analysis. That is, the automatic 1D phase unwrapping only works over the redundant parts of the analysed network. The main output of the procedure is the phase time series per each analysed pixel. Furthermore, the algorithm provides the standard deviation of each estimated phase, the residuals of the final least squares estimation, and the final local redundancy of each observation. All these outputs are needed to assess the quality of the estimates.

Finally it is interesting to note that the proposed model is similar to the one of geometric or "spirit" levelling, e.g. see Heiskanen and Moritz (1967). In a levelling network we estimate, by least squares, the point heights starting from levelling in a way which is similar to estimating image phases starting from interferograms. However, there are some important differences, which require implementing rather different estimation procedures. The most important one is that in a levelling network the outliers typically represent low percentages, e.g. below 1-2%, of the whole number of observations. This requires relatively simple procedures to detect outliers. By contrast, in our procedure we may experience much higher percentages of outliers, e.g. above 20-30% if they are evenly distributed in the network. This percentage of unwrapping-related error may vary as a function of different factors, like the noise, the selected point density, deformation rates, etc. A direct consequence of the high outlier percentages is that we have to devote particular care in checking the redundancy of the analysed network. Despite these difficulties, in our procedure we can exploit a specific property, which does not hold in the levelling case: the outliers are multiples of 2π.

4.1.2. **Behaviour of 1D phase unwrapping using simulated data**

In order to illustrate the performance of the procedure, we describe below the results of a test performed using simulated data. The simulated data set was based on satellite data; however, the example should be valid also for GB-SAR data. Later in this chapter is discussed an example of application of the algorithm based on real GB-SAR data. For the simulation, we used the following simplified model for the interferometric phases:

$$\Delta\varphi_k = \varphi_{ij}^{Defo} + \varphi_{ij}^{Atmo} + \varphi_{ij}^{Noise} \tag{4.4}$$

where $\Delta\varphi_{ij}^{\mathrm{Defo}}$, $\Delta\varphi_{ij}^{\mathrm{Atmo}}$ and $\Delta\varphi_{ij}^{\mathrm{Noise}}$ are the phase components due to deformation, atmospheric effects and noise, respectively; k=1,…,M indicates the interferogram number and i and j=1,…,N indicate the image number. We simulated a network of 35 images and 150 interferograms, designing a locally heterogeneous redundancy, see Figure 4.3. The minimum redundancy of the network is 3, i.e. each image has at least 3 associated interferograms. A subset of interferograms was contaminated by unwrapping errors distributed randomly:

$$\Delta\varphi_k = \varphi_{ij}^{Defo} + \varphi_{ij}^{Atmo} + \varphi_{ij}^{Noise} + 2k\pi \tag{4.5}$$

In this case k varied between -3 and 3, and the unwrapping errors affected 20% of the total number of interferograms, i.e. 30 outliers were introduced in the network. It must be underlined that the assumption of the random behaviour of the unwrapping errors is an optimistic assumption, which makes easier the detection and correction. In some cases, the unwrapping errors are related to a particular image or a set of images clustered on time and which are affected by temporal noise effects. Even so, the simulated network was considered appropriately for checking and illustrating the algorithm. The main input parameters of the procedure were:

- The outlier rejection threshold was set to 3 rad: if the absolute value of the residual was bigger than 3 then the observation was considered an outlier candidate.
- The minimum accepted redundancy after outlier rejection was 3, i.e. if an image had less than 3 images after outlier rejection then the algorithm did nothing with this image.

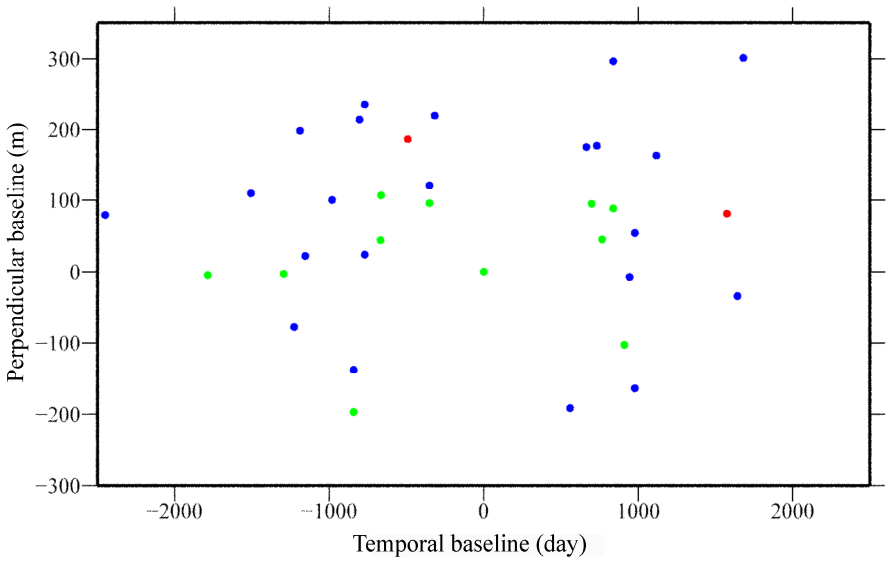

Figure 4.3: Redundancy of simulated interferogram network. This figure shows the number of interferograms (incidence value) connected to each image. Incidence values $\leq$ 4, which represent the weakest part of the network, are shown in red, values between 4 and 8 are in blue, and above 8 in green.

- The tolerance ε for correcting an observation was set to 0.3 rad.
- The reaccepting threshold was set to 1.5 rad, i.e. if the residual of the observation i was smaller the 1.5 after the outlier rejection then it was re-accepted.

Figure 4.4 illustrates the results of the outlier correction and rejection procedure, showing the initial interferogram network and its changes until the last iteration, which in this case is the 13$^{\text{th}}$ one. In the first plot are shown, in blue, the outliers introduced in the network, while in the following plots are shown the results of three iterations, highlighting the current candidate outliers (in red, for the 1$^{\text{st}}$ and 6$^{\text{th}}$ iterations), the eliminated outliers (purple) and the corrected outliers (green). In the last iteration all outliers are corrected with the exception of two of them, which are highlighted in blue. The two missing corrections are due to the low redundancy of the corresponding observations, see Figure 4.3: for those observations the algorithm did not perform outlier correction or rejection because not enough information was available locally in the network.

The outlier correction and rejection procedure has a direct impact on the observation residuals at the different iterations, see Figure 4.5. In the first plot, which corresponds to the first iteration, most of the residuals have relatively high values, which are caused by the presence of unwrapping errors (simulated outliers, shown in blue). In the other plots one may appreciate the evolution of the residuals. For instance, one may observe that between the 6$^{\text{th}}$ and 7$^{\text{th}}$ iterations the candidate outlier, shown in red, is removed (empty circle). In the last iteration the observations that were re-entered are shown in yellow. Most probably these are originally bad residuals due to outliers in "neighbouring observation", which decrease during the correction and rejection procedure. In the last iteration most of the residuals are small, with the exception of two of them, in blue, which are not corrected due to the low redundancy of the corresponding observations. Apart from these two observations, for which the network does not provide enough information, the rest of the network is free of outliers.

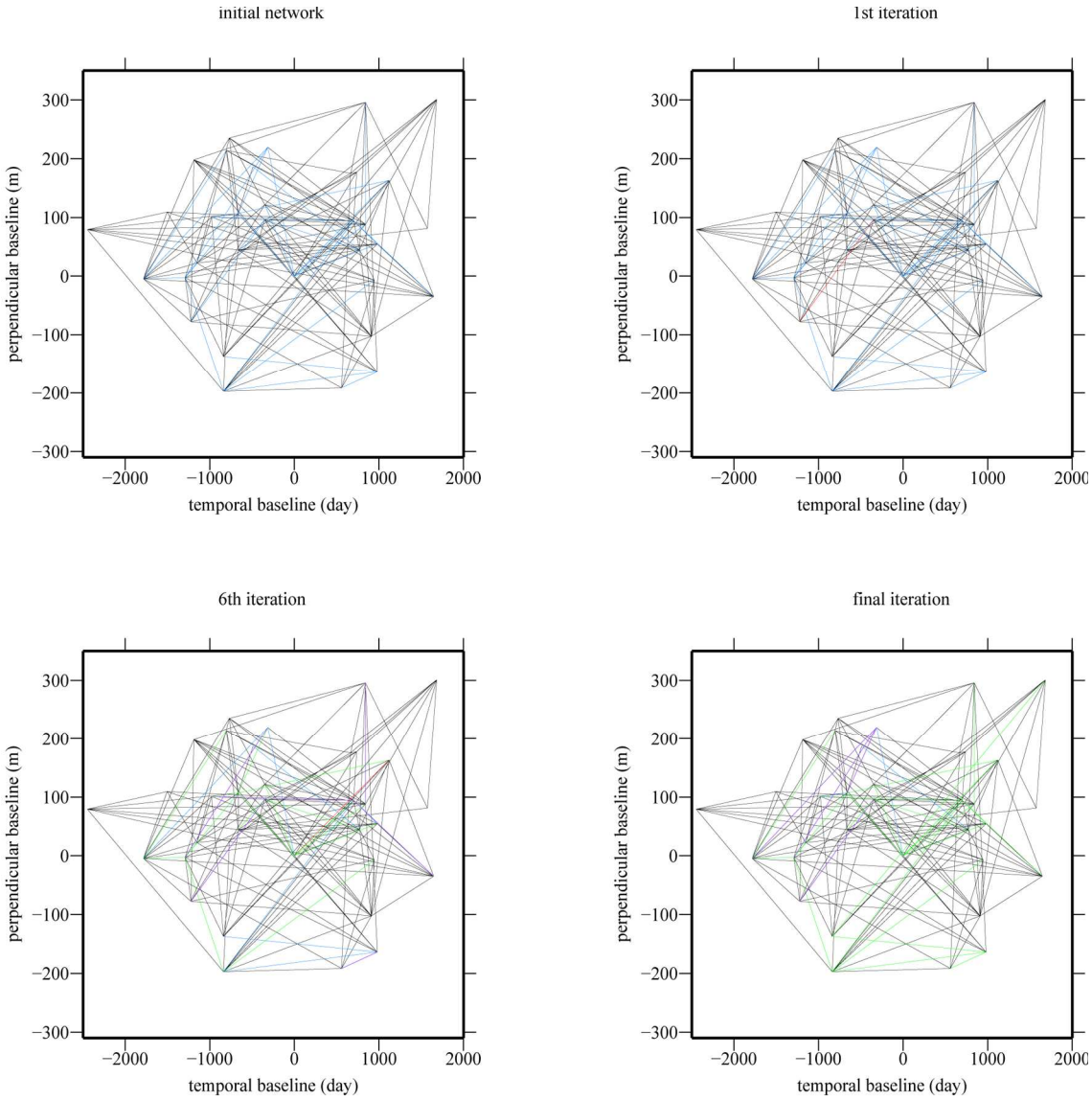

Figure 4.4: Evolution of interferogram network through the outlier correction and rejection process, using simulated data. The blue lines indicate the interferograms corrupted by unwrapping errors, the red lines indicate the outlier candidate (only for the 1st and 6th iterations), the green lines show the interferograms corrected during the processing, and finally the purple lines show the rejected outliers. Two outliers remain in the network at the end of the process.

The two remaining high residuals have to be checked manually after the automatic procedure, because they have a direct impact on the final estimation of image phases. Figure 4.6 (above) shows an example of phase time series, while in the same figure (below) are shown the standard deviations of the residuals of all interferograms related to a given image. One may observe that images 1 and 24 (in blue), which are related to the two remaining observations affected by outliers, are characterized by high standard deviations. Note that in the same figure the standard deviation of images 4 and 9 is equal to zero because the standard deviations of all images with less than two interferograms are automatically set to zero.

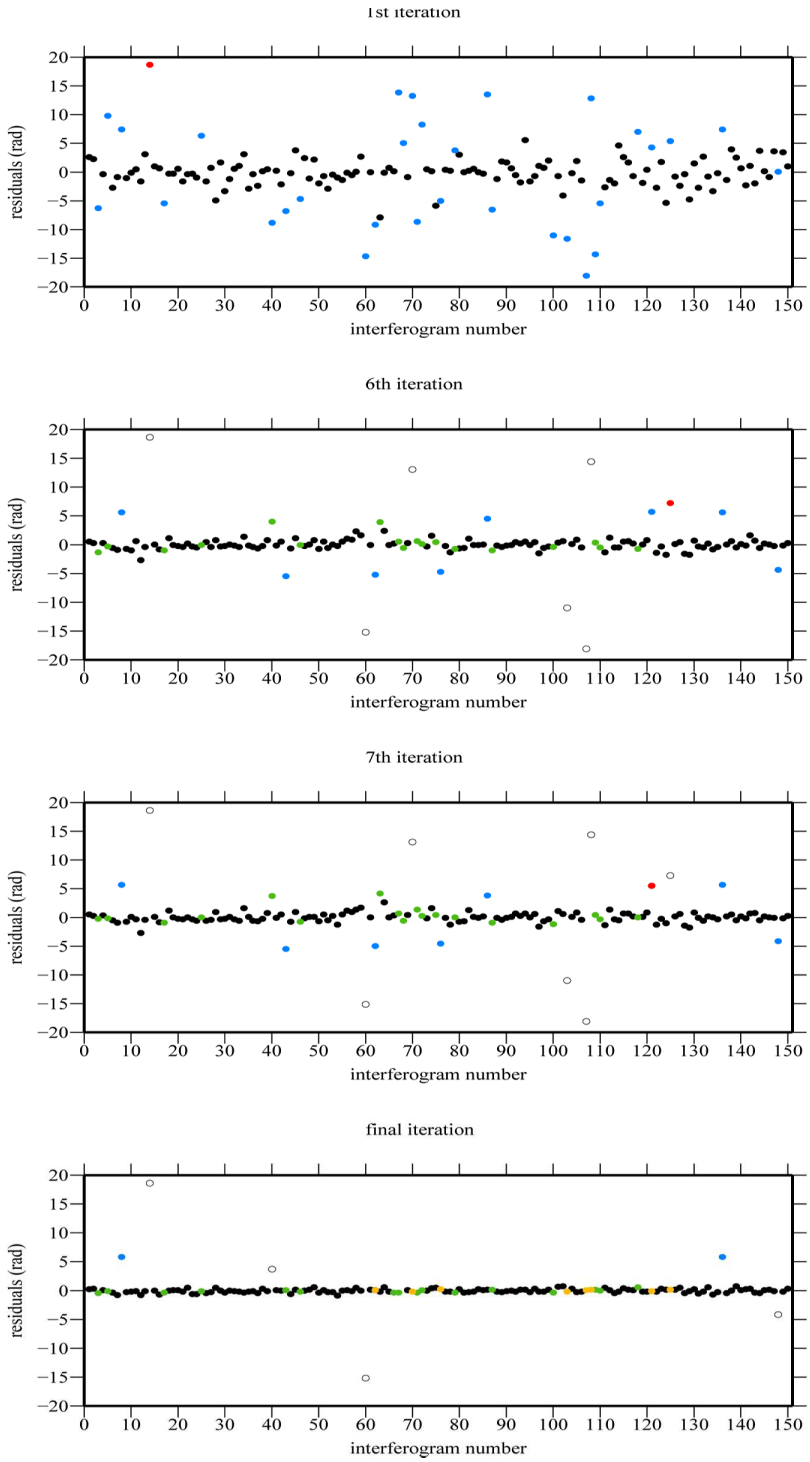

Figure 4.5: Evolution of residuals through the outlier correction and rejection process based on simulated data. The four plots correspond to the 1st, 6th, 7th and last iterations. The blue points indicate the observations with unwrapping errors (simulated outliers), the red points the outlier candidates, the green points the corrected outliers and the white points indicate the temporally removed outliers. Note that in the last iteration the white points are the definitely removed outliers, while the yellow points are for outliers removed in previous iterations but finally corrected and re-entered. One may notice a global decrease of residuals until the last one, where most of the residuals are close to zero with the exception of two of them due to low network redundancy.

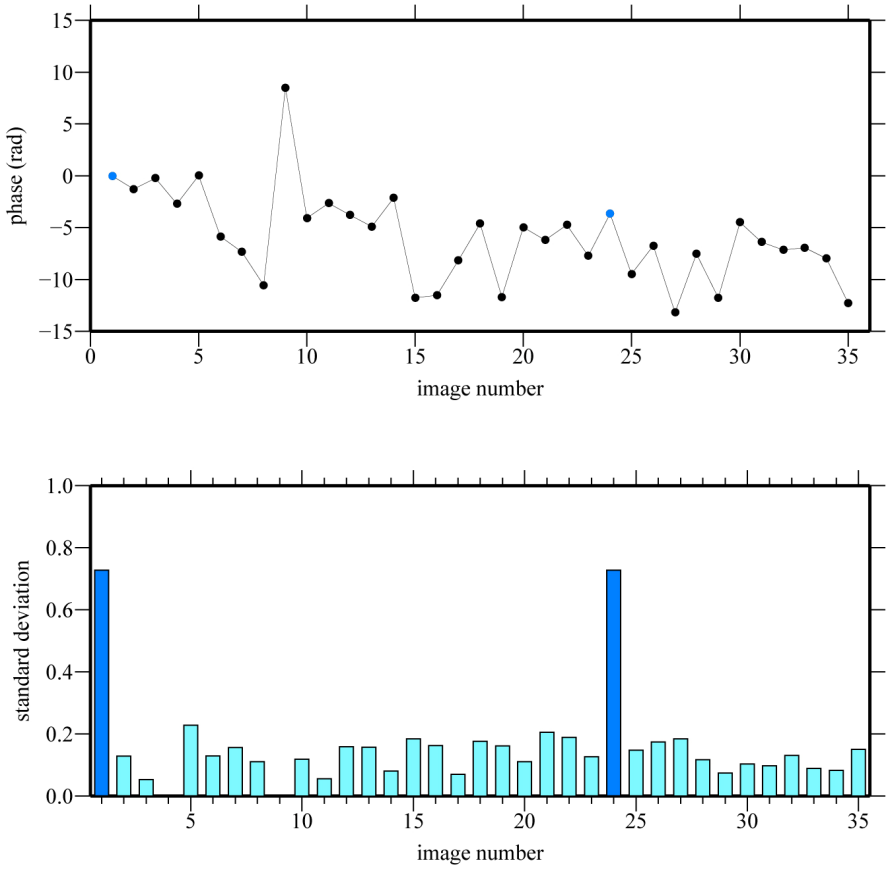

Figure 4.6: Estimated phase time series using the simulated data (above), and associated standard deviations. The images 1 and 24, which have high standard deviations, are directly tied to the two uncorrected interferograms affected by simulated outliers.

4.2. A real case study: the dike of Algeciras

This section describes in detail the main results of a GB-SAR monitoring campaign carried out in the Algeciras harbour (South Spain). This real case study is used in this chapter to emphasize one of the main limitations that can be experienced by applying the standard approach described in Chapter 3: the appearance of some unwrapping errors on the time series, which requires a time consuming, one by one, time series analysis. As it is shown later, this kind of analysis limits the potentials of the technique because it can be only performed for a relatively small set of points. This limitation is partially solved by the proposed 2+1D phase unwrapping. Later in this chapter, an entire sub-section is devoted to the comparison between direct integration and 2+1D unwrapping.

The Algeciras campaign was planned to measure the relative displacements of the different portions of a dike located approximately 500 m off the coast, see Figure 4.7. The site distribution presented a challenge from the viewpoint of GB-SAR monitoring: the geometry of the scene required finding an optimal viewpoint for the GB-SAR in order to get the best compromise between dike coverage and displacement sensitivity. The selected viewpoint was the highest point of the Algeciras harbour: the roof of the 60-m height control tower. Although it was quite far from the area of interest, about 2 km, there were no other suitable points of view. In Figure 4.7 the blue rectangle shows approximately the measured area, and the red one highlights the dike.

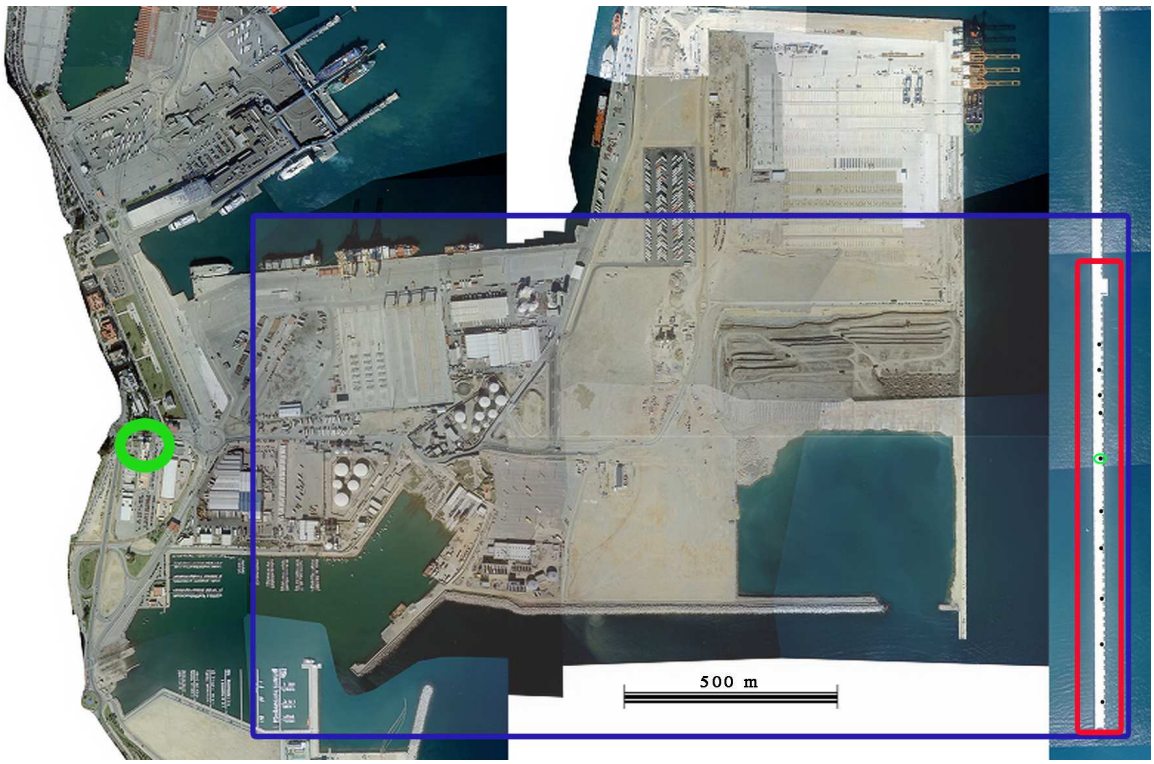

Figure 4.7: Port of Algeciras (South Spain) test site. The green circle indicates the position of the control tower, where was located the GB-SAR. The blue rectangle shows the measured area and the red one the object of interest: a dike. The location of 10 CRs is indicated by black dots; the one bounded by a green ellipse is the reference CR.

The used system was the Ku-band IBIS-L system available at the IG. No information about the expected deformations was known a priori. The system was configured in order to acquire one image every 10 minutes. This was the maximum temporal sampling rate for the selected acquisition parameters, see Table 4.1. The duration of the campaign was 34 days. During this time the system did not acquire over about 24 hours due to a software error. The total amount of acquired images was 4974.

In order to ensure getting good measurements over at least a set of selected points, 10 CRs were installed over the dike. The CRs were distributed approximately uniformly along the measured part of the dike. The CRs used in this test case are shown in Figure 2.7. One of them was used as a reference point, i.e. all the displacements measured with GB-SAR refer to it. The maximum distance between the reference and the CRs is 450 m. In term of range distance to the GB-SAR, all the CRs are included in a range crown of about 100 m.

Range resolution	[m]	*0.5*
Azimuth resolution	[rad]	*0.004*
Acquisition interval	[min]	*10*
Maximum range	[m]	*2500*

Table 4.1: Port of Algeciras (South Spain) test site: GB-SAR acquisition parameters.

4.2.1. Data processing

In order to simplify the computational cost and the analysis effort, the data analysis was focused on the dike, neglecting the rest of the scene. The images were processed considering two separated periods, before and after the above mentioned software error: this made the analysis of the whole period easier, avoiding possible problems during the 24 hours of lack of data. It was assumed that nothing happened in the dike during the 24-h period. The number of processed images per each period was around 2400 images.

In a first stage, the procedure described in Chapter 3 was applied for each period. However, image co-registration and APS estimation were not performed. The APS effects were considered, at least in a first approximation, negligible due to the relatively small size of area of interest. The used pixel selection criterion was the DA. Figure 4.8 shows the MA, the DA and the final set of points, which were selected with a DA threshold of 0.3. The MA and DA were calculated using a subset of 300 images distributed along the whole period. The CRs are easy to identify on the MA image; the horizontal white lines of this image are due to the strong response of the CRs and the associated side lobes. The grey circle in the MA image shows the reference CR. One may observe the parabolic geometry of the dike, which is due to the polar acquisition geometry of the GB-SAR, see also Figure 2.3 in Chapter 2, which displays the MA image of the whole scene.

A DSM of the dike was not available. For this reason the geocoding was performed by assuming a flat area, with constant height equal to zero. This made more difficult the interpretation of the results.

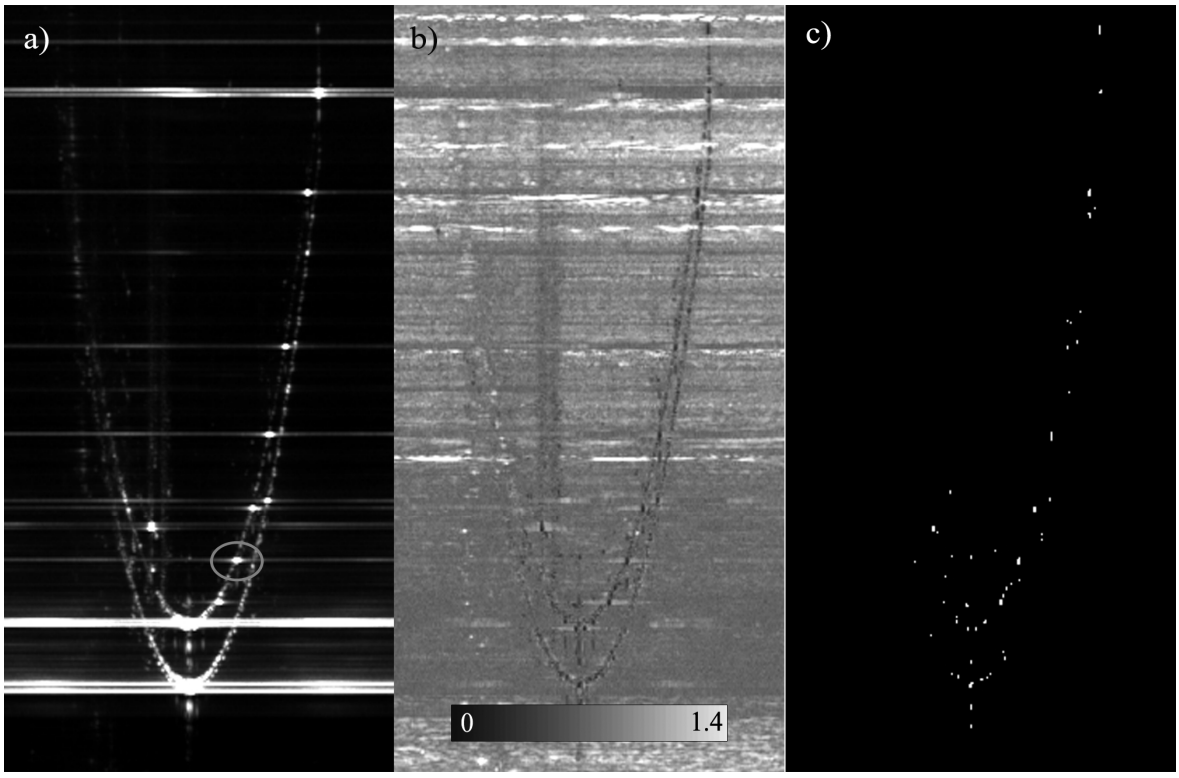

Figure 4.8: Port of Algeciras (South Spain) mean amplitude and DA: mean amplitude MA image (a), amplitude dispersion, DA (b) and final set of selected points, shown in white (c). The grey circle in the first image shows the reference CR.

4.2.2. Analysis of the results

The main goal of the measurements was to estimate the relative displacements within the dike. A preliminary analysis was focused on the CRs because they ensure a low noise level, minimizing the probability of aliasing. Figure 4.9 shows the CR distribution, while Figure 4.10 shows the estimated deformation time series for each CR. These time series clearly indicate that no relative displacements occurred in the observed period between the CRs and the reference CR.

During the phase unwrapping stage of these data some unwrapping errors occurred, which were manually detected and corrected. In this case the unwrapping errors were easy to identify because the points are stable and the observed phase jumps in the time series correspond to multiple values of 2π. A possible cause of these aliasing errors can be the wind, which affected the measurements in different moments of the observed period, making them noisy. Figure 4.9 shows, for each CR, the standard deviation of the deformation time series. Considering that all CRs are stable during the observed period, the standard deviation of the time series directly measures the dispersion of the displacement estimates over time. One may observe that the bigger the distance to the reference CR (P6) the higher is the standard deviation of the time series. This result, which was already analysed in Chapter 3, see Figure 3.22, is basically due to the atmospheric effects. It is worth recalling that for these data the APS estimation was not performed. All the standard deviations are below 1.6 mm.

In order to confirm the results obtained using the CRs, the analysis was extended to the rest of coherent points of the dike. The total number of measured coherent points is 286, see their distribution in Figure 4.8c. Again, the analysis was constrained by the existence of some phase unwrapping errors which compelled to the selection of a subset of 42 points whose time series were analysed one by one. The analysis confirmed the results obtained with the CRs: the dike suffered no differential movements during the measured period.

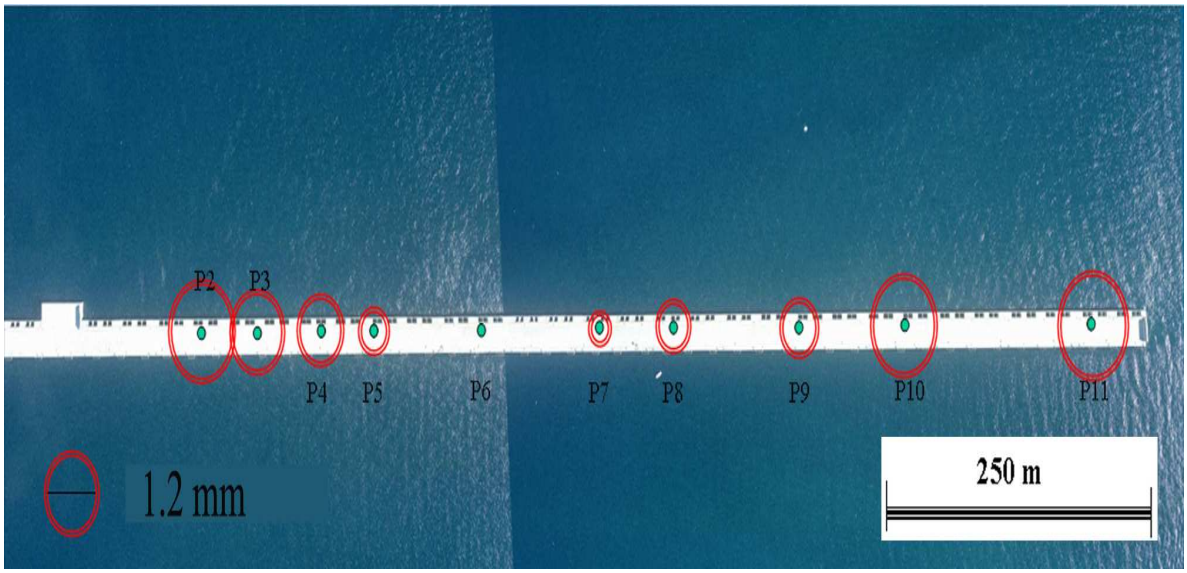

Figure 4.9: CR distribution and standard deviation of the displacement time series, which is displayed using red circles with diameter proportional to the standard deviation value.

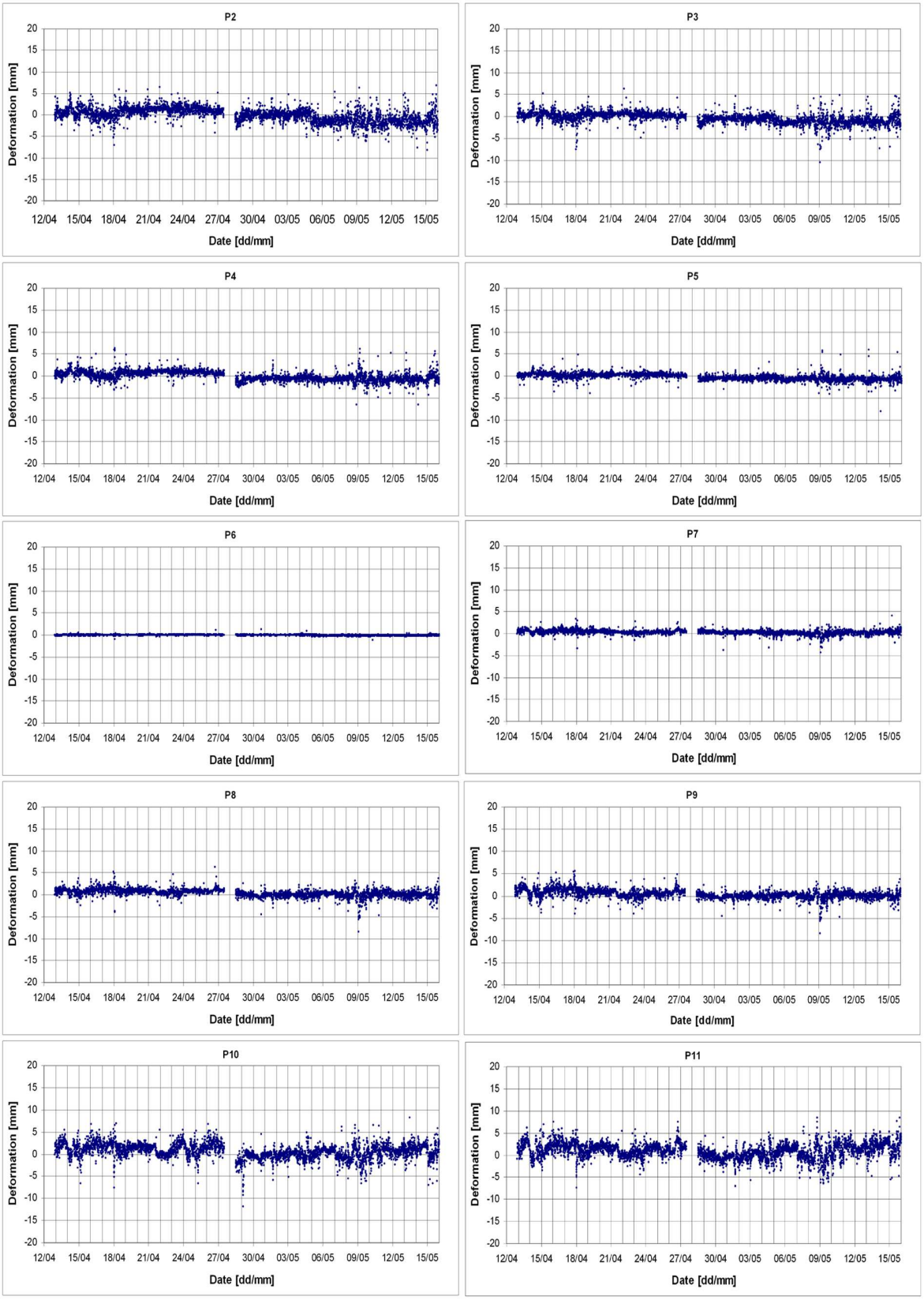

Figure 4.10: Temporal evolution of the CR during the 34 days. The deformation axis (Y-axis) ranges between -20 and 20 mm.

In addition, the analysis highlighted some points showing a strong pattern in the deformation time series: these points have 12-h periodical variations, which a further investigation proved to be strongly correlated with the tide effects. Figure 4.11 shows the obtained result over few of these points distributed along the dike by using the direct integration (above) and after time series analysis and correction (below). There are significant differences between these results. Looking at the results of the direct integration, a possible interpretation could be that these points are structures of the dike, e.g. defences or upstairs, which are all affected by the tide, having however different displacements. However, by analysing point by point independently, it was possible to detect some unwrapping errors and correct for them. It is worth mentioning that a priori the identification of these errors was not a trivial task. The interpretation of the corrected results differs substantially from the above interpretation: for all points the GB-SAR was basically observing the same phenomenon, i.e. the change of the sea level. To understand this, it is necessary to understand the specific geometry of the scene: some areas of the dike form a perfect dihedral with the sea surface, providing a highly coherent response along time, see Figure 4.12. Let's assume that the sea level decreases by h: the GB-SAR to target distance increases by δ, i.e. from d to $d'=d+\delta$. Assuming that between two consecutive GB-SAR acquisitions $\delta \leq (\lambda/4)$, being λ the wavelength, δ can be directly estimated from the unwrapped interferometric between consecutive phase images. Provided that h is negligible, if it compared with the GB-SAR height (60 m), then we can get an approximate value $\alpha=\tan^{-1}(60/2239)$ and, as a consequence, the GB-SAR-based estimate of the level change $h = \delta$ /sen(α).

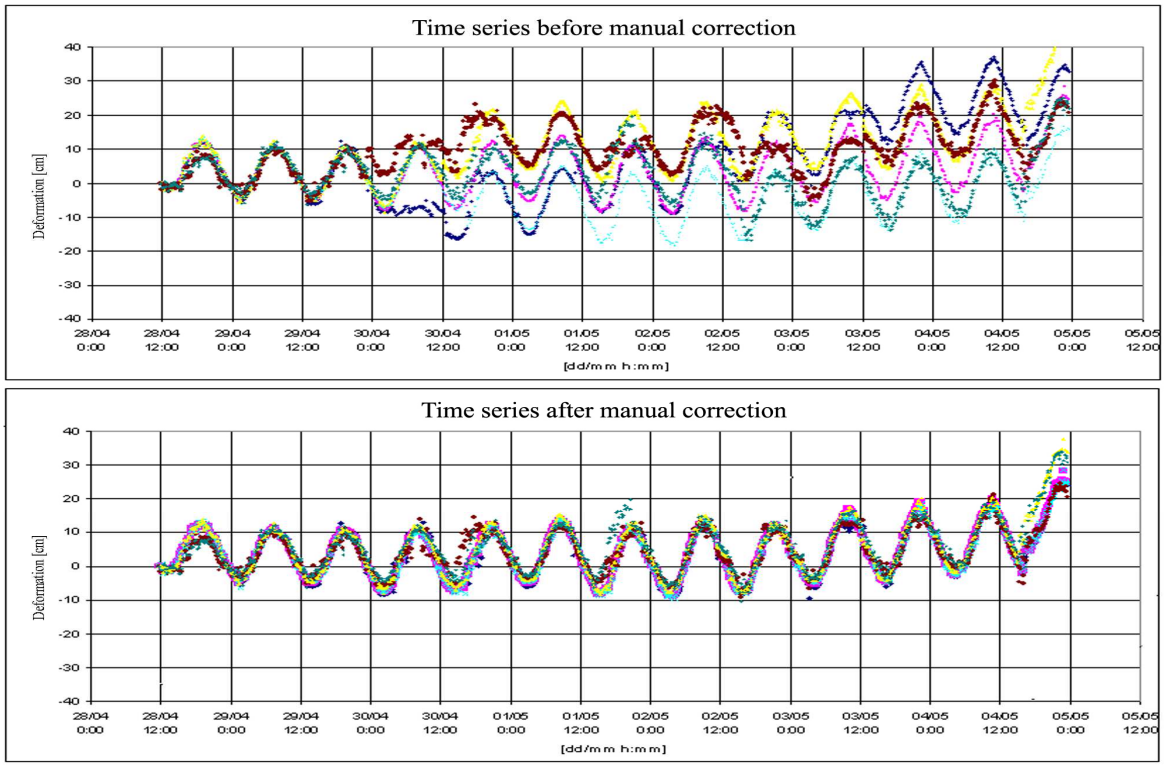

Figure 4.11: GB-SAR time series with a periodical pattern, which is caused by sea level changes due to tide effects. Original time series obtained by direct integration (above) and time series after manual correction of the unwrapping errors (below).

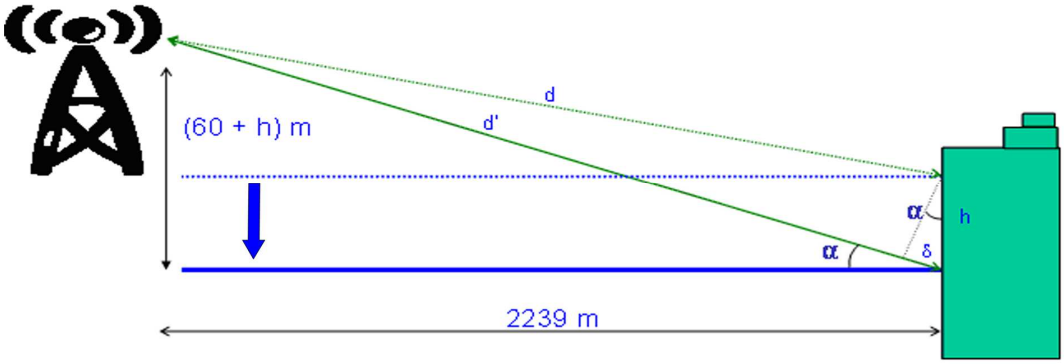

Figure 4.12: GB-SAR measurement of sea level changes due to tide effects: acquisition geometry. The green structure represents the dike and the black tower indicates the GB-SAR position. The dotted blue line represents the sea level at a given time T1 and the blue thick line the level at the time T2. The sea surface and the dike form a dihedral.

A nice validation of these results was made by comparing them with independent measurements of the sea level change, coming from the tide gauge of the Algeciras bay and provided by Puertos del Estado (www.puertos.es). The validation result for one point is shown in Figure 4.13: there is a good correspondence between the GB-SAR estimated of the sea level and the validation data. Note that although the data is represented as a continuous data the real measurements are discrete measurements. The GB-SAR result is sampled every ten minutes while the validation data is sampled every hour: some of the observed differences can be due to it.

It is worth noting that the above results were obtained by manual correction of the unwrapping errors. This manual process, which is slow and cumbersome, was feasible because it was limited to a small set of points. Next section addresses specifically the automatic capability of the proposed 2+1D phase unwrapping. It shows the efficiency of this phase unwrapping to automatically detect and correct unwrapping errors for all the measured points.

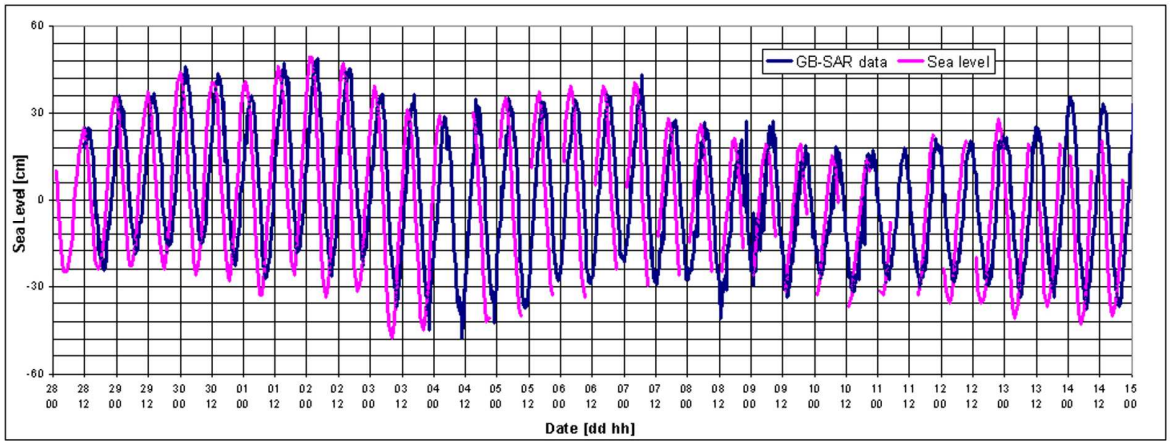

Figure 4.13: Validation of the sea level changes measured by GB-SAR. Validation data obtained by the tide gauge of the Algeciras bay and provided by Puertos del Estado, www.puertos.es (pink line), and GB-SAR sea level estimates (blue line). There is a good correspondence between the two types of data.

4.2.3. Direct integration and 2+1D unwrapping comparison

In this section a subset of the Algeciras dataset is used to evaluate the behaviour of the 2+1D phase unwrapping algorithm with real data. The subset, which contains 308 images covering two days of monitoring, were selected by including a period characterized by aliasing problems, detected during the manual analysis. The reason of using only two days was that the algorithm is currently not optimized for processing big amounts of data. Future works will be devoted to improve the computing efficiency aspects.

The interferogram network was designed to ensure a minimum starting redundancy of 5 interferogram for every image. The total number of generated interferograms was 1525, which were 2D unwrapped, and then the int2ima step was performed. The number of unknowns (images) was 308; the minimum redundancy after outlier rejection was 3 and finally the outlier rejection threshold was 3.

The total number of analysed points was 228. The total processing time was 155 minutes. However, the time can not be generalized because the time of processing is strongly dependent on data quality. The mean number of outlier candidates per point was 10, less than 1% of the observations, and the maximum number was 57, i.e. 4% of the observations. The mean number of unwrapping errors detected and corrected for each point was 3, i.e. about 30% of the outlier candidates. If we look at the global process, a set of 4649 outliers were detected and 582 of them were corrected. The rest of the outlier candidates were detected as false outliers and then reaccepted in the network, or simply rejected without correction, due to a weak local redundancy of the network. These numbers give an idea of the importance of applying automatic algorithms.

Figures 4.14 and 4.15 show some examples of int2ima results (green) and compare them with those of the direct integration (blue). Figure 4.14 shows some examples based on stable points. There are two aliasing errors in the direct integration time series. Even though they seem to be evident, it is worth observing that a simple step detector would hardly be capable of correcting them because the phase noise hides the "2π jump" between consecutive images. By contrast, the int2ima solution properly detects and corrects for the two aliasing errors. Figure 4.15 shows some more complex examples. The first plot concerns a stable point: the result of the direct integration shows several aliasing errors in the last period of the measurements. By contrast, the int2ima properly detected and corrected the aliasing errors, correctly evidencing the stability of the point. The main cause of these aliasing errors could be the phase noise, which seems higher in the last part of the measured period. The second plot shows one example with a strong periodical pattern, due to sea level changes. Again, in this case the solution from the direct integration is affected by different aliasing errors, which are properly corrected by the int2ima algorithm. Finally, the last plot shows a more difficult example, where the direct integration solution shows a strong displacement variation. Over the same point, the int2ima found 20 outliers candidates, correcting 12 of them: the final result, which shows a stable point, completely differs from the other solution.

The results shown in Figures 4.14 and 4.15 can be considered, intuitively, positive examples. This, however, is based on the interpretation of the results. Using the information available from the int2ima, it is possible to derive a kind of quality index, which describes, in an automatic way, the quality of the phase unwrapping estimates. Without going into details, this interesting feature of int2ima, which is based on the analysis of the residuals, is briefly discussed below. Once the corrections are applied, if all observations are consistent the residuals are expected to be zero or close to zero. In Figure

4.16 are shown the time series and the residuals of the first and last iteration of a given pixel. One may observe five short periods with high residuals in the first iteration (blue dots). If we look at the green circle, we observe that the residuals of the last iteration (green dots) are zero: all the aliasing errors were properly detected and corrected. Looking at the blue circles, we find examples where the residuals of the last iteration are not zero, but the corresponding results seem to be not critically affected. In these cases the algorithm did not act because most of the residuals are below the outlier threshold of 3 rad, but the redundancy is high enough to get a good estimate of the phase value. Finally, let's consider the period marked by the red circle, where the int2ima provides the same solution of the direct integration, i.e. it does not make any correction. In this case most of the observations are outliers candidates, which are uniformly distributed between -3 and +3 rad. This is a clear example of high concentration of unwrapping errors in the same part of the network. In such cases the algorithm cannot correctly detect the unwrapping errors. The positive aspect is that, by properly analysing the residuals, it is in principle possible to identify the concentration of high residuals in the same portion of the network, and thus alerting, through a quality index, of the poor quality of the given estimate. This is a remarkable advantage of the algorithm, not fully exploited so far, which has a positive impact on the interpretation and exploitation of the results.

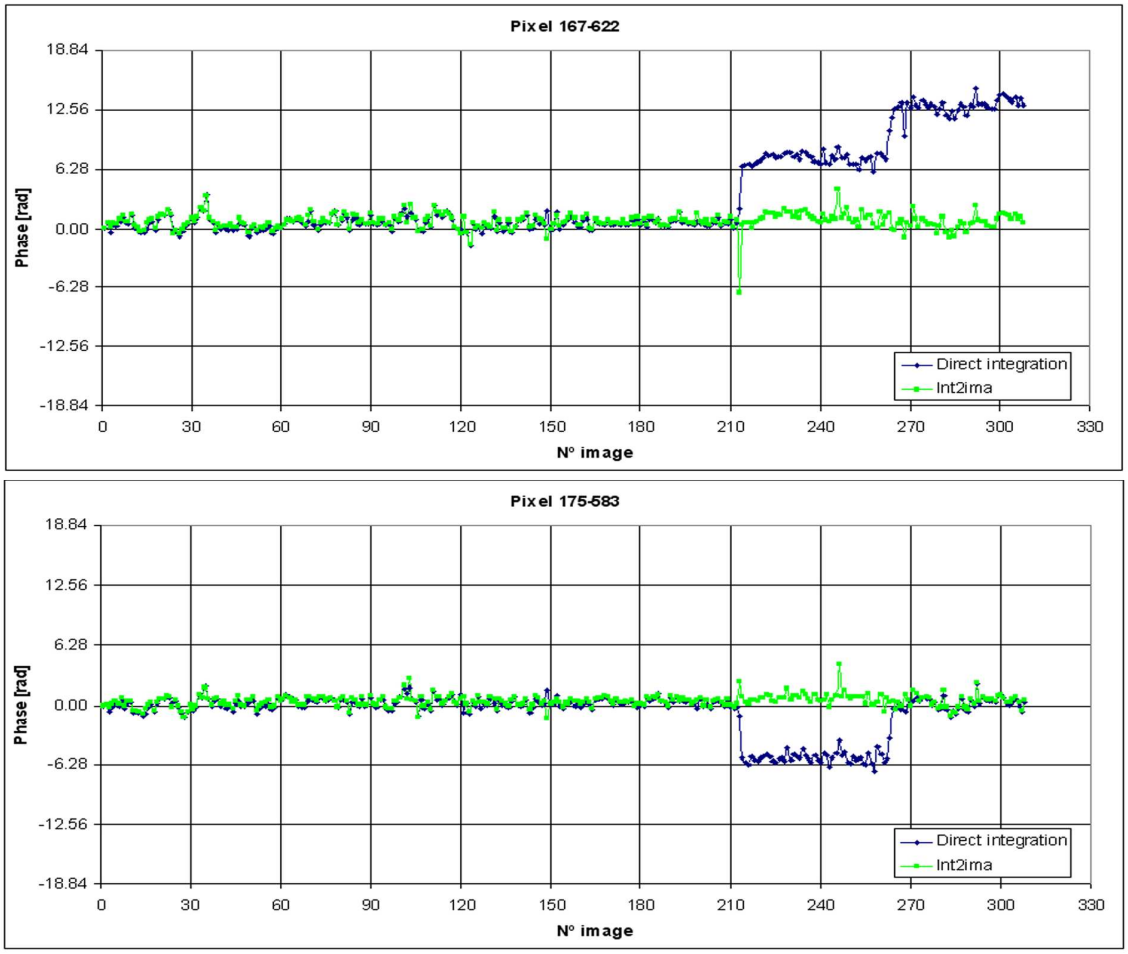

Figure 4.14: Comparison between the int2ima (green time series) and the direct integration results (blue time series). The time series come from stable points.

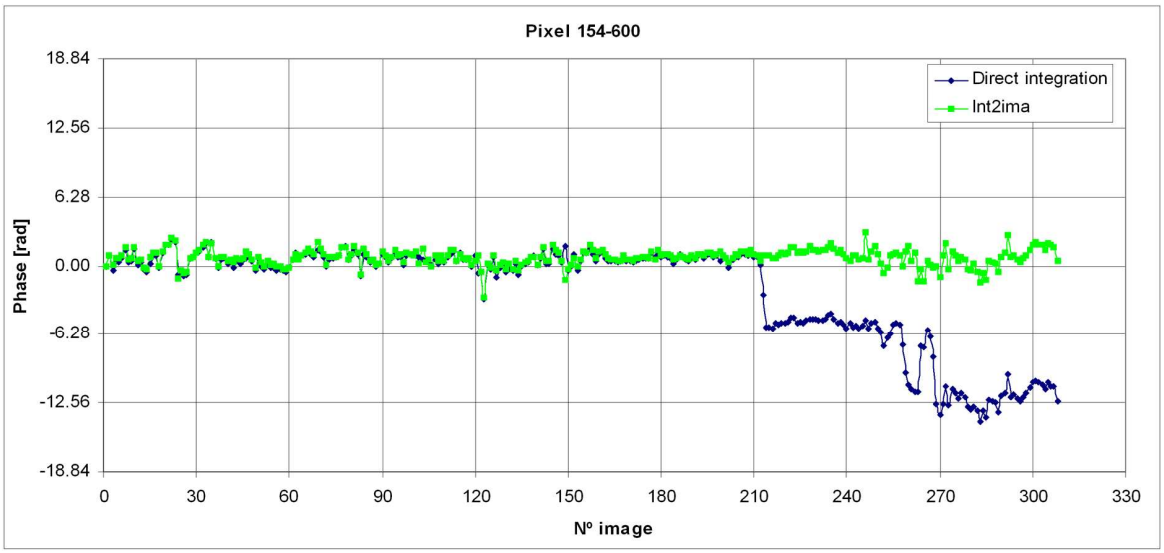

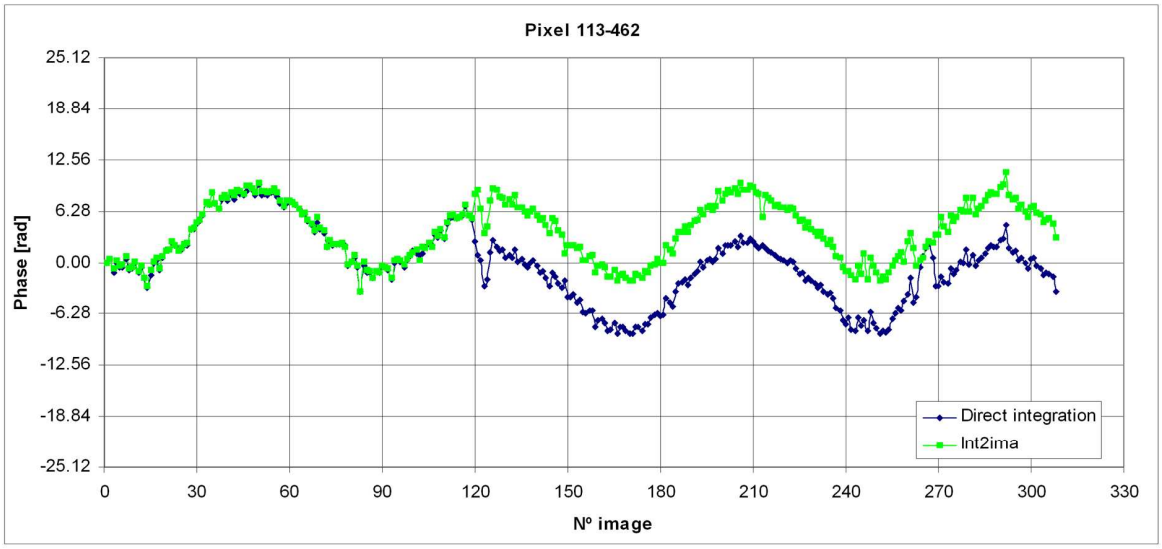

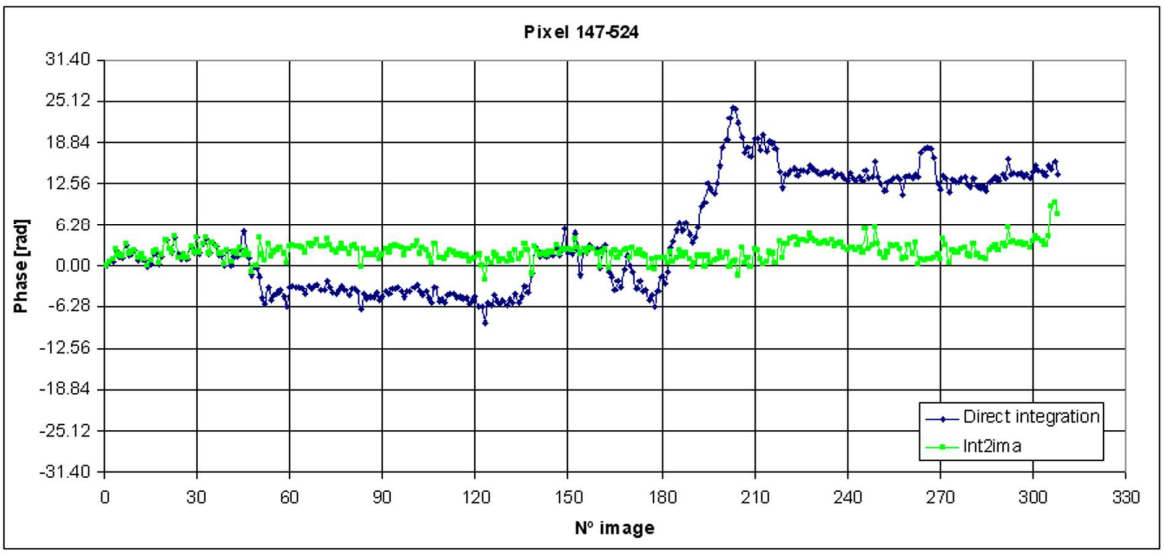

Figure 4.15: Deformation time series: comparison between the solution from int2ima and the direct integration.

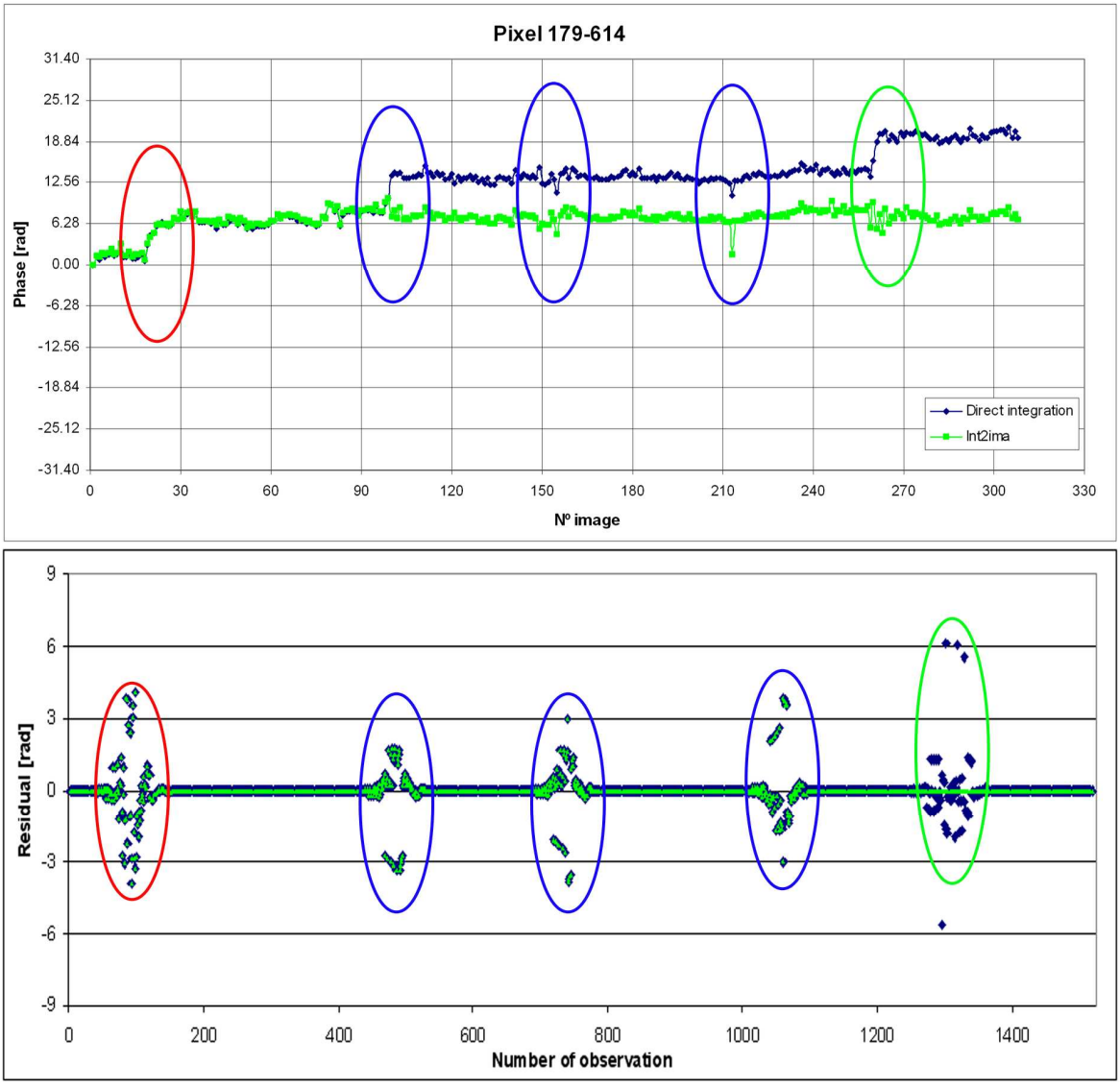

Figure 4.16: Int2ima residual analysis: Deformation time series from int2ima and the direct integration (above). In the plot below, observation residuals at the first iteration (in blue) and the last iteration (in green) for a given pixel.

Chapter 5

Non-interferometric GB-SAR for deformation measurement

This chapter presents a procedure for deformation monitoring, which uses a non-interferometric approach based on GB-SAR data. This approach is completely different from and complementary to the one described in Chapter 3. In fact, it does not exploit the information contained in the interferometric phase; rather, it exploits the geometric information of the GB-SAR amplitude images. This is achieved by using an image matching technique performed on the amplitude images acquired over the same scene in different times, and by adopting targets optimised to image matching purposes.

The chapter is organized in five main sections. The first one introduces the methodology, comparing it with the interferometric approach. In the second section the complete procedure is described, while in the third one are discussed two important topics: the characterization of the exploitable targets and the achievable precision. Section 5.4 is devoted to the description of some validation experiments performed in different environments, and finally the last section describes the results obtained in a real landslide case.

5.1. Introduction

In the previous chapters is described the use of GB-SAR interferometry to measure and monitor deformations. Two data acquisition modes are considered: the continuous and the discontinuous modes. The first one is usually adequate for monitoring crisis episodes, while the latter one is more appropriate to monitor slow or very slow displacement phenomena. This chapter is focused on a discontinuous approach, where the instrument is used to revisit the same site over time, similarly to what happens with satellite acquisitions.

As already commented earlier in this dissertation, the SAR interferometric technique requires two fundamental components. Firstly, it needs a coherent GB-SAR sensor, which measures both the phase and amplitude of the radar backscattered signal. Secondly, it needs repeated SAR acquisitions of the same scene over time, starting, at least, from two acquisitions. The eventual displacements of the observed scene occurred between two SAR acquisitions separated in time are derived by computing and analysing the interferometric phase. The major advantage of this approach is its high sensitivity to small displacements, which can be measured with a precision that is a fraction of the used SAR wavelength. Considering that the majority of the available GB-SAR systems work with wavelengths in the region of 1-5 cm, this implies, for good targets, millimetre or even sub-millimetre displacement precision. The main limitations of this approach are discussed below.

The conditio sine qua non for using SAR interferometry is that a sufficient number of targets remain coherent over the observation period, which can range from weeks to several months or years, especially for very slow deformation phenomena. The loss of coherence that SAR data may experience over time can be particularly severe over vegetated and forested areas, and over scenes that change continuously over time modifying their radar responses. A second critical limitation is aliasing. Due to the ambiguous nature of interferometric phase measurements, the displacement undergone by a given scene can only be correctly, say unambiguously, estimated if the relative displacements actually occurring between adjacent coherent targets cause an interferometric phase difference up to half phase cycle. In terms of displacements this condition imposes a very restrictive limit that ranges from about 4.5 mm up to about 15 mm respectively at Ku- and C-band. From the operational viewpoint, the risk of deriving ambiguous displacement estimates represents a very severe limitation of the technique.

A third limitation is related to atmospheric component of the interferometric phase, which is caused by heterogeneities of atmospheric parameters, at the time of SAR image acquisitions, during the propagation from the sensor to the target. The atmospheric effect may degrade the quality of the displacement estimation. In the worst cases, when strong atmospheric components are associated with spatially sparse coherent targets, it may even affect the phase unwrapping stage. The last main limitation is due to the mono-dimensional nature of the GB-SAR interferometric measurements, which returns displacements only along the LOS direction of the radar: out of the three possible components of a generic 3D displacement, GB-SAR interferometry can only provide this component of displacement, the LOS component.

The proposed non-interferometric procedure provides remarkable improvements with respect to all four above described limitations, as detailed in the next section.

5.2. Description of the procedure

The procedure takes full advantage of the GB-SAR imagery by jointly using two key components. An image matching technique is performed on the amplitude GB-SAR images, and special targets are employed, which are optimal for image matching purposes. A way to get good targets is by using artificial Corner Reflectors (CRs). However, this is in principle not strictly necessary, provided that a sufficient number of natural targets are already available to sample the phenomenon of interest. Keeping in mind that the natural reflectors can always complement the measurements based on CRs, in the following we assume that CRs are used.

Figure 5.1 illustrates the main concept of the procedure: two images of the same place are collected at different times (master and slave), then a common point is identified in both images (P and P') and finally, looking at subpixel level, the displacement vector (S_x, S_y) occurred during the measured period is estimated.

The core of the procedure is three-fold: (i) employing a GB-SAR in a discontinuous mode; (ii) using image matching procedures; and (iii) deploying CRs. It is worth emphasising that these three core components are, *per se*, well known and established techniques. The procedure consists on using them jointly and in an optimized way for displacement monitoring purposes, achieving interesting performances, as it is discussed later in this chapter.

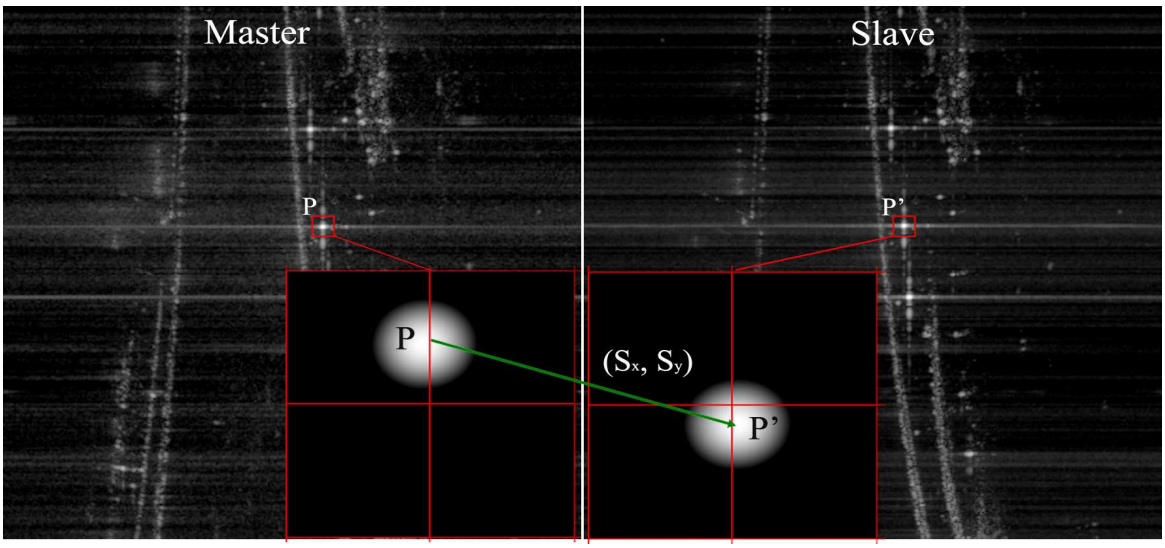

Figure 5.1: The key concept of the procedure is the image matching performed over special targets. The same point appears in the master (on the left) and the slave (on the right) images. Then, by means of a matching technique, which works at subpixel level, the displacement vector (Sx, Sy) is estimated.

This section describes the complete proposed procedure, which can be divided into the following steps:

- Data acquisition.
- Data pre-processing.
- Global matching.
- Estimation of the GB-SAR repositioning effects.
- Estimation of the pairs of displacements.
- Estimation of the displacement time series.

The block diagram of the entire procedure is shown in Figure 5.2. Each step is described in the following sections.

5.2.1. Data acquisition

The data acquisition is obtained through N in-situ campaigns. The followed procedure for each campaign consists on:

- Installing the GB-SAR instrument in a position to fully illuminate the area of interest (AoI). Usually the GB-SAR positioning (and re-positioning in the following campaigns) is performed in a relatively light fashion, e.g. without building a stable concrete base. This eases the data acquisition procedure. This can reduce the accuracy of the measurements but a check through coregistration is always carried out on site in order to check the quality of the repositioning.
- Deploying a set of M CRs in the AoI.
- Acquiring multiple images, obtaining a set of K complex SAR images. According to the author's experience, a set of 15 images is typically enough. These multiple images are used to reduce the effects on the amplitude images due to speckle and atmospheric effects.

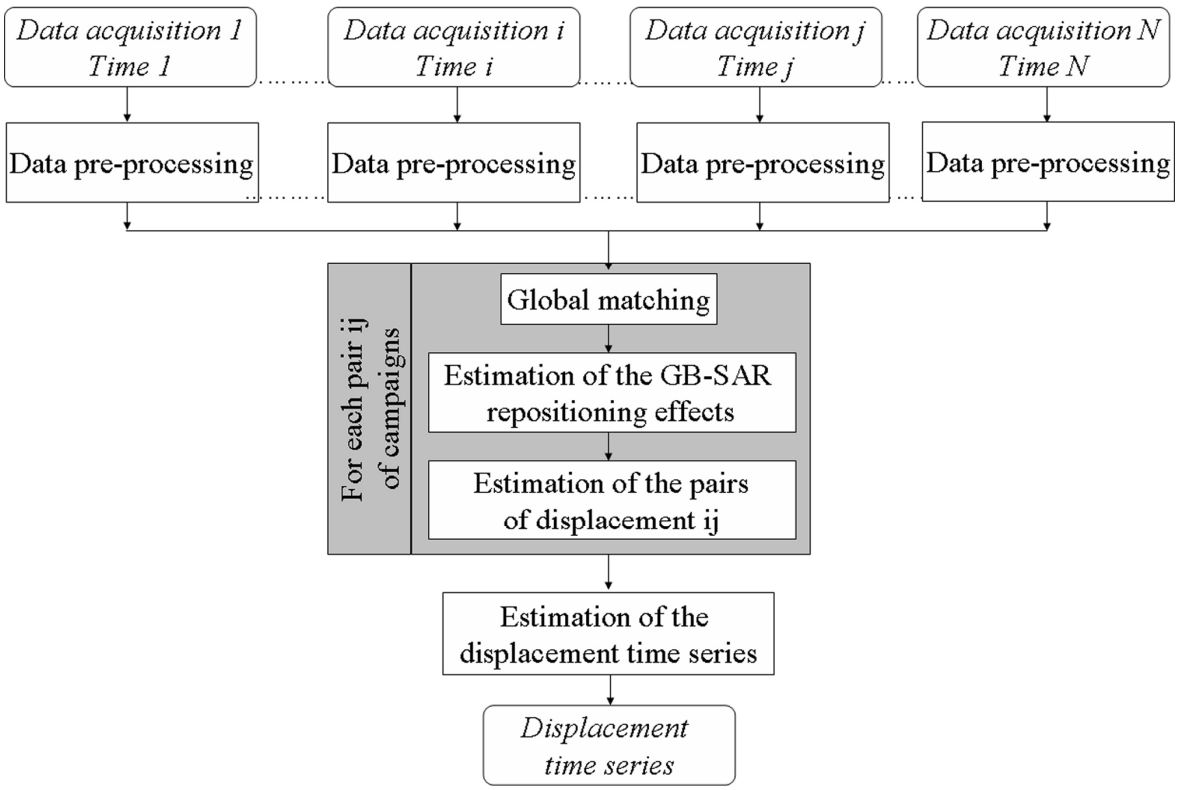

Figure 5.2: Block diagram of the complete GB-SAR non-interferometric procedure.

5.2.2. Data pre-processing

The data pre-processing is performed on each set of K complex SAR images acquired in a campaign, and hence is repeated up to N times. The algorithm is described in Figure 5.3. Firstly, it involves a check of the quality of each acquired complex SAR image. This check has the objective of detecting and eventually discarding images with problems, e.g. corrupted files, very noisy images, images characterised by blurred amplitude values, etc. The check is usually done visually. However, especially for large datasets the analysis of the amplitude statistics can ease this check.

On the sub-set of quality-proofed images, which includes $Q \leq K$ images, a temporal filtering is performed. The goal of the filtering is the enhancement of the SAR amplitude images by strongly reducing the so-called speckle effect. This is achieved through an incoherent temporal averaging of the Q images. The result of this operation is an incoherent mean SAR image A_{incoh}, which is obtained as follows:

$$A^k_{incoh}(i,j) = \frac{\sum_{i=0}^{Q} A^k_i(i,j)}{Q} \tag{5.1}$$

where k is the number of the campaign at hand, A_i is the amplitude value of the i-th acquisition of the campaign k, (i, j) is the column and line position of a generic pixel, and Q is the number of images.

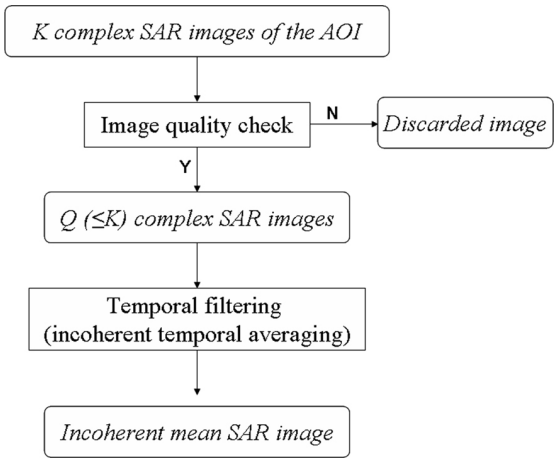

Figure 5.3: Data pre-processing procedure.

5.2.3. Global matching

The scheme of this step is shown in Figure 5.4. The global matching is performed on each analysed pair *ij* of campaigns. Given N campaigns, the minimum number of global matching is *N-1,* e.g. *12*, *23*, …, *ij*, ..., *(N-1)N.* The global matching involves:

- Getting, as input, a pair of incoherently averaged SAR images, say A^i_{incoh} and A^j_{incoh}. The first image is referred to as the master, while the second one is called slave.
- Performing a pixel selection, whose goal is identifying those pixels of the two images that can be exploited for the image matching purposes, excluding the other ones. The pixels to be selected include those associated with the M deployed CRs, and others related to "natural reflectors", like exposed rocks, buildings, man-made structures, metallic structures, etc. Different procedures can be used for this purpose, which usually are based on the amplitude images or on other statistics. The selection criterion used on this work will be discussed later in this chapter.
- Performing the global image matching over the set of pixels selected in the previous step. Several algorithms can be used for this purpose, see for example feature based matching (Förstner (1984)) or the least squares matching (Gruen (1985)). In Bamler and Eineder (2005) the achievable shift estimation accuracy of three different matching algorithms, the coherent speckle correlation, the incoherent cross-correlation and the split band interferometry is discussed. The results obtained on the present work were achieved by using the incoherent cross-correlation, which is based on the amplitude images.
- A further selection is then performed on the outcome of the global matching, i.e. W pairs of global shifts, usually expressed in pixels. Each pair containing one image shift (the shift needed to match a given slave pixel with its homologous on the master image) for each of the two main directions of the SAR images: the range direction, and the cross-range direction. The selection is performed on a score that measures the quality of the matching. It is usually related to the used image matching procedure. Examples of these score factors are the cross-correlation coefficient, the sigma naught of LS matching, or other indicators of the slave to master goodness-of-fit.
  The result of the global matching is finally a selected set of $R \leq W$ pairs of global shifts.

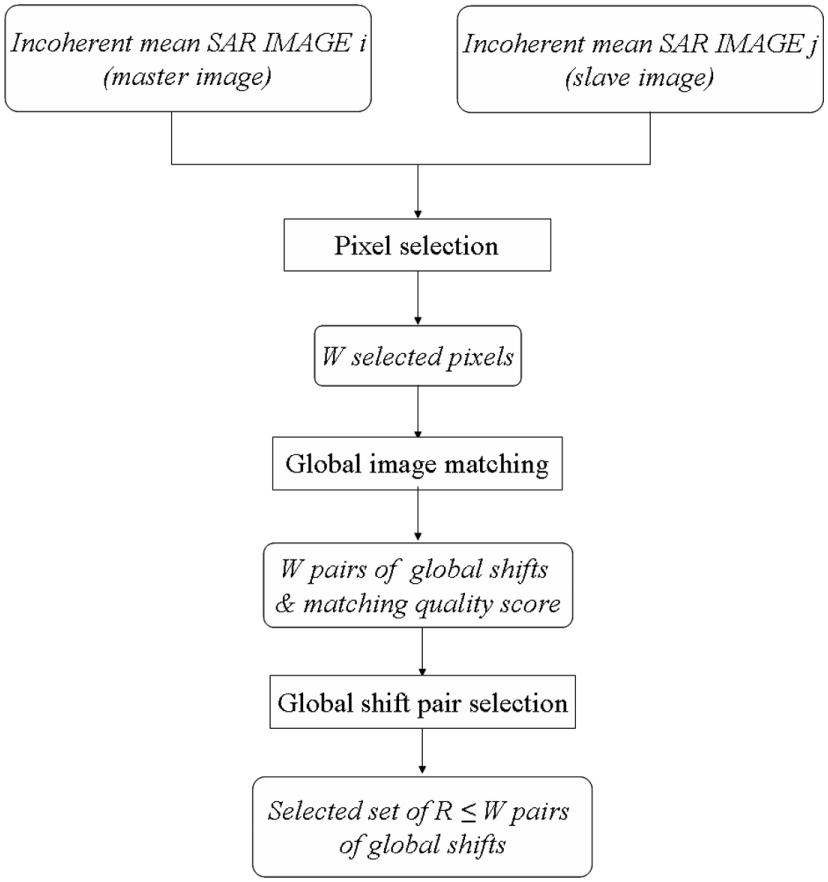

Figure 5.4: Global matching procedure performed for each pair of campaigns.

5.2.4. Estimation of the GB-SAR repositioning effects

Estimation of the GB-SAR-repositioning effects, like the global matching, is performed on each analysed pair *ij* of campaigns. These effects are due to the fact that there are slight changes in the position and orientation of the GB-SAR between different campaigns. The sequence of this step is shown in Figure 5.5. The estimation of these effects involves:

- Collecting external information on the stable areas located in the vicinity of the deformation AoI. This information is usually available if the deformation mechanism and the key characteristics of the deformation phenomenon at hand are known. In case this information is not available, one alternative way to get it is by analysing the set of R pairs of global shifts estimated in the previous step. If the information on the stable areas is known in the so-called object space, say a cartographic or geographic reference system, it has to be properly mapped in the SAR image space to be exploited. This operation, which requires as input the position and orientation of the GB-SAR, is the inverse of the geocoding operation described in Chapter 3. The output of this operation is a mask that identifies all stable areas in the SAR image space.
- By using the above mask, a subset of the R pairs of global shifts is computed, which is given by the $S \leq R$ global shifts that fall in the stable area mask.

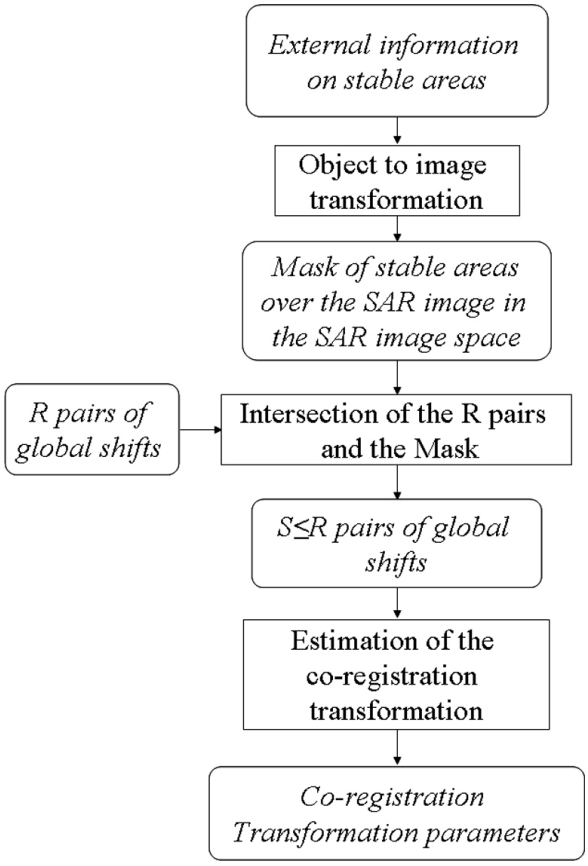

Figure 5.5: Estimation of the GB-SAR repositioning effect.

- The S global shifts are used to estimate the so-called coregistration transformation, i.e. the slave to master transformation which is due to the GB-SAR-repositioning effects. The complexity of the transformation mainly depends on the topography of the AoI and the distance AoI to the sensor. The author's experience suggests that, excluding close-range scenarios, e.g. located at less than 50-100 m, and strong topographic variations, the affine transformation, or any transformation with similar characteristics, is sufficient for this purpose. In our procedure the used transformation model is:

$$\left.\begin{aligned} x_S &= x_M + p_x(x,y) + \xi_x \\ y_S &= y_M + p_y(x,y) + \xi_y \end{aligned}\right\} \tag{5.2}$$

  where (x_S, y_S) are the image coordinates on the slave image of the point (x_M, y_M) of the master image, (ξ_x, ξ_y) are the residual errors on the estimation, and p_x, p_y are transformation functions whose parameters are the unknowns.
- The final result of this block is a set of transformation parameters modelling the GB-SAR-repositioning effects and used to perform the slave to master coregistration.

For the sake of completeness, it is worth mentioning that coregistration transformation parameters could, in principle, be estimated directly, by measuring accurately and in each campaign the position and orientation of the GB-SAR sensor.

5.2.5. Estimation of the pairs of displacements

The estimation of the pairs of displacements is performed on each analysed pair *ij* of campaigns. It involves:

- Subtracting the GB-SAR-repositioning effects, which are modelled by the coregistration transformation parameters, from the set of R pairs of global shifts. This results in R pairs of displacement shifts, where the displacements are relative displacements with respect to the whole set of stable areas mentioned above. As mentioned above, the R pairs of displacement shifts include those shifts associated with the M deployed CRs and others related to "natural reflectors" located in the AoI.
- Taking into account the GB-SAR image parameters the above displacement shifts are transformed in displacements. It is worth noting that in this step the displacements are still defined in the image space, which usually coincides with the SAR master image.
- Finally, considering the GB-SAR sensor parameters (GB-SAR position, orientation, etc.), the image geocoding is performed. This involves the image to object transformation described in Chapter 3. The final result is a set of R pairs of estimated displacements, which have a position defined in the object space, say in a cartographic or geographic coordinate reference system.

5.2.6. Estimation of the displacement time series

The estimation of the displacement time series has to be run once for all campaigns, to get the main product of the whole procedure, i.e. the estimated displacement time series. It involves:

- Getting, for each analysed pair *ij* of campaigns, a set of R_{ij} pairs of estimated displacements defined in the object space. Note that the sets R_{ij} are usually different. For this reason, the common set has to be identified by getting the intersection of all R_{ij} sets. From each pair *ij* of campaigns a new subset is defined: T_{ij}.
- If the minimum number of campaign pairs has been analysed, the displacement time series can be computed by direct integration of the T_{ij} pairs of estimated displacements. By contrast, if a redundant configuration is used, the displacement time series are estimated through a LS estimation procedure. In this case, the observation equation is:

$$\begin{cases} T_{ij} = T_j - T_i + \varepsilon \\ T_0 = 0 \end{cases} \tag{5.3}$$

  where T_o is set to 0, T_i and T_j are the unknowns and represent the accumulated displacement at time (i) and time (j) and ε are the residuals.
- The redundant configuration offers the advantage of having a certain degree of controllability of the displacements. In particular, the LS estimation can be analysed in order to identify and isolate outliers in the input data, i.e. the T_{ij} pairs of estimated displacements. This process can be iterative.

The final product is provided by the final LS solution: a set of T estimated displacement time series, defined in the object space, say in a cartographic or geographic coordinate reference system.

5.3. Advantages against the interferometric approach

The proposed procedure offers remarkable advantages with respect to GB-SAR interferometry, overcoming the important limitations addressed in Section 5.1. The main advantages of the non-interferometric approach with respect to the interferometric one are:

- It provides non-ambiguous, aliasing-free, displacement estimates. This is, by far, the most important advantage of the proposed procedure.
- The displacement estimates are not affected by the atmospheric effects.
- It provides 2D displacement measurements, in range and cross-range directions. This represents an improvement with respect to the LOS estimates coming from SAR interferometry. It is worth emphasising that the performances of the 2D estimations depend on the geometric characteristics of the used GBSAR imagery. In general, worse performances are expected in the cross-range direction, especially in the middle and far range of images, where spatial resolution is degraded.

In addition, by employing CRs, precise and reliable displacement estimates can be achieved. It is important to note that here we estimate the displacements over single targets, while usually SAR amplitude matching is usually employed for coregistration purposes, where hundreds of points are used to estimate a limited set of parameters (usually less than 10 for the entire image). Here we need to rely on the two displacements (shifts) per each measured target: in this context CRs are fundamental.

Finally the CRs guarantee the possibility to measure the same targets over time. Note that a similar effect can be achieved by using CRs in GBSAR interferometry.

5.4. Discussion of the proposed method

This section discusses in detail two fundamental technical aspects of the proposed non-interferometric GB-SAR procedure: the selection of the pixels that guarantee good deformation estimates, and the need of deploying CRs. Given two images acquired at different times, the proposed procedure provides a set of R pairs of estimated displacements occurred in the time interval between the master and slave acquisitions. The R points have to be previously selected considering their reflectivity with respect to their neighbours. A possible selection criterion is suggested by the diagram in Figure 5.6, which shows the theoretical relation between the estimated matching shift errors (hereafter named matching precision) and the signal-to-clutter ratio, i.e. a measurement of the intensity of a point scatter with respect to its neighbours located in a given window (Bamler and Eineder, 2004). Provided that this relation is based on theoretical results, the actual suitability of the signal-to-clutter ratio as pixel selection criterion was assessed by using real data.

For this purpose, three experiments were devoted to explore the relation between the matching precision and an estimation of the signal-to-clutter ratio using real data, which from now on is called peak to background ratio. The sequence of the experiments was basically the same, while the difference between them is due to the type of test site and the sensor to target distance. It was assumed that for the three sites the measured area remained stable during the measurements. The sequence of the three experiments was:

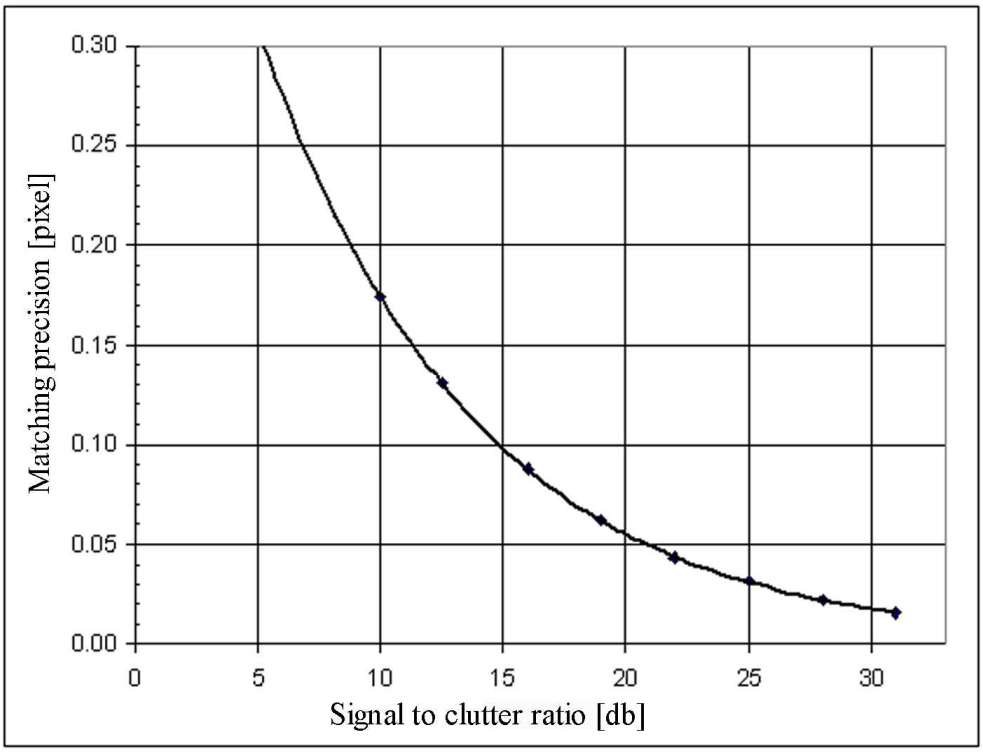

Figure 5.6: Matching precision of a point scatter as a function of the peak to background ratio, from Bamler and Eineder (2004).

- GB-SAR positioning;
- Acquiring a set of 15 images;
- Dismounting and re-mounting the GB-SAR;
- Acquiring a second set of 15 images;
- Applying the deformation estimation procedure over selected targets;
- Analysis of the estimates, considering that zero displacements were expected.

The three experiments were performed in three different scenarios, see Figure 5.7: the Cal Ganxo (Castelldefels) experiment was on an urban scenario, with maximum distance of 2.5 km; the Vallcebre, Catalan Pyrenees, experiment was performed in a mountainous environment, where the main part of the scene is vegetated, and with a maximum distance of 1.6 km; finally the Canal Olímpic (Castelldefels) was carried out in a flat area, with maximum distance of 1 km, and with a water channel between the area of interest and the sensor. These experiments were performed without considering data coming from artificial corner reflectors.

Considering the three experiments, the total amount of measured deformation pairs was 60247. Figures 5.8 and 5.9 show the plots of the matching precision in range and cross-range, respectively, with respect to pick to background ratio. The blue line represents the reference theoretical values, while the other lines represent the experimental results. The original results were analysed after applying some filtering: (1) points with correlation below 0.6 were discarded; (2) short range points, below 100 m, were excluded to avoid focusing distortions; and (3) points with estimated shifts bigger than 1 pixel were considered outliers and discarded. The last constraint only affected the statistics of points with low peak to background ratio, because none of the estimated shifts over points with a

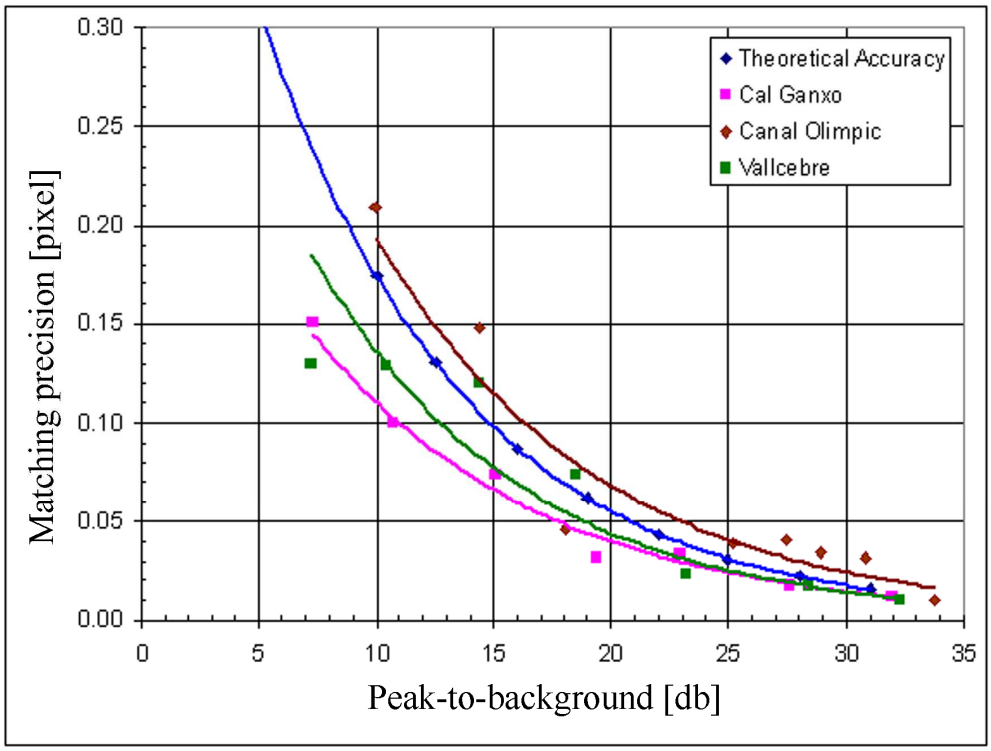

Figure 5.8: Theoretical and experimental matching precision in range as a function of the peak to background ratio.

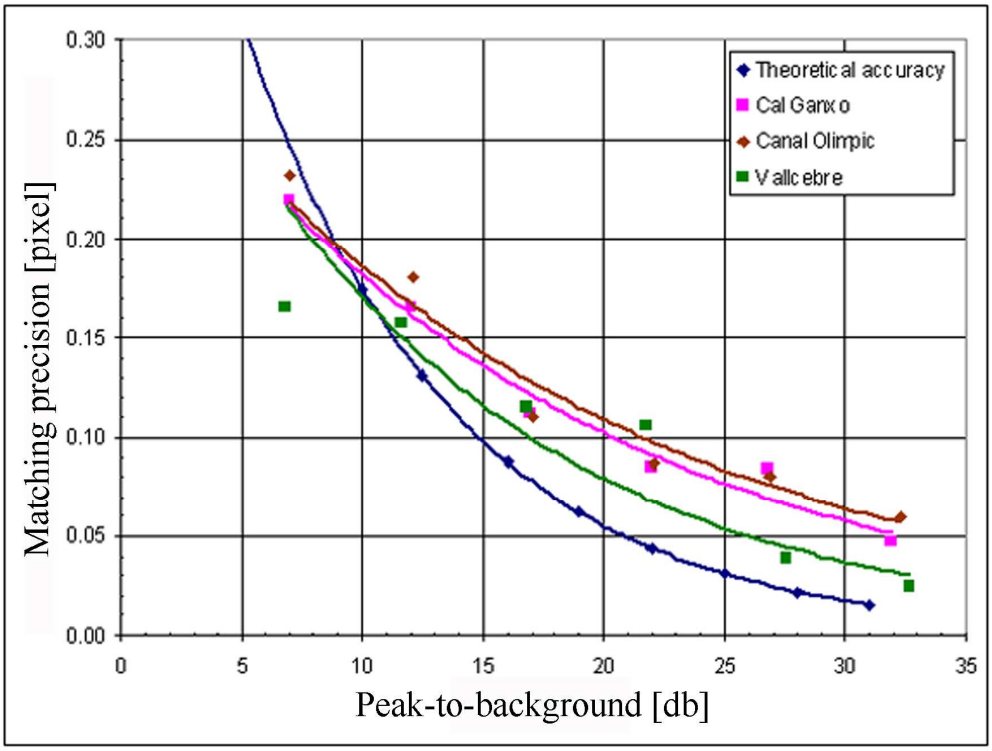

Figure 5.9: Theoretical and experimental matching precision in cross-range as a function of the peak to background ratio.

high peak to background were above one pixel. Two main conclusions can be derived:

- In range direction the experimental results agree very well with the theoretical ones (Figure 5.8). A matching precision of about 0.02 pixels, which corresponds to 1 cm for IBIS-L system at maximum range resolution of 50 cm, can be achieved by selecting points with pick to background ratios bigger than 30 db.
- The results in cross-range are notably worse, see Figure 5.9. In the best case, assuming reflectors with pick to background bigger than 30 db, the matching precision ranges from 0.02 to 0.07 pixels, which for the IBIS-L in terms of displacements correspond to 1 to 3 cm at 100 m, and to 10 to 30 cm at 1000 m. The decrease of the precision in the cross-range direction can be due to the fact that the cross-range resolution is obtained by averaging all the measurements collected by the radar during its movement along the rail. It makes the cross-range direction more sensitive to changes in the scene during the acquisition.

In addition, one may notice that the results on the Canal Olímpic are worse than the other two experiments. A possible explanation of this decrease on the precision can be due to the characteristics of the measured area which is too flat and it has calm water between the GB-SAR sensor and the main body. It is possible that in the statistics a lot of points within the water were treated as a good point due to double bound effects. However, in the range direction the results are still acceptable, e.g. a precision of 0.03 pixels, or 1.5 cm at 31 db were achieved.

5.4.1. Role of corner reflectors

The results of the three experiments made evident a critical point of the procedure: the low number of targets with a sufficient pick to background ratio to guarantee good deformation estimates. For the Cal Ganxo experiment, which includes an urban area, the number of points with pick to background bigger than 30 db is 73: this corresponds to the 0.32% of the total number of measured pairs. Similar values were obtained in the Vallcebre experiment, where the percentage of "good points" is 0.27%, and in the Canal Olímpic experiment, with 0.28%. In the Vallcebre test site, which concerns an active landslide, there is no "good points" in the movement area. In general, such percentages are largely insufficient to get an appropriate spatial sampling of a given deformation phenomenon. These results clearly demonstrate the need of deploying artificial corner reflectors, to ensure getting good deformation measurements. As already discussed in Chapter 2, this implies a remarkable change, from "pure remote sensing" to a "hybrid remote sensing supported by in-situ installed CRs".

Different types of CRs were developed and tested at the Institute of Geomatics with two-fold objectives: getting good matching performances (i.e. high pick to background ratio) and an accurate repositioning of the CRs in different campaigns. In particular, the objective was to ensure a millimetric repositioning and a pick to background ratio of at least 30 db. Some tests were performed on different types of CRs, trying to find the best compromise between signal characteristics, repeatability over time, size and portability of the CRs. Figure 5.10 shows two types of CRs. The most advanced type, which can be oriented at different angles, can be used for both Ku-band GB-SAR and X-band satellite data. It is worth noting that the capability of reaching 30 db is strongly dependent on the combination of the size of the CR and the sensor-CR distance.

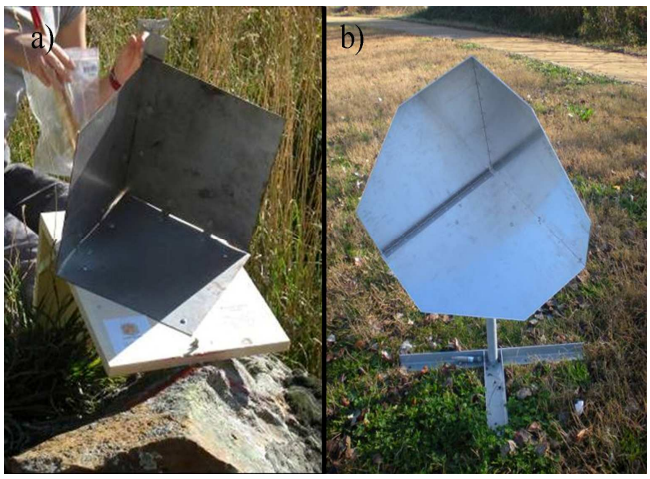

Figure 5.10: Two types of CRs developed and tested at the Institute of Geomatics.

5.5. Validation results

In this section are described some experiments made to validate the proposed non-interferometric GB-SAR procedure. Four experiments were carried out, all of them based on artificially induced deformations, which were simulated by displacing a set of CRs. The main objectives of these experiments were validating the new deformation monitoring technique, testing different types of CRs, and checking the dependence of validation errors on distance or on the magnitude of displacements. The experiments were performed using four different scenarios. The Campus experiments (I and II) were the first one, where the potentialities of the technique were evaluated. In these experiments the mean distance between the CRs and the sensor was around 150 m, the used CRs were those shown in Figure 5.10a, and the displacements were simulated both in in range and in cross-range. The Cal Ganxo experiment was performed to obtain results at a relatively far distance, around 1600 m. Finally, the Beach experiment was used to test different types of CRs. The sequence of the experiments was:

- Positioning the GB-SAR;
- Deploying the CRs in the observed scene;
- Acquiring a set of 15 images;
- Dismounting and re-mounting the GB-SAR, simulating the discontinuous mode;
- Applying different know displacements (reference values) to each CR;
- Acquiring a new set of 15 images;
- Estimating the displacements using the proposed procedure;
- Comparing the estimates displacements with the reference displacements.

It is worth noting, that only the CRs were moved, instead of the whole object, as it is on the real case. In Table 5.1 are shown the results obtained in the Campus experiments (I) and (II). For some of the CRs deployed in this experiments were simulated displacements in both range and cross-range directions. Table 5.2 shows the results of the Cal Ganxo and the Beach experiments, where only range displacements were simulated.

Let's consider the cross-range error column from Table 5.1, and in particular the 9 CRs with peak to background ratio greater than 30 db, which are highlighted by circles: the blue circles indicate the 5 CRs which were moved in cross-range, while the yellow ones

show those that remained stable during the experiment. Most of the cross-range errors were of the order of several centimetres. Considering the sensor to CR distances (all of them below 180 m), the errors are slightly worst than the expected ones according to the analysis discussed in Section 5.4. The interpretation of these results is two-fold. From one side, the cross-range performance is significantly under the expected one, which, roughly speaking was around 1 cm). For this reason, after these two experiments it was decided to focus our activities on improving and consolidating the results in the range direction, which from the beginning proved to offer better performances. On the other hand, the above results were considered useful to show the 2D capability of the proposed technique to measure displacements. Further works are needed to understand and improve the cross-range results. From now on the discussion of the results is focused on the range direction.

The range analysis was performed considering the four experiments. The total number of measured CRs was 37. The estimated validation errors are given by the difference between the GB-SAR estimates of displacements and the reference values. Most of the validation errors, 25 out of 37, are below 1 cm, five errors are between 1 and 2 cm, and finally seven errors are bigger than 2 cm. The latter ones can be considered outliers. These errors are analysed below.

If we consider only the 21 CRs with peak to background ratio bigger than 30 db, all of them but one have validation errors below 1 cm, see the range Tables 5.1 and 5.2. In this case, the outlier is explained by the distribution of the CRs on the scene: the CR with wrong estimation was affected by the side lobes of another CR, which was moved in a different way. A different representation of the results shown in Tables 5.1 and 5.2 is given by the plot (a) of Figure 5.11. The plot shows the relation between the errors and the peak to background ratio: the error dispersion increases with the decrease of the peak to background. Note that the outliers have been removed to better visualize the results.

For the Beach experiment, see Table 5.2, CRs with three different sizes were used. In this case the smaller ones, trihedral CRs with 20-cm edges, were deployed in the close range (from 223 m to 230 m), the medium ones, with 50-cm edge, at a medium distance (from 575 m to 597 m), and the bigger ones (up to 70 cm of edge) on the far range (from 963 m to 1080 m). As can be observed in Table 5.2, there are not significant differences on the results. This occurs because the size of the CRs was correctly modulated by the sensor to CR distance. It can be observed also that the CR with lower peak to background corresponds to one of the big CRs: in this case the reason is probably the not optimal orientation of the CR with respect to the radar.

Two more interesting results of these experiments are illustrated by the plots (b) and (c) of Figure 5.11. The plot (b) displays the errors versus the sensor to CR distance: there is not an evident relation between these two parameters. One may conclude that the quality on the deformation measurements is not distance dependent. However, it is worth noting that in this case, the real constraint is given by the peak to background threshold. In fact, the increase of the sensor-target distance makes more difficult finding natural "good" reflectors", and requires an increase of the CR size.

Finally, the plot (c) of the Figure 5.11 shows the relation between the errors and the magnitude of the displacements. This plot shows that the error magnitude is independent of the measured displacement, i.e. the accuracy of the method is not dependent on the magnitude of the measured displacement. It must be underlined that this represents a remarkable step forward with respect to the interferometric approach which is strongly dependent on the displacement magnitude due to the wrapped nature of the phases.

	CR Nº	Dist range [m]	Reference Range displacement [cm]	Estimated Range displacement [cm]	Reference Cross-Range displacement [cm]	Estimated Cross-Range displacement [cm]	Range Error [cm]	Cross-Range Error [cm]	Peak-to-background [db]
Campus Experiment	2	64.5	-1.00	-1.55	-1.00	-0.88	*0.55*	*-0.12*	**31**
	10	70.0	-5.00	-5.45	-5.00	-8.65	*0.45*	*3.65*	**31**
	3	80.0	-10.00	-10.95	-10.00	-16.51	*0.95*	*6.51*	**30**
	4	119.5	-10.00	-18.75	0.00	0.00	*8.75*	*0.00*	**20**
	5	127.0	-15.00	-16.40	0.00	0.00	*1.40*	*0.00*	**28**
	9	131.5	-20.00	-7.00	0.00	-7.23	*-13.00*	*7.23*	**28**
	8	133.5	0.00	0.00	0.00	0.00	*0.00*	*0.00*	**27**
	1	211.5	-20.00	-6.25	0.00	-17.50	*-13.75*	*17.50*	**21**
	6	220.0	0.00	-0.75	0.00	0.00	*0.75*	*0.00*	**26**
Campus Experiment (II)	2	79.5	-12.00	-12.50	-14.00	-18.05	*0.50*	*4.05*	32
	1	80.0	0.00	0.00	0.00	-1.20	*0.00*	*1.20*	34
	3	91.0	-20.00	-20.30	-20.00	-23.39	*0.30*	*3.39*	16
	4	110.5	-80.00	-79.70	0.00	-1.66	*-0.30*	*1.66*	29
	5	134.0	0.00	0.00	0.00	0.00	*0.00*	*0.00*	34
	6	167.5	30.00	28.10	0.00	-5.03	*1.90*	*5.03*	27
	11	179.5	15.00	15.60	-40.00	-46.13	*-0.60*	*6.13*	32
	10	194.0	-40.00	-39.05	0.00	-2.91	*-0.95*	*2.91*	31
	7	201.0	0.00	0.00	0.00	-9.14	*0.00*	*9.14*	32
	9	215.0	0.00	0.00	0.00	-9.78	*0.00*	*9.78*	29
	8	232.5	35.00	34.40	0.00	3.49	*0.60*	*-3.49*	27

Table 5.1: Validation results of two simulated experiments made in the IG Campus. The results of the two experiments correspond to the same scenario, but changing the displacement magnitudes and simulating movements in range and cross-range directions. In the range error column, the circles underline the worst results. The orange one indicates an outlier with relative high peak to background, while the two green circles show big errors with small peak to background. The yellow circles of the cross-range error column indicates CRs with peak to background bigger than 30 that remained stable during the experiment, while the blue ones represent those which were displaced in cross-range.

	CR Nº	Dist range [m]	Reference Range displacement [cm]	Estimated Range displacement [cm]	Error [cm]	Peak-to-background [db]
Beach Experiment	Small 1	223.0	26	25.78	*0.32*	33
	Small 2	239.0	9	9.38	*-0.38*	34
	Small 3	230.0	-20	-20.31	*0.21*	31
	Small 4	230.0	-17	-18.75	*1.45*	26
	Medium 1	575.0	18	18.75	*-0.75*	35
	Medium 2	597.0	29	28.13	*0.68*	30
	Big 1	963.5	-19	-19.50	*0.40*	32
	Big 2	1038.5	19	20.31	*-1.11*	32
	Big 3	*1035.5*	*-31*	*-14.06*	*-16.74*	*32*
	Big 4	1080.0	24	21.90	*1.60*	21
Cal Ganxo	1	1521.0	-15	1.55	*-16.55*	26
	2	1503.5	15	10.00	*5.00*	27
	3	1530.5	-15	-60.00	*45.00*	21
	4	1556.5	-31	-30.00	*-0.60*	35
	5	1573.0	23	23.45	*-0.95*	34
	6	1603.5	-27	-26.55	*-0.45*	33
	7	1657.5	-15	-14.05	*-0.65*	35

Table 5.2: Validation results of the Beach and Cal Ganxo simulated experiments. The experiments cover the range of distances from 223 m up to 1.6 km. The circles highlight the worst results. The red circle is an outlier with peak to background bigger than 30 db; the orange one is an outlier with relative high peak to background but with big errors, while the green circle show big error with small peak to background.

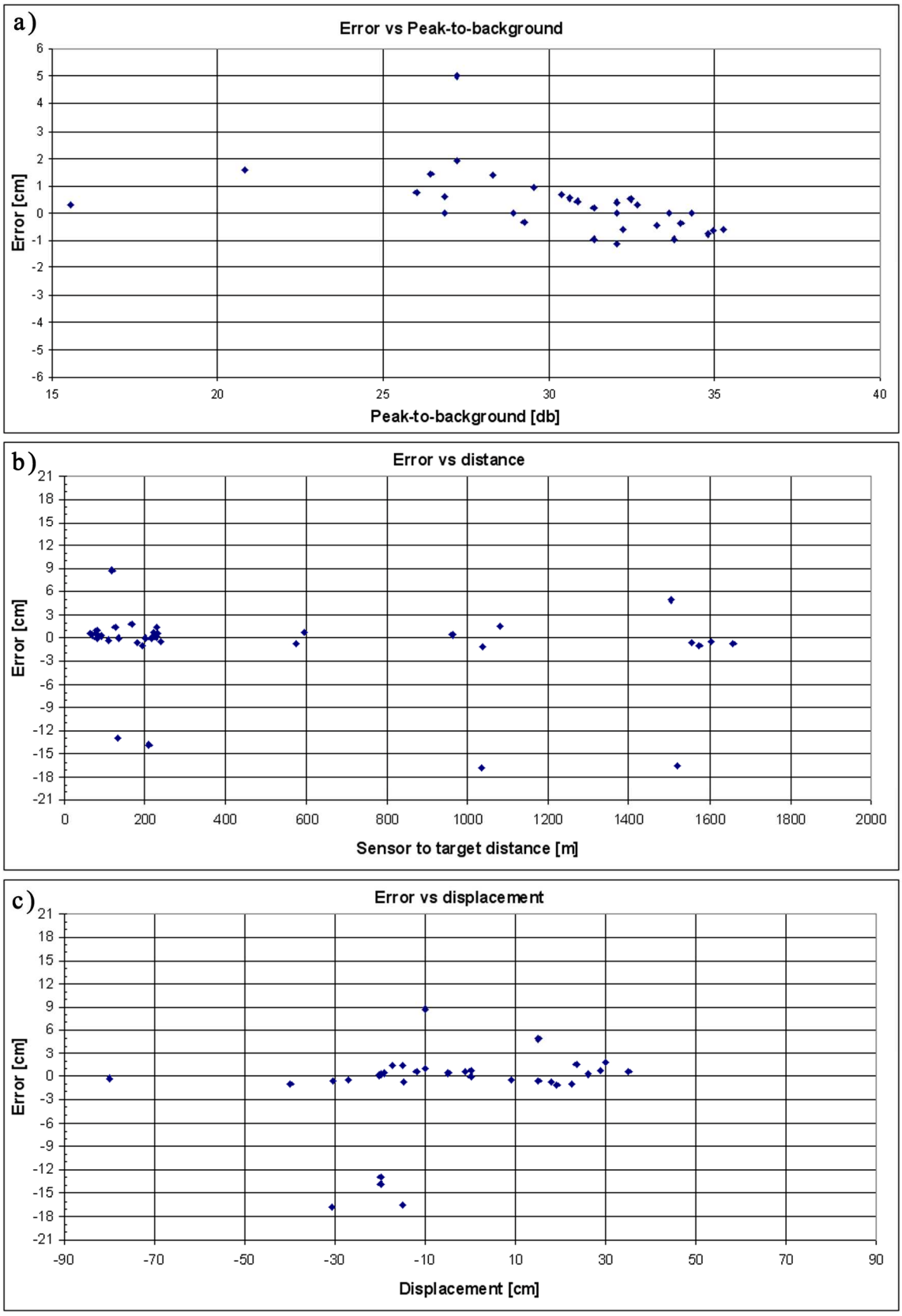

Figure 5.11: Analysis of the validation errors: plot of errors vs. peak to background ratio, peak to background (a); plot of errors vs. sensor to target distance (b); and plot of errors vs. displacement magnitude (c).

5.6. A real case study: Vallcebre test site

This section describes the results obtained on a real case study, the Vallcebre landslide, located in the Catalan Pyrenees. It is an active landslide which on the last three decades has been used, mainly by the Polytechnic University of Catalonia, as a natural laboratory to evaluate different monitoring techniques like total station, GPS, inclinometers, piezometry, extensometers, photogrammetry and satellite radar interferometry. The landslide is located in a rural area: it consists basically of vegetated areas, with a reduced number of isolated rural houses, which can act as natural reflectors.

The landslide was monitored using the non-interferometric GB-SAR approach from February 2010 to September 2011, carrying out eight campaigns. Figure 5.12 shows a photo of the measured area: the area bounded by the red line is the most active part of the landslide. The red dots represent the eleven CRs deployed in the moving area, while the four green ones represent the reference CRs, which were assumed to be stable. The green CRs together with other natural reflectors were used to estimate the repositioning effects.

In parallel to the GB-SAR measurements, five topographic campaigns were carried out in order to validate the results obtained with the GB-SAR. The topographic measurements were done approximately from the same viewpoint of the GB-SAR and considering only the distance. This was done in order to ensure a millimetric precision, which was needed to validate the GB-SAR displacements and in order to make easier the validation analysis. The GB-SAR and topographic results were both in LOS. It was not possible to re-install all the CRs in all campaigns, due to the vegetation changes and the water level raise in a portion of the AoI.

For the first four campaigns the CRs shown in Figure 5.10a were used. These are “first generation CRs”, which allowed us to make a light repositioning by simply marking with paint over stones the position of each CR. However, the repositioning was an important source of error, which limited the analysis: the repositioning errors were of the same order of magnitude of the precision of the procedure. In addition, due to the target-sensor distance, with these CRs was not possible to get measurements with pick to background ratio greater than 30 db. Table 5.3 shows the validation results based on the first generation CRs. Despite the relatively low pick to background ratio, half of the measurements has errors of about 1 cm or less, while the other half has errors above 2 cm. It is worth noting that these errors could be caused by both matching errors and repositioning of the CRs.

In order to avoid the uncertainty of the repositioning and to improve the pick to background a new generation of CRs was used, see Figure 5.10b. The new CRs have a larger size and allow the repositioning to be realized by fixing mechanically the base of the CR to the terrain (e.g. rocks). The CR bases remained in situ between campaigns: only the CR heads were removed at each campaign. This allowed us to improve noticeably the precision on the repositioning. Another improvement was the pick to background which, as it is shown in Table 5.3, has notably increased: for the last four campaigns the pick to background ratio was greater than 30 db for all CRs. The validation results with the new CRs show that all the measurements but one have errors below 1 cm. There is only one outlier (see CR9 on the measurement 11/2010 - 01/2011): even though its reason is not very clear, it could be due to an error on the CR repositioning. The results again confirm

the measurement performances of the proposed technique, which were discussed in the previous section.

Figure 5.13 shows an aerial photo of the measured area with the total displacement vectors for those CRs with reliable results for the whole period, while Figure 5.14 shows the corresponding temporal series. The measurement covers the period from February 2010 to September 2011. The maximum measured displacement is about 80 cm and corresponds to the CR 12. The temporal series show that the movements are mainly linear in time. However, one may notice a deceleration of the displacements between July 2010 and January 2011, followed by an increase of the activity. It is worth noting that the displacement vectors are drawn in the LOS direction. These vectors must be projected on the terrain by taking into account the slope and aspect of the landslide. This could help in interpreting some results, e.g. the fact that CRs located on the foot of the landslide (CR10 , CR11 and CR8), which is supposed to be the most active part of the landslide, are the slowest points.

Figure 5.12: Vallcebre test site. The green points represent the stable CRs while the red ones represent the CR deployed on the area of movement.

	CR	Dist range [m]	Topographic measurement [pix]	Estimated Shift Range [pix]	Error [pix]	Error [cm]	Peak-to-background [db]
Small CR's 07/2010-09/2010	3	532.0	-0.08	-0.14	*0.06*	*2.83*	27
	4	523.5	-0.09	-0.11	*0.02*	*1.17*	20
	5	546.0	-0.08	-0.13	*0.05*	*2.35*	21
	6	600.5	-0.08	-0.19	*0.11*	*5.48*	24
	7	619.5	-0.09	-0.11	*0.02*	*1.07*	21
	8	526.5	-0.07	-0.06	*-0.01*	*-0.38*	20
	10	441.0	-0.04	-0.09	*0.05*	*2.49*	21
	12	530.5	-0.09	-0.09	*0.01*	*0.29*	27
	14	524.5	0.01	0.02	*-0.01*	*-0.48*	14
New CR's 11/2010-01/2011	CR01	507.0	0.07	0.10	*-0.03*	*-1.26*	34
	CR03	533.0	0.08	0.08	*0.00*	*0.03*	33
	CR05	543.5	0.08	0.05	*0.03*	*1.49*	31
	CR06	600.0	0.08	0.07	*0.01*	*0.51*	33
	CR09	445.5	0.09	0.19	*-0.10*	*-4.94*	33
	CR10	440.5	0.07	0.07	*0.01*	*0.31*	32
	CR11	482.0	0.09	0.10	*-0.01*	*-0.66*	35
	CR12	530.5	0.10	0.10	*0.00*	*0.04*	33
	CR14	523.5	-0.01	0.01	*-0.01*	*-0.67*	34
	CR15	707.5	-0.01	0.01	*-0.02*	*-0.87*	33
	CR16	466.5	0.00	-0.01	*0.01*	*0.47*	34
	CR17	832.5	0.05	0.05	*-0.01*	*-0.31*	30
New CR's 01/2011-04/2011	CR01	507.0	-0.20	-0.18	*-0.02*	*-0.88*	34
	CR03	533.0	-0.21	-0.20	*-0.01*	*-0.57*	34
	CR05	544.0	-0.21	-0.20	*-0.01*	*-0.57*	34
	CR06	600.0	-0.18	-0.19	*0.01*	*0.65*	35
	CR09	445.5	-0.17	-0.18	*0.01*	*0.36*	34
	CR10	440.5	-0.16	-0.14	*-0.02*	*-0.86*	34
	CR11	482.5	-0.20	-0.21	*0.01*	*0.52*	35
	CR12	530.5	-0.23	-0.22	*0.00*	*-0.20*	34
	CR14	524.0	0.01	0.02	*0.00*	*-0.18*	34
	CR15	707.5	0.02	0.00	*0.01*	*0.70*	36
	CR16	466.5	0.02	0.00	*0.02*	*0.80*	34
	CR17	832.5	-0.04	-0.02	*-0.01*	*-0.75*	31

Table 5.3: Validation results for three measurements on Vallcebre test site. The first campaign refers to the results obtained with the small, "first generation CRs", while the other two have been obtained with the new one. It is observed an improvement on the accuracy with the new CR network. This is correlated with the increase of the pick to background of the new CRs.

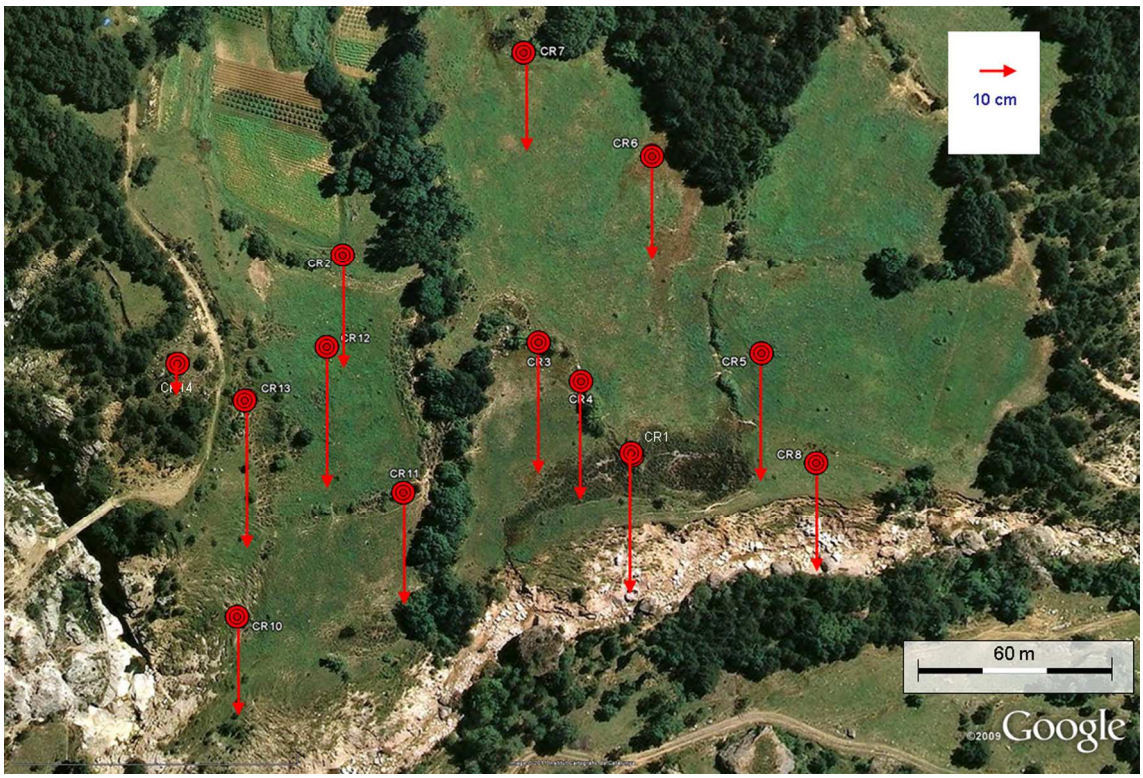

Figure 5.13: Vallcebre test site: LOS displacement estimated with the non-interferometric approach for 13 CRs. The period of measurement is February 2010 to September 2011. The maximum measured displacement corresponds to the CR12 with 37 cm.

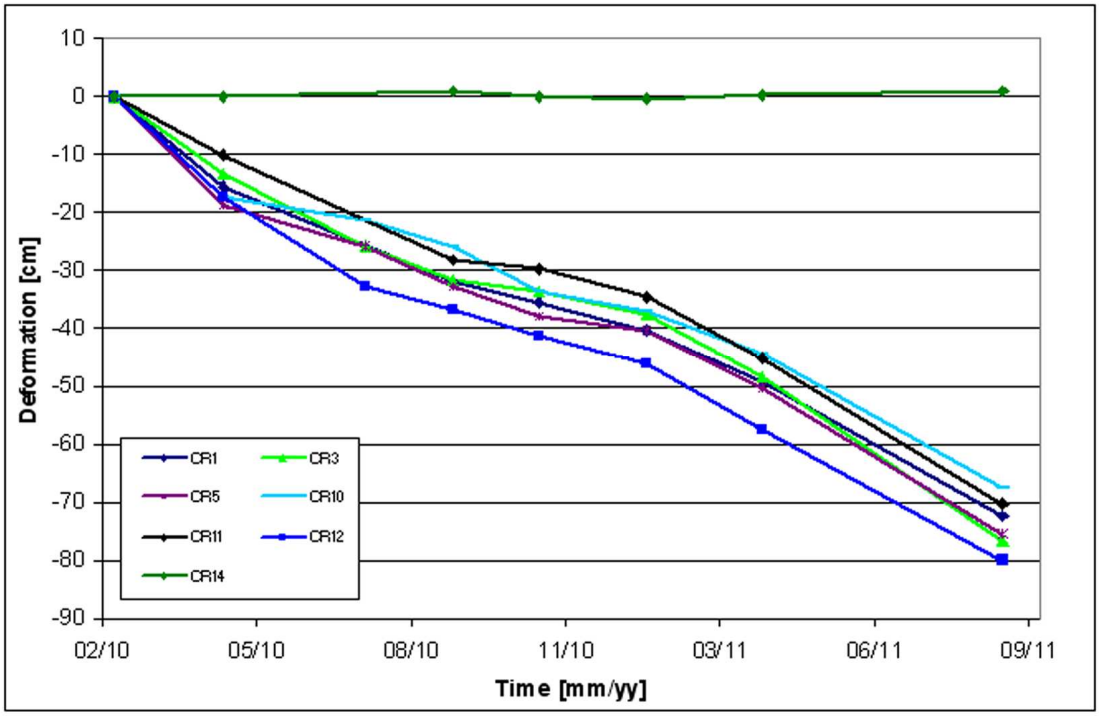

Figure 5.14: Time series of 7 CRs from Figure 5.13 for the whole measured period, from February 2010 to September 2011.

Chapter 6

Conclusions

This chapter summarizes the main conclusions of this thesis, which is devoted to the measurement and monitoring of deformations using the GB-SAR technique. In addition, it discusses the most important open technical issues that require further research.

The contribution of this dissertation is three-fold. Firstly, it offers a comprehensive description of a GB-SAR interferometric chain, which covers all aspects from data acquisition to the final deformation estimates. The description includes the main processing and analysis steps of the procedure and reflects the experience gained by the author in the last eight years working with both satellite and GB-SAR data. Secondly, it proposes an innovative algorithm, which addresses one of the most critical aspects of GB-SAR interferometry, i.e. the phase unwrapping, which is due to the ambiguous nature of the interferometric GB-SAR observations. This thesis proposes a new algorithm, which is named 2+1D phase unwrapping. Its main characteristics are discussed later in this chapter. Thirdly, the thesis proposes an innovative algorithm for GB-SAR long-term monitoring, which is based on the amplitude component of the SAR images. Using this algorithm a completely new GB-SAR approach can be implemented, which is named non-interferometric GB-SAR, and which offers interesting complementary advantages with respect to GB-SAR interferometry. This approach is undergoing the review process to get a European patent (Crosetto and Monserrat, 2011).

The conclusions of this thesis and the discussion of future research needs are organized in two main parts: the interferometric approach to deformation measurement and the non-interferometric one.

- ***Interferometric approach for deformation measurement.*** The core of this part consists in the description of a whole GB-SAR interferometric chain for deformation measurement. The Chapter 3 has been focused on the description of the standard GB-SAR processing chain implemented at IG. Each step of the procedure has been discussed and illustrated by using real data acquired at different sites. Out of the whole procedure, three steps deserve a specific discussion: pixel selection, phase unwrapping, and the atmospheric phase estimation.

  The pixel selection has been addressed by discussing two different criteria: the coherence, which is a spatial-based criterion, and the dispersion of the amplitude (DA), which is a point-based criterion. Although the two criteria have demonstrated to be useful in the processing of several GB-SAR datasets, they directly depend on the choice of a given threshold value. This involves finding a trade-off between point density and the quality of the selected phases. An empirical way to prove the goodness of the chosen threshold is by analysing the quality of the phase unwrapping results, which depends on both the phase quality and the pixel density. Further research is needed to define more robust and automatic pixel selection criteria. A further limitation is related to the fact

that the DA is a statistics that is usually computed on the whole set of images. On one hand, pixels that contain valuable interferometric phases, but not during the whole monitoring period, may be discarded: more advanced techniques need to be developed to take advantage of such pixels. On the other hand, pixels that are globally good can be contaminated by subsets of noisy phases: more elaborated techniques should be adopted to exploit them.

The second important topic is the phase unwrapping, which is one of the weakest points of SAR and GB-SAR interferometry. In the procedure described in Chapter 3 it is performed automatically on each interferogram. Usually, its quality control is performed visually, by inspecting the unwrapped phases. However, this involves a cumbersome operation, which hampers a complete quality check. In Chapter 4 a new phase unwrapping algorithm has been proposed, which is called 2+1D phase unwrapping. The algorithm has been fully described, discussing in particular the pixel wise unwrapping strategy. The main conclusions related to the 2+1D phase unwrapping are listed below.

- The importance of phase unwrapping errors has been illustrated considering different real case examples: if not properly corrected, these errors may drastically degrade the quality of the deformation time series. The performances of the new algorithm have been shown considering the same examples: clear improvements with respect to the standard approach have been achieved.
- The detection and correction of the phase unwrapping errors is performed in a fully automated fashion: this is particularly valuable to process very large sets of GB-SAR images, e.g. several hundreds or thousands of images, where the visual inspection of the unwrapping results is unfeasible.
- The proposed method works properly with redundant networks of interferograms and images, and with rather uniform distributions of unwrapping errors in these networks. A sufficient network redundancy can be usually guaranteed, while the concentration of unwrapping errors is usually not predictable: big error concentrations usually prevent a proper error detection and correction.
- A remarkable advantage of int2ima is the possibility to derive a kind of quality index, which describes, in an automatic way, the quality of the unwrapping estimates. This is based on the analysis of the residuals. This is a remarkable advantage of the algorithm because, for all cases where the error detection and correction does not work, e.g. where high concentrations of errors occur, we can get a warning through the quality index. This has a positive impact on the interpretation and exploitation of the results.

Considering the positive results achieved so far, it could be worth devoting further research efforts to the int2ima algorithm. Firstly, the algorithm should be improved to improve its computation performances. Secondly, efficient procedures need to be found to check and analyse the unwrapping data in the most critical configurations, i.e. weak network configurations and high concentrations of unwrapping errors. Finally, more work is needed to fully take advantage of the int2ima quality indices.

The last important step of the interferometric approach is the atmospheric phase estimation. In this dissertation the atmospheric phase component is estimated by using a 2D polynomial, whose degree can be selected as a function of the site characteristics. Although this approach generally provides good results, three limitations must be underlined. Firstly, it works under the assumption that the APS varies smoothly along the scene: in some scenarios this can be not the case, especially where abrupt topographic variations occur. Secondly, it is critically dependent on the quality of the unwrapped

phases; this quality cannot always be guaranteed, especially for all critical cases, e.g. low coherence, etc. Finally, it is strongly dependent on the distribution of the stable areas with respect to the displacement area at hand. Further research should be devoted to overcome these limitations.

- ***Non-interferometric approach for deformation measurement.*** A new procedure for measuring terrain deformation with GB-SAR data has been proposed. This procedure, which is amplitude-based, exploits the GB-SAR data without using the interferometric phase. The procedure overcomes three of the main limitations of the GB-SAR interferometry:

- The procedure is aliasing-free, i.e. it is not affected by the limitations related to phase unwrapping, especially those related to the deformation rates of the observed phenomena, which represent a severe drawback of GB-SAR interferometry. The price to be paid for this remarkable advantage is a reduction of the sensitivity and precision of the achievable deformation estimates
- The procedure is basically not affected by atmospheric effects, which mainly influence the GB-SAR phase.
- The method can in principle provide 2D displacement measurements, in range and in the cross-range directions. This represents an improvement with respect to the mono-dimensional LOS measurement capability of GB-SAR interferometry. However, the validation results have been shown weak performances of deformation estimates in the cross-range direction. A more in depth analysis is needed to understand if there is room for improving such performances. On the other hand, promising results have been obtained in the range direction.

Several experiments have been devoted to analyse the performances and validate the proposed approach. The main outcomes are:

- Achieving a precision of 1/50 pixels, which results in 1 cm in range using IBIS-L, requires scatterers with a peak to background ratio bigger than 30 db.
- The number of natural scatterers that provide the needed peak to background ration is usually very limited. Although this aspect is site-dependent, in the three studied sites the percentage of 30 db scatterers is less than the 1%.
- The use of CRs is usually needed to ensure a sufficient sampling of the deformation.
- The effectiveness of the procedure has been demonstrated on a real landslide case. Monitoring it during one year and half, displacements up to 75 cm were measured. Obtaining equivalent results using the non-continuous interferometric GB-SAR approach would have been unfeasible due to the aliasing effects.

To conclude, further investigation is needed to improve some aspects of the procedure. One of the weak aspects of the actual implementation is the need of deploying CRs to reach the required peak to background ratio. Further research will be focused on new image matching algorithms able to take full advantage of natural reflectors. A second aspect is related the usability of the CRs, especially at long distances that require CRs of considerable sizes. The development of active CRs would significantly reduce the CR size, contributing to improve the logistics of the measurement campaigns, especially at long distances, e.g. above 2 km. Finally, the methodology could be extended to real aperture radar systems: this would simplify considerably the logistics of the campaigns because the real aperture radar does not require the use of a rail.

Bibliography

Adam, N., Parizzi, A., Eineder, M., Crosetto, M., 2009. "*Practical Persistent Scatterer processing validation in the course of the Terrafirma project*". Journal of Applied Geophysics, Vol. 69, pp. 59-65.

Alba, M., Bernardini, G., Giussani, A., Ricci, P.P., Roncoronia, F., Scaioni, M., Valgoic, P., Zhangd, K., 2008. "*Measurement of dam deformations by terrestrial interferometric techniques*". International Archives of the Photogrammetry, Remote Sensing and Spatial Information Sciences, Vol. 37, Part B1, Beijing (China).

Antonello, G., Casagli, N., Farina, P., Leva, D., Nico, G., Sieber, A.J.,Tarchi, D., 2004. "*Ground-based SAR interferometry for monitoring mass movements*". Landslides, 1(1), pp. 21–28.

Antonello, G., Casagli, N., Farina, P., Fortuny, J., Leva, D., Nico, G., Sieber, A.J., Tarchi, D., 2003. "*A ground-based interferometer for the safety monitoring of landslides and structural deformations"*. Proc. of International Geoscience and Remote Sensing Symposium, (IGARSS), Vol. 1, pp. 218–220, Seoul (South Korea).

Bamler, R. and Just, D., 1993. "*Phase statistics and decorrelation in SAR interferograms*". Proc. of International Geoscience and Remote Sensing Symposium, (IGARSS), pp 980-984, Tokyo (Japan).

Bamler, R. and Hartl, P., 1998. "*Synthetic aperture radar interferometry"*. Inverse Problems, Vol. 14, pp. R1–54.

Bamler, R., and Eineder, M., 2004. "*Split Band Interferometry versus absolute ranging with wideband SAR systems*". Proc. of International Geoscience and Remote Sensing Symposium, (IGARSS), Vol. 2, pp. 980–984, Anchorage (USA).

Bernardini, G., Ricci, P., Coppi, F., 2007. "*A ground based microwave interferometer with imaging capabilities for remote measurements of displacements*". Proc. of 7th Geomatic Week, Barcelona.

Biescas, E., Crosetto, M., Agudo, M., Monserrat, O., Crippa, B., 2007. "*Two Radar Interferometric Approaches to Monitor Slow and Fast Land Deformation*". Journal of Surveying Engineering, Vol. 133, Issue 2, pp. 66-71.

Casagli, N., Tibaldi, A., Merri, A., Del Ventisette, C., Apuani, C., Guerri, L., Fortuny-Guasch, J., Tarchi, D., 2009. "*Deformation of Stromboli Volcano (Italy) during the 2007 eruption re-vealed by radar interferometry:Numerical modelling and structural geological field data*". Journal of Volcanology and Geothermal Research, 182 (2009), pp. 182–200.

Casagli, N, Catani, F, Del Ventisette, C, Luzi, G, 2010. "*Monitoring, prediction, and early warning using ground-based radar interferometry*". Landslides 7(3), pp. 291–301

Costantini, M., 1998. "*A novel phase unwrapping method based on network programming*". IEEE Trans. Geosci. Remote Sens., Vol. 36 (3), pp. 813– 821.

Costantini, M. and Rosen, P. A., 1999. "*A generalized phase unwrapping approach for sparse data*". Proc. of International Geoscience and Remote Sensing Symposium, (IGARSS), Vol. 1, pp. 267–269, Hamburg (Germany).

Crosetto, M., Monserrat, O., Bremmer, C., Hanssen, R., Capes, R., Marsh S., 2008. "*Ground motion monitoring using SAR interferometry: Quality assessment*". European Geologist, N. 26, pp. 12-15.

Crosetto, M, Monserrat, O., Iglesias, R. and Crippa, B., 2010. "*Persistent Scatterer Interferometry: potential, limits and initial C- and X-band comparison*". Photogrammetric Engineering and Remote Sensing, Vol. 76, nº 9, pp. 1061-1069.

Crosetto, M., Monserrat, O., Cuevas, M., Crippa, B., 2011. "*Spaceborne Differential SAR Interferometry: Data Analysis Tools for Deformation Measurement*". Remote Sens., 3, pp. 305-318.

Crosetto, M. and Monserrat, O., 2011. "*A method for monitoring terrain and man-made feature displacements using Ground-Based Synthetic Aperture Radar (GBSAR) data*". European patent, application nº 11382216.7 (patent pending).

Curlander, C. and McDonough, R. N. ,1991. "*Synthetic Aperture Radar Systems and Signal Processing*". New York: Wiley, sec. V.3.

Del Ventisette, C., Intrieri E., Luzi G., Casagli, N., Fanti R., and Leva, D., 2011."*Using ground based radar interferometry during emergency: the case of the A3 motorway (Calabria Region, Italy) threatened by a landslide*", Nat. Hazards Earth Syst. Sci., Vol. 11, pp. 2483–2495.

Ferretti, A., Prati, C., Rocca, F., 2001. "*Permanent scatterers in SAR interferometry*". IEEE Trans. Geosci. Remote Sens., Vol. 39(1), pp. 8-20.

Ferretti, A., Monti-Guarneri, A., Massonnet, D., Prati, C., Rocca, F., 2007. "*InSAR Principles: guidelines for SAR Interferometry Processing and Interpretation*". ESA Publications ESTEC Noordwijk NL; TM-19, ed. K. Flecther ISBN 92-9092-233-8.

Fornaro, G., Franceshetti, G. and Lanari, R., 1996. "*Interferometric SAR phase unwrapping using Green's formulation*". IEEE Trans. Geosci. Remote Sens., Vol. 34, pp. 720–727.

Förstner, W., 1984. "*A feature-based correspondence algorithm for image matching*". International Archives of the Photogrammetry, Remote Sensing and Spatial Information Sciences, Vol. 26 (3/3), pp. 150–166.

Fortuny-Guash, J. and Sieber, A. J., 1994. "*Fast algorithm for near-field synthetic aperture radar processor*". IEEE Trans. Antennas Propagat., Vol. 42, pp. 1458–1460.

Fortuny-Guasch, J., 2009. "*A Fast and Accurate Far-Field Pseudopolar Format Radar Imaging Algorithm*". IEEE Trans. Geosci. Remote Sens., Vol. 47(4), pp. 1187–1196.

Gabriel, A.K., Goldstein, R.M. and Zebker, H.A., 1989. "*Mapping small elevation changes over large areas: differential radar interferometry".* Journal of Geophys. Res., Vol. 94, nº B7, pp. 9183–9191.

Galahad D2.2. "*Results of the evaluation of the expected accuracy and precision of GB-SAR*". Deliverable D2.2 of the project Galahad, 2008. http://www.galahad.eu/.

Ghiglia, D. C. and Romero, L. A., 1989. "*Direct phase estimation from phase differences using fast elliptic partial differential equation solvers*". Opt. Lett., Vol. 15, pp. 1107–1109.

Ghiglia, D. C. and Romero, L. A., 1994. "*Robust two-dimensional weighted and unweighted phase unwrapping that uses fast transforms and iterative methods*". J. Opt. Soc. Amer. A, Vol. 11, nº 1, pp. 107–117.

Ghighlia, D. C. and Pritt, M. D., 1998. "*Two-Dimensional Phase Unwrapping: Theory, Algorithms, and Software*". New York: Wiley-Interscience.

Goldstein, R. M., Zebker, H. A. and Werner, C. L., 1988. "*Satellite radar interferometry: Two-dimensional phase unwrapping*". Radio Sci., vol. 23, nº 4, pp. 713–720.

Golub, G.H., and Van Loan, C.F., 1989. "*Matrix Computations*"*., 2nd ed.*, Baltimore: Johns Hopkins University Press.

Gruen, A., 1985. "*Adaptive Least Squares Correlation: A Powerful Image Matching Technique*". South African J. Photogrammetry, Remote Sensing and Cartography, vol. 3, nº 14, pp. 175-187.

Hanssen, R. and Bamler, R., 1999. "*Evaluation of interpolation kernels for SAR interferometry*". IEEE Trans. Geosci. Remote Sens., Vol. 37(1), pp. 318-321.

Hanssen, R., 2001. "*Radar interferometry*". Kluwer Academic Publishers, Dordrecht (The Netherlands).

Heiskanen, W. and Moritz, H., 1967. "*Physical Geodesy"*, H.W. Freeman, San Francisco.

Herrera, G., Fernandez-Merodo, JA., Mulas, J., Pastor, M., Luzi G., Monserrat, O., 2009. "*A landslide forecasting model using ground based SAR data: the Portalet case study*". Engineering Geology, Vol. 105, Issue: 3-4, pp. 220-230.

Iannini, L., Monti Guarnieri, A., Giudici, D., 2009. "*Atmospheric phase screen in ground based radar: statistics and compensation*". Proc. of Fringe 2009 workshop: advances in the science and application of SAR interferometry, Frascati (Italy).

Laakso, T.I., Valimaki, V., Karjalainen, M. and Laine, U.K, 1996. "*Splitting the unit delay [FIR/all pass filters design]*", IEEE Signal Processing Magazine, Vol. 13, Issue 1, pp. 30-60.

Leva, D., Nico, G., Tarchi, D., Fortuny, J., Sieber, A.J., 2003. "*Temporal analysis of a landslide by means of a ground-based SAR interferometer*". IEEE Trans. Geosci. Remote Sens., Vol. 41, pp. 745–752.

Lin, Q., Vesecky, J. F. and Zebker, H. A. 1992. "*New approaches in interferometric SAR data processing*". IEEE Trans. Geosci. Remote Sens., Vol. 30, pp. 560-567.

Lingua A., Piatti D., Rinaudo F., 2008. "*Remote monitoring of a landslide using an integration of GB-InSAR and lidar techniques*". International Archives of the Photogrammetry, Remote Sensing and Spatial Information Sciences. Vol. 37. Part B1. Beijing 2008.

Luzi, G., Pieraccini, M., Mecatti, D., Noferini, L., Guidi, G., Moia, F. and C. Atzeni, 2004. "*Ground-based radar interferometry for landslides monitoring: Atmospheric and instrumental decorrelation sources on experimental data*". IEEE Trans. Geosci. Remote Sens., Vol. 42, nº 11, pp. 2454–2466.

Luzi, G., Pieraccini, M., Mecatti, D., Noferini, L., Macaluso, G., Tamburini, A., Atzeni, C., 2007. "*Monitoring of an Alpine Glacier by Means of Ground-Based SAR Interferometry*". IEEE. Geosci. Remote Sens. Letters, Vol. 4, nº 3, pp. 495-499.

Luzi, G., Noferini, L., Mecatti, D., Macaluso, G., Pieraccini, M., Atzeni, C., Schaffhauser, A., Fromm, R., and Nagler, T., 2009. "*Using a groundbased SAR interferometer and a terrestrial laser scanner to monitor a snow-covered slope: Results from an experimental data collection in Tyrol (Austria)*". IEEE Trans. Geosci. Remote Sens., Vol. 47, pp. 382–394.

Luzi, G., 2010. "*Ground-based SAR Interferometry: a novel tool for Geoscience*". Geoscience and Remote Sensing, New Achievements, pp. 01-026, P. Imperatore & D. Riccio editors, Vukopvar (Croatia).

Luzi, G., Monserrat, O., Crosetto, M., Copons, R., Altimir, J., 2010a.. "*Ground-Based SAR interferometry applied to landslide monitoring in mountainous areas*". Proc. of Mountain Risks conference: Bringing science to society, Florence (Italy).

Luzi, G., Crosetto, M., Monserrat, O., 2010b. "*Advanced Techniques for Dam Monitoring*". Proc. of II International Congress on Dam Maintenance and Rehabilitation, pp. 23-25, Zaragoza (Spain).

Luzi, G., Monserrat, O., Crosetto, M., 2011. "*Potential of coherent radar to support the monitoring of building health state*". Submitted to Research in Non-Destructive Evaluation Journal.

Martinez-Vazquez, A., Fortuny-Guasch, J. and Gruber, U., 2005. "*Monitoring of the snow cover with a ground-based synthetic aperture radar*". Proc. of EARSeL symposium, Vol. 4, nº 2, pp.171-178, Porto (Portugal).

Martinez-Vazquez, A., and Fortuny-Guasch, J., 2007. "*Snow Avalanche Detection and Classification Algorithm for GB-SAR Imagery*". Proc. of International Geoscience and Remote Sensing Symposium, (IGARSS), pp. 3740 – 3743, Barcelona (Spain).

Martinez-Vazquez, A., 2008. "*Snow cover monitoring techniques with GB-SAR*". PhD thesis, Universitat Politècnica de Catalunya. http://hdl.handle.net/10803/6922.

Mecatti, D., Noferini, L., Macaluso, G., Pieraccini, M., Luzi,, G., Atzeni, C. and Tamburini, A., 2007. "*Remote sensing of glacier by ground-based radar interferometry*", Proc. of International Geoscience and Remote Sensing Symposium, (IGARSS), pp. 4501–4504, Barcelona (Spain).

Mecatti, D., Macaluso, G., Barucci, A., Noferini, L., Pieraccini, M. and Atzeni, C., 2010. "*Monitoring open-pit quarries by interferometric rada for safety purposes*", Proc. of European Radar Conference (EuRAD), Paris (France).

Monserrat, O., Crosetto, M., 2008. "*Deformation measurement using terrestrial laser scanning data and least squares 3D surface matching*". ISPRS Journal, Vol. 63, Issue 1, pp. 142-154.

Monserrat, O., Crosetto, M. Cuevas, M. and Crippa, B., 2011. "*The thermal expansion component of Persistent Scatterer Interferometry observations*". IEEE. Geosci. Remote Sens. Letters, Vol. 8, pp. 864-868.

Nico, G., Leva, D., Antonello, G., Tarchi, D., 2004. "*Ground-based SAR interferometry for terrain mapping: theory and sensitivity analysis*". IEEE Trans. Geosci. Remote Sens., Vol.42, nº 6, pp. 1344- 1350.

Noferini, L., Pieraccini, M., Mecatti, D., Macaluso, G., Atzeni, C., 2005a. "*Long terml and slide monitoring by Ground Based SAR Interferometer*". International Journal of Remote Sensing, Vol. 27, pp. 1893–1905.

Noferini, L., Pieraccini, M., Mecatti, D., Luzi, G., Tamburini, A., Broccolato, M. and Atzeni, C., 2005b. "*Permanent scatterers analysis for atmospheric correction in ground-based SAR interferometry*". IEEE Trans. Geosci. Remote Sens., Vol. 43, nº 7, pp. 1459–1471.

Noferini, L., Pieraccini, M., Mecatti, D., Macaluso, G., Luzi, G., Atzeni, C.,2007. "*DEM by ground-based SAR interferometry*". IEEE. Geosci. Remote Sens. Letters, Vol. 4(4), pp. 659–663.

Perna, S., Wimmer, C., Moreira, J. and Fornaro, G., 2008. "*X-band airborne differential interferometry: Results of the OrbiSAR campaign over the Perugia area*". IEEE Trans. Geosci. Remote Sens., Vol. 46, nº 2, pp. 489– 503.

Pieraccini, M., Casagli, N., Luzi, G., Tarchi, D., Mecatti, D., Noferini, L., Atzeni, C., 2002. "*Landslide Monitoring by Ground-Based Radar Interferometry: a field test inValdarno (Italy)*". International Journal of Remote Sensing, Vol. 24, pp. 1385–1391.

Pipia, L. , Fabregas, X., Aguasca, A., Mallorqui, J. J. A., 2006. "*Comparison of different techniques for atmospheric artifact compensation in GB-SAR differential acquisitions*". Proc. of International Geoscience and Remote Sensing Symposium, (IGARSS), pp. 3739–3742, Denver, Colorado (USA).

Pipia L., Fabregas X., Aguasca A., Lopez-Martinez C., Mallorqui J., Mora O., 2007. "*A Subsidence Monitoring Project using a Polarimetric GB-SAR Sensor*". Proc. of the 3rd Int. Workshop POLinSAR, Frascati (Italy).

Pipia, L., Fabregas, X., Aguasca, A., Duque, S., Mallorqui, J.J., Lopez-Martinez, C., 2008. "*Polarimetric Deformation Maps Retrieval of Urban Areas using Ground-Based SAR Acquisitions*". Proc. of International Geoscience and Remote Sensing Symposium, (IGARSS), Vol.4, nº 4, pp. 327-330, Boston (USA).

Rödelsperger, S., Becker, M., Gerstenecker, C., La¨ufer, G., Schilling, K. and Steineck, D., 2010a. "*Digital elevation model with the ground-Monitoring of displacements with ground-based microwave interferometry: IBIS-S and IBIS-L*". Journal of Geodynamics Vol. 49, pp. 241–246.

Rödelsperger S., Läufer G., Gerstenecker C. and Matthias B., 2010b. "*Monitoring of displacements with ground-based microwave interferometry,: IBIS-S and IBIS-L*". Journal of Applied Geodesy, Vol. 4, pp. 41-54

Rosen, P. A., Hensley, S., Joughin, I. R., Li, F. K., Madsen, S. N., Rodríguez, E., and Goldstein, R. M., 2000. "*Synthetic aperture radar interferometry*". Proc. of IEEE, Vol. 88, Issue 3, pp. 333–382.

Rudolf, H., Leva, D. Tarchi, D. Sieber, A.J., 1999. "*A mobile and versatile SAR system*". Proc. of International Geoscience and Remote Sensing Symposium, (IGARSS), pp. 592–594, Hamburg (Germany).

Schaffhauser, A., Adams, M., Fromm, R., Jörg, P., Luzi, G., Noferini, L., and Sailer, R., 2008. "*Remote sensing based retrieval of snow cover properties*". Cold Regions Science and Technology, Vol. 54(3), pp. 164-175.

Skolnik, M. I., 1991, "*Radar Handbook*", 2nd ed. New York: McGraw-Hill.

Strang, G., 1998. "*Introduction to linear algebra*". Wellesley: Wellesley-Cambridge Press.

Tarchi, D., Rudolf, H., Luzi, G., Chiarantini, L., Coppo, P. and Sieber, A. J., 1999. "*SAR interferometry for structural changes detection: A demonstration test on a dam*". Proc. of International Geoscience and Remote Sensing Symposium, (IGARSS), pp. 1522–1524, Hamburg (Germany).

Tarchi, D., Rudolf, H., Pieraccini, M. and Atzeni, C., 2000. "*Remote monitoring of buildings using a ground-based SAR: Application to cultural heritage survey*". International Journal of Remote Sensing, Vol. 21, nº 18, pp. 3545–3551.

Tarchi, D., Casagli, N., Fanti, R., Leva, D., Luzi, G., Pasuto, A., Pieraccini, M., Silvano, S., 2003. "*Landslide monitoring by using ground-based SAR interferometry: an example of application*". Engineering Geology, Vol. 68, Issues 1–2, pp. 15–30

Werner, C., Strozzi, T., Wiesmann, A., Wegmuller, U., 2008. "*A Real-Aperture Radar for Ground-Based Differential Interferometry*". Proc. of International Geoscience and Remote Sensing Symposium, (IGARSS), Vol. 3, nº 3, pp. 210-213, Boston (USA).

Wimmer, C, Siegmund, R, Schwabisch, M. and Moreira, J., 2000. "*Generation of high precision DEMs of the Wadden Sea with airborne interferometric SAR*". IEEE Trans. Geosci. Remote Sens., Vol. 38, nº 5, pp. 2234–2245.

Zhou, Z., Motoyuki S., 2003. "*Ground-based polarimetric SAR systems for environment studies*". Proc. of Antennas and Propagation Society International Symposium, Vol.1, pp. 202- 205.

Zhou, Z., Hamasaki, T., Sato, M., Boerner, W., 2004. "*3-D broadband ground-based polarimetric SAR data processing for the monitoring of vegetation growth variations*", Proc. of International Geoscience and Remote Sensing Symposium, (IGARSS), pp. 1248 -1251, Anchorage (USA).